Wang, P., Prell, W.L., Blum, P., et al., 2000
Proceedings of the Ocean Drilling Program, Initial Reports Volume 184

4. SITE 1143[1]

Shipboard Scientific Party[2]

BACKGROUND AND OBJECTIVES

The primary objectives of Site 1143 (proposed site SCS-9) in the southern South China Sea (SCS) were to (1) reconstruct the development of sea-surface temperature (SST) seasonality and its relation to the stability of the Western Pacific Warm Pool; (2) compare long-term records of accumulation rates and sediment variability in the southern SCS to records of uplift, denudation, and climate change; and (3) identify and interpret climate change in the southern SCS in the context of summer and winter monsoon evolution.

Site 1143 is located at 9°21.72′N, 113°17.11′E, at a water depth of 2772 m (Fig. **F8,** p. 52, in the "Leg 184 Summary" chapter). The site lies within the northwestern part of the Dangerous Grounds or Nansha Islands area, a region of poorly charted islands and reefs on the southern continental slope of the SCS. Because the initial sites proposed in this area were close to a hydrocarbon province, discussions with the Pollution Prevention and Safety Panel (PPSP) resulted in locating SCS-9 farther downslope (to the north) and limiting penetration to 400 m (note that Hole 1143C was deepened to 500 meters below seafloor (mbsf); see **"Operations,"** p. 3). The final location of Site 1143 lies between the high accumulation rate (100–300 m/m.y.) terrigenous deposits of the paleo-Sunda and Mekong Rivers to the south and the carbonate-rich but low sedimentation rate (10–20 m/m.y.) region of the northernmost southern margin (Sarnthein et al., 1994; Huang and Wang, 1998). We expected that the location of Site 1143 would have an accumulation rate of ~50 m/m.y. and would be a sensitive indicator of both the pelagic and terrigenous sources in the southern SCS. Given these accumulation rates, we expected to reach the upper Miocene (~8 Ma) with 400 m penetration.

The basement structure and sediment cover near Site 1143 are complex, as indicated by the seismic lines (NS95-240 and NSL95-160) pro-

---

[1] Examples of how to reference the whole or part of this volume.
[2] Shipboard Scientific Party addresses.

vided by Guangzhou Marine Geological Survey, Ministry of Land and Resources of China (Figs. **F1,** p. 11, and **F4,** p. 16, in the "Seismic Stratigraphy" chapter). The site lies near the cross point of Lines NSL160 at common depth point (CDP) 1812 and NS240 at CDP 3617. This area is characterized by basement faulting on a scale of a few kilometers, overlain by sediments ranging from 700 to 1400 m in thickness. A series of seismic reflectors in this area, mapped by the Guangzhou Marine Geological Survey, indicated that the 400-m penetration should reach midway between Reflectors T_1 (Miocene/Pliocene boundary; 5.2 Ma) and T_2 (top of the middle Miocene; 10.2 Ma). Note that the latter reflector designation was uncertain. Site 1143 was approached along seismic Line NSL160 (from southwest to northeast) using the 3.5-kHz recorder to verify the bathymetry. The 3.5-kHz surface reflections and near-surface reflectors were parabolic, suggesting an irregular surface on a scale of meters. Site 1143 is located in a slight depression within a fault basin that contains ~1.25 s (~1250 m) of sediment. Because of interference by observing vessels, a more complete survey could not be conducted; the prospectus site location was confirmed by identification of the depth gradient leading to the site and the water depth.

Site 1143 provides a record of low-latitude climate that contrasts with the northern SCS sites and will enable us to construct a history of the thermal gradient within the SCS. The site lies within the Western Pacific Warm Pool, which has average annual temperatures >28°C and occupies much of the near-equatorial region of the western Pacific and eastern Indian Ocean. These warm waters provide latent heat to the summer monsoon circulation and are the source of convection that drives the Walker Circulation. The SST estimates from faunal, isotopic, and biomarker data at Site 1143 will provide information on both the long- and short-term variability of temperatures in the southern SCS and thus on the stability of the Warm Pool. The SST contrast with the northern sites will identify when the SCS began to develop large thermal gradients, primarily caused by lower winter SSTs associated with the development of the winter monsoon. Although seasonality is not uniquely related to monsoon circulation, an increase in seasonality during the past glacial interval is attributed, at least in part, to the strengthening of the East Asian winter monsoon.

Site 1143 is also thought to record terrigenous flux from the Mekong River system, which drains a large area of southeastern Asia and portions of the Tibetan Plateau. Therefore, the pattern of Neogene terrigenous accumulation rates at this site should provide a new record of sediment erosion, weathering, and transport related to Himalayan-Tibetan uplift; this record may then be compared with relevant records from the Bengal Fan (Leg 116) and Arabian Sea (Leg 117).

In addition to its geological complexity, Site 1143 had its share of logistical and political complexity (see **"Operations,"** p. 3). As noted earlier, Site 1143 lies within the Dangerous Grounds area in the southern part of the South China Sea. Before navigation in this area, a port call was required to repair the shipboard 10-cm radar. In addition, transit to and from the site was made only during daylight and at reduced speeds. Finally, this region of the South China Sea is claimed by multiple jurisdictions, and diplomatic clearances were required from all parties. Besides waiting on final clearances, incidents of piracy near the Spratly Islands raised safety concerns that were addressed by contacting all jurisdictional parties to confirm the ship's location and its times of operation. Despite multiple obstacles, the Leg 184 shipboard party recovered an excellent sediment record from Site 1143.

OPERATIONS

Port Call

Leg 184 began at 0730 hr on 11 February 1999 when the first line was passed ashore at the Victoria Quay in Fremantle, Australia. A number of engineering tasks were accomplished during the port call, including the installation of a new housing unit (penthouse), a container to house the microbiology laboratory on top of the lab stack, a vegetable chiller on the sun deck, and the replacement of the boom on Crane 2. The arrival of several freight containers that contained critical engine parts was delayed, and the vessel had to remain in port 2.5 days beyond the planned departure at 0600 hr on 16 February. At 1730 hr on 18 February, the last line was released from Victoria Quay, and the vessel cleared the harbor.

Transit to Site 1143 (Proposed Site SCS-9)

Site 1143 in the Nansha or Spratly Island area is located in an area that required special diplomatic efforts and safety protocols, which were finalized during the eventful 2800-nmi transit. Before the *JOIDES Resolution* could proceed to the prospective site, it required approval of the four political entities that lay claim to the region. Three countries (People's Republic of China [PRC], Vietnam, and the Philippines) had given formal consent before the drillship left Australia. The approval from Chinese Taipei was received on 26 February, a few days before drilling operations began.

Site 1143 is situated in poorly charted waters labeled Dangerous Grounds on the Admiralty charts. Although the site had been surveyed, extra precautions were necessary to ensure that the passage to the site was done in the safest possible manner. The 60-nmi transit across Dangerous Grounds was to be made at reduced speed, only during daylight, and only with calm seas and clear visibility.

Another issue was the piracy threat in the region. The vessel received a warning on 20 February from the Regional Piracy Center (RPC) in Kuala Lumpur via the Singapore Inmarsat C station (Sentosa Island) that the area around Sunda Strait and Karimata Island is the most prone to pirate raids. In response to this alert, the captain decided to adjust the speed of the ship to ensure a daylight transit across the Sunda Strait. The RPC alerted the vessel that persons in military uniforms and using military vessels had recently attacked ships passing close to the location of Site 1143. This information plus data from other sources raised serious questions regarding the security of the vessel during operations at Site 1143. The matter was referred to Ocean Drilling Program (ODP) management, who in turn consulted with senior program officials in Washington, D.C. On 22 February, a request was issued to the director of the Office of Ocean Affairs of the U.S. Department of State to review this matter and to provide advice, procedures, and assurances for the vessel's safety at Site 1143. On 23 February, the captain met briefly with the scientists and technicians and discussed ship security issues, including precautions that would be followed during the transit through the Sunda Strait. Also discussed were procedures to be followed should persons unknown attempt to board the vessel. Although an attack on the vessel was deemed highly unlikely, prudence and diligence required that this issue be addressed before crossing the strait.

At 0600 hr on 25 February, the vessel left the Indian Ocean and entered the Sunda Strait between Java and Sumatra. The ship entered the strait while it was still dark and with heavy rain punctuated by an occasional lightning flash. The eruption of Anak Krakatoa ("son of Krakatoa") was visible through the gloom from a distance of 20 nmi. The vessel passed within 6 nmi of the cone that is now growing in the caldera left by the 1883 eruption.

On the morning of 23 February, the S-band (10 cm) radar failed. During the subsequent trouble shooting by the Overseas Drilling Limited electronic technicians, the problem was ascertained to be in the rotary joint and/or associated cabling located in the antenna assembly. No spares for these items were on the vessel. The approach to Site 1143 required that both X-band and S-band radar units be operational. The vessel was therefore diverted to Singapore at 0830 hr on 26 February to allow factory representatives with the proper parts to work on the defunct unit. The ship arrived at the Changi holding anchorage in Singapore at 1500 hr on 27 February. At 1030 hr on 28 February, two technicians from Aeradion Technology Pte Ltd. and the vessel agent, Victor Chan, boarded the *JOIDES Resolution,* and the repairs were concluded in less than 2 hr. The vessel was under way to Site 1143 at 1215 hr on 28 February.

As the ship neared Dangerous Grounds, a fax was received on 3 March from the deputy director-general of the State Oceanic Administration of the Peoples' Republic of China in Beijing. This fax provided additional emergency contact phone and fax numbers in Beijing as well as reassurances that the Chinese navy had been instructed "to keep a close eye on the cruise." Because the PRC naval base at Yong-Shu-Jiao ("always summer reef") is located ~20 nmi northwest of Site 1143, this fax furnished the necessary assurances for vessel security that were required before establishing station keeping at Site 1143.

At 0445 hr on 3 March, ~5 nmi from the entry position to Dangerous Grounds, the forepeak tank was filled to adjust vessel trim bow down. This was done so that if the vessel were to ground on a reef, the bow would be the first point of contact. If the bow were to strike a shoal, the forepeak tank would be drained and the vessel backed off and diverted to a safe port for a hull inspection. At 0500 hr the speed was reduced to 6 kt; at 0600 hr, the *JOIDES Resolution* altered course from 49° to 90° at position 09°20.0′N, 112°5.5′E, and entered poorly charted waters. Lookouts were posted as the vessel made its way to the location that marked the beginning of the 3.5-kHz survey point.

At 1215 hr, a PRC navy patrol vessel, *South Tug 156,* was sighted. After an initial attempt by our Chinese co-chief to inform the PRC vessel of our identity, no radio communication was established. The patrol craft followed us to the site location. At 1530 hr another vessel, named *Truong SA-12*, approached the *JOIDES Resolution*, and the crew attempted to hail us. This ship identified itself as Vietnamese. Our captain was unable to communicate with the *Truong SA-12* because of the language barrier.

From 1500 to 1530 hr, a 3.5-kHz survey was conducted over an existing seismic line as the vessel approached the site from the southwest. The survey was aborted earlier than planned as a result of the proximity of the Chinese and Vietnamese vessels and accompanying communication problems. At 1605 hr, after verifying site location with bathymetry, the positioning beacon was dropped on precise Global Positioning System coordinates.

Site 1143 (Proposed Site SCS-9)

After the hydrophones and thrusters were extended and the vessel located on position, the corrected precision depth recorder depth referenced to the dual elevator stool was obtained and indicated 2782.4 m. The advanced hydraulic piston corer (APC) and extended core barrel (XCB) bottom-hole assembly was made up and deployed. During the tripping of the drill string, the vessels *Truong SA-12* and *South Tug 156* remained visible until nightfall. At 2200 hr, the *South Tug 156* moved away from the site and was lost to radar. The *Truong SA-12* lingered in the area and kept us company until the site was abandoned.

Hole 1143A

Hole 1143A was spudded with the APC at 0330 hr on 4 March. Piston coring advanced to 190.4 mbsf with excellent recovery (102%). The cores were oriented starting with Core 3H. APC refusal resulted when Core 21H did not achieve a full stroke into the indurated sediment. The hole was deepened with the XCB to the depth approved by the PPSP, 400 mbsf. The average recovery for the entire hole was 95% (Tables **T1**, **T2** [both also in **ASCII format**). Only a trace amount of methane was measured at concentrations <10 ppmv (see **"Organic Geochemistry,"** p. 18). No higher hydrocarbons were detected. Downhole temperature measurements were obtained using the APC temperature tool (APCT) before the retrieval of Cores 4H, 7H, 11H, and 16H, at 31, 60, 98, and 145 mbsf, respectively. A temperature gradient of 84°C/km was calculated from these data (see **"Physical Properties,"** p. 23).

T1. Site 1143 coring summary, **p. 81.**

T2. Site 1143 coring summary by section, **p. 83.**

Three wireline logging runs were planned. After the hole was flushed with a 30-bbl mud treatment, it was displaced with an additional 100 bbl of sepiolite. During the pipe trip to the logging depth of 86 mbsf, the driller did not observe any increased weight caused by a restriction in the size of the hole. The first log was conducted with the triple combination tool suite. Results of the first run determined that the hole was in generally good condition below 210 mbsf and provided satisfactory results below this depth. Above 210 mbsf, there were alternating swelling clays and washouts as large as 45 cm. Several tight spots were measured, and a 3-hr wiper trip was performed before the next tool string could be deployed. Later deployment of the Formation MicroScanner (FMS) and sonic tool combination encountered an obstruction in the hole at <20 m below the bit. Several attempts to pass this obstruction proved fruitless. The mud pumps were used in an attempt to hydraulically push the tool suite past the hole constriction, but this maneuver gained only ~3 m. A moderate overpull was required to free the tool from the mud. After recovering the logging tool, the drill pipe was lowered past the obstruction to a depth of 163 mbsf and then pulled back with the bit positioned at 134 mbsf. The second deployment of the FMS required well over an hour for the logging tool to be worked through the clays. The hole was logged in one pass from 378 to ~158 mbsf. The planned deployment of the geological high-resolution magnetic tool (GHMT) was canceled. The logging equipment was disassembled, and the drill string was pulled clear of the seafloor.

Hole 1143B

The vessel was offset 20 m east for Hole 1143B. Before coring was begun in this hole, a bottom-water temperature measurement was obtained with the APCT. At 0130 hr on 7 March, Hole 1143B was spudded with the APC. The inferred seafloor depth from the mudline recovery was 2783.5 m. After advancing to 175.4 mbsf, APC refusal resulted when Core 19H did not achieve a full stroke. The hole was deepened with nine XCB cores to 258.2 mbsf, which was considered the target depth for this hole. All piston cores were oriented starting with Core 3H. The bit cleared the seafloor at 0010 hr on 8 March. The average recovery for the hole was 95% (Tables T1, T2).

Hole 1143C

The vessel was offset 10 m east, and the last hole of the site was spudded with the APC at 0100 hr on 8 March. The seafloor depth calculated from a presumed mudline recovery of 9.4 m was 2784.5 m, but hole-to-hole correlation showed that the top of the core was actually 4 m below the mudline. The hole was APC cored to 177.4 mbsf. The piston cores were oriented starting with Core 3H. The hole was deepened with the XCB to 286 mbsf when approval was received to extend the depth of the hole to 500 mbsf. The XCB coring continued until 2315 hr on 9 March when the last core (54X) was recovered from 500 mbsf. The average recovery for the hole was 96%. The average recovery for the site was 95% (Tables T1, T2).

The drill pipe was pulled out of the hole and cleared the seafloor at 0045 hr on 10 March. As the drill string was being recovered, both primary and backup beacons were retrieved, and the hydrophones and thrusters were retracted. The bit was at the rotary table at 0530 hr, and by 0545 hr the drilling equipment was secured for the voyage to the next site. At 0655 hr, a submarine periscope was clearly visible as it crossed our bow and pursued a reciprocal course that brought it within one-quarter mile of the starboard side of our vessel. The *JOIDES Resolution* cleared Dangerous Grounds at 1300 hr at 10°0′N, 113°17.1′E.

COMPOSITE SECTION

We built a continuous meters composite depth (mcd) scale and a splice (as defined in "Composite Section," p. 3, in the "Explanatory Notes" chapter) that range from the top of Core 184-1143B-1H to the bottom of Section 184-1143B-20X-5. The splice and the continuous portion of the mcd scale extend from 0 to 190.85 mcd. Splice construction below this interval was precluded by incomplete core recovery, decreased core quality (e.g., biscuiting), and alignment of core gaps. As described below, however, we were able to construct a discontinuous, or "floating," mcd scale for the cores below 191 mcd (see "Composite Section," p. 3, in the "Explanatory Notes" chapter).

The mcd scale and the splice are based on the stratigraphic correlation of whole-core multisensor track (MST) and split-core color spectral reflectance (CSR) data (lightness, L*) collected at 2- to 4-cm intervals (see "Physical Properties," p. 23, for details). From the MST, we used magnetic susceptibility (MS), gamma-ray attenuation (GRA) bulk density, and natural gamma radiation (NGR) data; the *P*-wave data were of no stratigraphic use. These data, and the splice constructed from them, are presented on the mcd scale in Figures F1, F2, F3, and F4 (also as Synergy Software KaleidaGraph plots and Microsoft Excel data files [see the "Supplementary Materials" contents list]; the spliced records are also available in ASCII format). The depth offsets that comprise the

F1. Smoothed/correlated MS data and splice, p. 32.

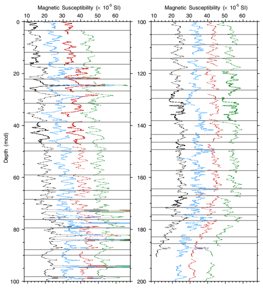

F2. Smoothed/correlated NGR data and splice, p. 35.

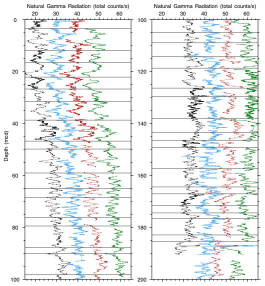

F3. Smoothed/correlated GRA data and splice, p. 38.

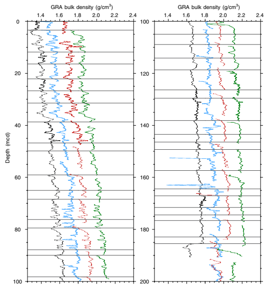

F4. Smoothed/correlated L* values from the CSR data and splice, p. 41.

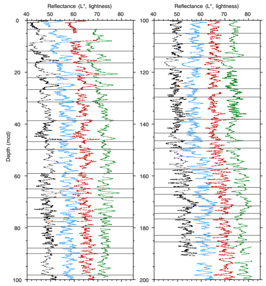

mcd scale are given in Table **T3** (also in **ASCII format**). The splice tie points (Table **T4,** also in **ASCII format**) should be used as a guide for detailed postcruise sampling.

T3. Site 1143 composite depths, **p. 84.**

T4. Site 1143 splice tie points, **p. 85.**

Magnetic susceptibility was the most useful stratigraphic tool for correlation. CSR and NGR were helpful in intervals where the MS structure was ambiguous. Gamma-ray attenuation was the least useful because intracore squeezing and stretching produced a signal that was often larger than the natural variability. We constructed the mcd scale by assuming that the uppermost sediment (the "mudline") in Core 184-1143B-1H was the sediment/water interface. This core, the "anchor" in the composite depth scale, is the only one with depths that are the same on the mbsf and mcd scales. From this anchor we worked downhole, correlating the stratigraphy core by core. Based on the correlations, we added a constant to the mbsf depth for each core in each hole in order to align the stratigraphic structure of each core log. We did not squeeze or stretch data within the depth domain. Because we did not make intracore adjustments to depth, we were not able to align every feature in the stratigraphic records. A good example of this occurs between 80 and 90 mcd: MS spikes representing ash layers are perfectly aligned, yet other correlative features may be misaligned (by as much as 50 cm).

Correlation of Cores 184-1143A-13H, 184-1143B-13H, and 184-1143C-13H (~115–130 mcd) was particularly challenging. We chose to match structure within the MS and CSR data. Alternative correlations are possible. In the splice, we chose to append successive cores from Hole 1143C at two locations (49.84 and 89.94 mcd) instead of incorporating short intervals from Hole 1143B (Table **T4**). Correlative structure in Holes 1143A and 1143B demonstrates that no significant amount of sedimentary section is missing between the appended cores from Hole 1143C.

Below 191 mcd, core quality and recovery decrease and turbidite frequency increases (see **"Lithostratigraphy,"** p. 8). Although the cores in this interval could not be tied directly to the composite depth scale (and thus the splice), they could be correlated with each other. Here we placed the cores in a relative, or discontinuous, composite depth scale, which we refer to as the "floating" mcd (as defined in **"Composite Section,"** p. 3, in the "Explanatory Notes" chapter). This scale is not tied to the overlying mcd scale (and thus back to the mudline). Instead, the positions of the cores in Holes 1143A and 1143B below 191 mcd are adjusted such that correlative features match those in Hole 1143C, whose depths retain the offset accumulated at the bottom of the splice. Correlation below 191 mcd is less certain than in the overlying interval, except for the ties made between MS events associated with turbidite layers (Fig. **F1**).

In several cases, we noted stratigraphic distortion among correlative cores from adjacent holes. We attribute much of this to the normal coring process, although we cannot discount the possibility that some may reflect true differences among the stratigraphic sections. An example of the stratigraphic distortion is the low GRA values at the tops of cores, indicating stretching relative to the bottoms (Fig. **F3**).

LITHOSTRATIGRAPHY

Lithologic Units

Unit I (0–512.4 mcd)

Interval: Cores 184-1143A-1H through 44X; Cores 184-1143B-1H through 28X; Cores 184-1143C-1H through 54X
Depth: 0–400.0 (Hole 1143A); 0–258.2 (Hole 1143B); 0–500.0 (Hole 1143C)
Age: late Miocene to Pleistocene

Lithologic description of Site 1143 was made by visual inspection of the cores, smear-slide analysis, and carbonate content determined by coulometer analysis (for methods, see **"Organic Geochemistry,"** p. 14, in the "Explanatory Notes" chapter).

Only one lithologic unit has been recognized at Site 1143. Unit I can be divided into two Subunits, IA and IB, based on the carbonate content (Fig. F5). The sediments at Site 1143 represent continuous hemipelagic sedimentation of fine-grained terrigenous material and calcareous nannofossils from the late Miocene to present. The occurrence of minor lithologies in the core (ash layers, turbidite sediments, and green clay layers) varies with depth and also differentiates between Subunits IA and IB (Fig. F6).

F5. Sediment summary, p. 44.

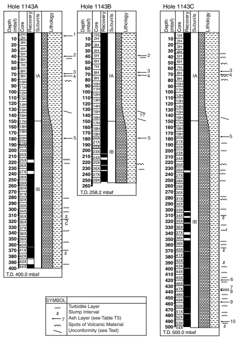

F6. Green clay layer frequency, p. 45.

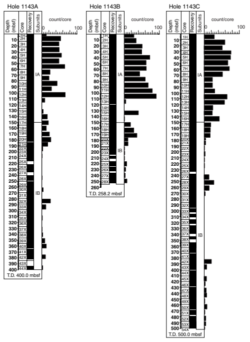

Subunit IA (0.0–160.0 mcd)

Interval: Core 184-1143A-1H through Section 184-1143A-17H-6, 30 cm; Core 184-1143B-1H through Section 184-1143B-17H-3, 90 cm; Core 184-1143C-1H through Section 184-1143C-17H-1, 120 cm
Depth: 0–153.2 mbsf (Hole 1143A); 0–151.8 mbsf (Hole 1143B); 0–150.1 mbsf (Hole 1143C)
Age: late Pliocene to Pleistocene

Subunit IA comprises the upper part of the sedimentary sequence in Holes 1143A to 1143C and consists of olive-gray, light grayish green, and greenish gray clayey nannofossil mixed sediment, clay with nannofossils, and clay. Bedding is not evident, and compositional changes are gradual. Sediment color changes related to varying carbonate content are observed throughout, with lighter layers having higher carbonate concentration. Carbonate content (nannofossils, foraminifers, and other forms of calcite, organic and/or inorganic), estimated by smear-slide analysis, is ~25%.

An oxidized red-brown clay layer is present in the top 3 cm of Holes 1143A and 1143B, whereas coring in Hole 1143C did not recover the mudline. Continuous to discontinuous layers and mottles of green clay are present throughout Subunit IA (Figs. F6, F7). Mottling is generally diffuse, and bioturbation intensity ranges from rare to common. Homogeneous patches of light yellowish to brownish gray nannofossil clay, sometimes with high concentrations of foraminifers and pyrite, are likely burrow fills.

F7. Green clay layer, p. 46.

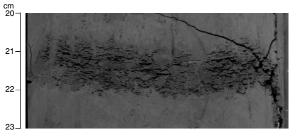

In addition to the dominant hemipelagic sediment, foraminifer ooze turbidites are noted within this subunit. These sediments are normally graded, often with a scoured basal contact on the underlying clayey sediment.

Several volcanic ash layers, ranging from 1 to 9 cm thick, are observed in Subunit IA (Table **T5**). These ashes have sharp bases and normal size grading, are unaltered, and are composed of angular glass shards and volcanic minerals. The thicker ashes are often dark colored, suggesting mafic composition, whereas the two youngest ash layers are thin, light-colored, and intensely bioturbated. Irregular spots of volcanic material are also detected in the upper 90 m of Subunit IA. The ash layers in Subunit IA tend to be thinner bedded (1 to 9 cm) than the Subunit IB ashes (1 to >20 cm).

T5. Volcanic ash layers, **p. 86.**

A possible unconformity, related to a sharp change in sediment color and marked by a steeply dipping horizon of black material (Fig. **F8**), is observed in Section 184-1143A-15H-5, 93–96 cm (133.0 mbsf; 140.0 mcd), and is also identified in FMS imaging (see **"Wireline Logging,"** p. 26). A similar horizon, suggesting an erosive boundary and likely the same unconformity, is in Section 184-1143B-15H-3, 107 cm (133.7 mbsf; 142.02 mcd), and in Section 184-1143C-16H-5, 50 cm (146 mbsf; 155.58 mcd). The boundary is horizontal in Holes 1143B and 1143C; thus the dip observed in Hole 1143A may be a drilling artifact.

F8. Inclined unconformity with black layer, **p. 47.**

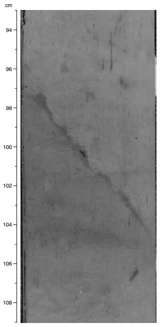

Subunit IB (160.0–512.4 mcd)

Interval: Section 184-1143A-17H-6, 30 cm, through Core 184-1143A-44X; Section 184-1143B-17H-3, 90 cm, through Core 184-1143B-28X; Section 184-1143C-17H-1, 120 cm, through Core 184-1143C-54X
Depth: 153.2–400.0 mbsf (Hole 1143A); 151.8–258.2.0 mbsf (Hole 1143B); 150.1–500.0 mbsf (Hole 1143C)
Age: late Miocene to late Pliocene

F9. Black ash layer, **p. 48.**

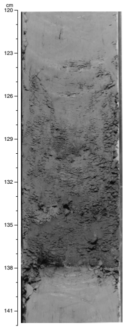

Subunit IB is characterized by a higher carbonate content and an increase in the frequency of turbidites compared with Subunit IA. Carbonate content increases rapidly below 150.0 mbsf, from ~25 wt% in Subunit IA to 30–45 wt% in Subunit IB. This change in composition is not clearly observed during visual inspection of the core, but smear-slide identification does indicate higher carbonate content compared to Subunit IA.

The dominant lithologies of Subunit IB are clayey nannofossil mixed sediment, nannofossil clay, and nannofossil ooze with clay. The green clay layers are not as frequent as in Subunit IA. Colored patches (presumably biogenic), bioturbation, and mottling are present in Subunit IB, without any clear change in proportion and significance from Subunit IA. Recognized trace fossils include *Zoophycos* and *Chondrites,* which are best observed between 240.0 and 512.4 mcd (~231.0–500.0 mbsf). Dark gray volcanic ash layers and volcanic breccias occur throughout this subunit (Fig. **F9**).

T6. Turbidite deposits, **p. 87.**

F10. Base of a coarse turbidite layer, **p. 49.**

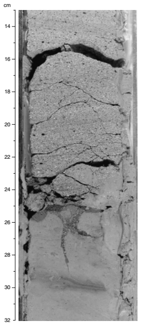

Major sedimentary structures observed in Subunit IB are slumps and turbidites (Table **T6;** Fig. **F10**). A 5-m-thick interval containing several slumps is observed in Core 184-1143A-36X from the top of the core to Section 36X-4, 50 cm (322.5 mbsf; 333.1 mcd). A 6.5-m-thick foraminifer sand turbidite is observed in intervals 184-1143A-37X-3, 25 cm, to 38X-1, 38 cm (336.8 mbsf; 348.4 mcd), and 184-1143C-36X-5 to 37X-2, 12 cm (336.0 mbsf; 348.4 mcd), but is only 4 m thick in this core. The upper part of this interval is composed of extremely homogeneous and structureless nannofossil clay and corresponds to the hemipelagic fine-grained E interval of the Bouma sequence (Bouma, 1962). The sediments at the base of the turbidite layer are more or less homogeneous foraminifer silt and sand. Flaser, oblique, and low-angle cross-lamination and normal grading are all recognized and testify to the current-dominated environment of deposition.

At the bottom of Holes 1143A and 1143C, where the sediment is more consolidated, offsets of laminations and burrows by microfaults are noted. The microfaults show an inclination of 40°–45° to the horizontal of the core. Motion is dominantly dip slip. A calcite-filled slickenside, observed in Section 184-1143A-44X-2, 76 cm (396.16 mbsf; 409.22 mcd), plunging at 10°–15°, indicates a sinistral component of displacement.

Dark brown to brownish black clay layers, characterized by high concentrations of siliceous material such as spicules, are observed in the lower part of Hole 1143C, below 430.0 mbsf (442.4 mcd). These layers often have parallel laminations and *Chondrites* traces at their top.

Discussion

Green Layers

The green layers are concentrated in the top 180 m of sediment, although they persist throughout the core. Smear-slide analysis indicates a nearly complete lack of calcareous and siliceous microfossils within these intervals, and a green mineral that resembles glauconite is observed under the microscope. However, X-ray diffraction analysis of bulk sediment from the green clay failed to confirm the presence of glauconite. The green layers are often discontinuous because of bioturbation and frequently occur as burrow fill and mottled intervals.

The origin of these green layers is enigmatic. Three formation schemes are possible: direct, rapid deposition of clay; alteration of volcanic ash layers; and dissolution and modification of the original nannofossil clay. One mechanism for the rapid deposition of clay is distal turbidites. However, this mechanism would likely also transport calcareous and siliceous microfossils to the site. The second alternative, alteration of volcanic ash layers, seems unlikely because unaltered ash layers are preserved within the nannofossil clay sequence throughout the entire section. Also, the frequency of the green intervals (the maximum approaches 100 green clay layers per core) would require extensive and sustained volcanism. Previous studies of “green layers” that are attributed to the alteration of volcanic ash (Lind et al., 1993; Gardner et al., 1986) describe a very different sedimentary feature: millimeter-scale color bands that overprint the surrounding sedimentary matrix where the color bands are diffuse in nature, that crosscut burrows and sedimentary layering, and that contain the same sediment components, including microfossils, as the surrounding matrix. In contrast, the green clay layers observed at Site 1143 occur as centimeter-scale deposits, are not observed to crosscut or overprint surrounding sedimentary features, are present as burrow fill and discontinuous layers (implying deposition or formation in the surface or near surface of the sediment column), and lack the calcareous microfossils of the surrounding nannofossil clay. The third hypothesis, selective dissolution of the original sedimentary matrix, could be possible under reducing conditions, perhaps caused by periods of intensive primary production in the region. However, no other sedimentary evidence indicates more intensive primary productivity. The origin of these green clay layers can only be determined by further analytical work.

Turbidites

Turbidites are common features at Site 1143. They can easily be correlated between the three holes on the basis of depth, thickness, and composition. Only four Bouma intervals, A (34 occurrences), B (30 occurrences), C (10 occurrences), and D/E (15 occurrences) (Bouma, 1962) were recognized. The A and B intervals are typically composed of foraminifer sands, with an occasional volcanic fraction. Since foraminifers have a low settling velocity because of their shape and low density, the turbidity currents did not have major erosional effect on the underlying sediment, as suggested by the lack of rip-up clasts. The basal turbidite sediments are often structureless or may display graded bedding or upper flow regime parallel laminations. The C intervals display different kinds of rippled beds, including flaser and contorted bedding. They can also be associated with syndepositional structures such as small-scale slumps, contorted bedding, water-escape structures, or soft-sediment faulting. Their composition mainly consists of silt-sized foraminifers with minor detrital input. The D/E intervals are difficult to differentiate here because parallel bedding could not be recognized, but the lack of bioturbation suggests episodic deposition.

The highest carbonate content noted at Site 1143 (84 wt%) is present in the coarse intervals of the calcareous turbidites (see **"Organic Geochemistry,"** p. 18). The planktonic/benthic foraminifer ratio is lower in these layers than in the hemipelagic sediment (see **"Biostratigraphy,"** p. 11), suggesting that they may have been transported from shallower depths.

Between 226 and 500 mbsf in Hole 1143C, the combined thickness of turbidites reaches 27.96 m, ~10% of the total section. This is a minimum estimate as some turbidites may have been obliterated by burrowing. This episodic sedimentation contributes to the increase in sedimentation rate noted in the lowest part of Site 1143 (see **"Sedimentation and Accumulation Rates,"** p. 17). The decrease in calcareous turbidites and slumping upsection may suggest a decreasing paleoslope at Site 1143 over the period represented by the cored interval.

BIOSTRATIGRAPHY

Calcareous Nannofossils

Calcareous nannofossils from Site 1143 were investigated in smear slides from core-catcher samples and from selected samples to better constrain the biohorizons. Site 1143 yielded abundant and well-preserved nannofossils in Holocene to Pliocene sections. In the upper Miocene, the nannofossils remained abundant, but their preservation gradually deteriorated downhole. The deterioration is indicated by increasing calcite overgrowth on discoasters and dissolution of placoliths, until finally the discoasters are difficult or impossible to identify to the species level. A complete calcareous nannofossil biostratigraphy for Site 1143 is based on the compilation of detailed studies on Hole 1143A and the lower part of Hole 1143C (see Tables T7, T8).

T7. Summary of biohorizons, **p. 90.**

T8. Calcareous nannofossil checklist, **p. 91.**

Emiliania huxleyi is present continuously from the top of Hole 1143A down to 13.2 mcd, assigning the interval to Zone NN21/CN15. A distinct decrease in the relative abundance of *E. huxleyi* from 2.9 mcd to 13.2 mcd constrains the uppermost 2.9-m interval to younger than 90 ka. The interval between 15.7 mcd and 26.8 mcd contains abundant

Gephyrocapsa spp. but lacks *E. huxleyi* and *Pseudoemiliania lacunosa;* it was assigned to Zone NN20/CN14b with an age range of 260 to 460 ka. At 27.7 mcd, the last occurrence (LO) of *P. lacunosa* marks the NN19b/CN14a to NN20/CN14b zonal boundary. Samples 184-1143A-6H-CC (53.7 mcd) and 7H-CC (63.4 mcd) contain rare to very rare, medium and large *Gephyrocapsa* spp. and an overwhelming dominance of various small *Gephyrocapsa* spp. (if excluding *Florisphaera profunda*): hence, these samples were assigned to the mid-Pleistocene small *Gephyrocapsa* acme zone (1.01–1.22 Ma). The next lower biohorizon, the LO of *Calcidiscus macintyrei,* was encountered at 74.2 mcd and indicates an age of 1.59 Ma (NN19a) for this stratigraphic level.

In terms of calcareous nannofossils, the Pliocene/Pleistocene boundary (1.77 Ma, Berggren et al., 1995) is located below the first occurrence (FO) of medium-sized *Gephyrocapsa* spp. (>4 mm; i.e., *Gephyrocapsa lumina, Gephyrocapsa carribeanica,* or *Gephyrocapsa oceanica*). This biohorizon has been dated at 1.69 Ma and is above the LO of *Discoaster brouweri,* which has an age of 1.95 Ma. The identification of the latter is unreliable at Site 1143 because of the consistent occurrence of reworked discoasters in the uppermost Pliocene and the lowermost Pleistocene. The process of redeposition will likely obscure the LO datum but will not affect the FO datum. The FO of medium-sized *Gephyrocapsa* spp. was identified at 93.5 mcd, but rare *D. brouweri* and *Discoaster pentaradiatus* also occurred in the same sample. *D. brouweri* is always very rare approaching its extinction level, and its LO is estimated at 94.3 mcd. Its abundance increases distinctly from 98.2 mcd downward. The LO of *D. pentaradiatus* is tentatively placed at 111.2 mcd because of its consistent occurrence and higher abundance below this level. The LO of *D. surculus* was found at 119.7 mcd, which assigns an age of 2.53 Ma to this level.

Sphenolithus abies and *Sphenolithus neoabies* are the last two survivors of sphenoliths, and they disappeared from the oceans in the latest Zanclean. Their highest occurrence in Hole 1143A was at 153.0 mcd, which assigns an age of 3.66 Ma to this level. *Reticulofenestra pseudoumbilicus* is identified here as specimens whose maximum diameter is larger than 7 μm in its uppermost range (the lower Pliocene), which is in accord with the size of the holotype (Gartner, 1967). Based on this definition, the LO of *R. pseudoumbilicus* is identified slightly below that of *S. abies* at 153.0 mcd. *Discoaster asymmetricus* occurred sporadically in the upper Miocene and the lowest Pliocene but became slightly more abundant and consistently present in samples above 195.2 mcd. This first “common” occurrence datum of *D. asymmetricus* is used to separate Zones NN13/CN11a and NN14/CN11b. The extinction of *Triquetrorhabdulus rugosus* (5.23 Ma) occurred shortly after the end of the Messinian and predates the evolution of *Ceratolithus rugosus* (5.1 Ma). These two datums are useful bioevents to constrain the Pliocene/Miocene boundary, but, unfortunately, they were not found in the uppermost Miocene and lowermost Pliocene at Site 1143. Thus, the Pliocene/Miocene boundary at Site 1143 is located between the FO (5.37 Ma) and LO (4.99 Ma) of *Ceratolithus acutus* at 213.0 and 200.6 mcd, respectively.

The LO of *Discoaster quinqueramus* was found at 220.7 mcd, which defines the upper boundaries of Zone NN11/CN9d and gives an age of 5.54 Ma to this level. *Amaurolithus amplificus* occurs at 244.0 through 259.7 mcd, which constrains this interval from 5.99 to 6.76 Ma. The oldest nannofossil datum documented in Hole 1143A is the FO of *Amaurolithus primus,* which is identified at 347.6 mcd. The interval from 357.8 mcd to 413.6 mcd yielded few *D. quinqueramus* and common *Discoaster berggrenii,* placing the bottom of Hole 1143A in Subzone CN9a (the lower part of Zone NN11).

Hole 1143C was drilled down to 500 mbsf, 100 m deeper than Hole 1143A, in expectation of penetrating the lower upper Miocene. The FO of *D. berggrenii* that defines the boundary between Zones NN10 (CN8) and NN11(CN9) was documented at 412 mcd, and it assigns an age of 8.2 Ma to this level. Sample 184-1143C-49X-CC (470.61 mcd) consists mostly of volcanic ash with few calcareous nannofossils. The nannofossil assemblage in this sample contains *Discoaster hamatus,* which occurred exclusively in Zone NN9, and Eocene to early Miocene species *Reticulofenestra umbilicus, Sphenolithus ciperoensis, Sphenolithus belemnos,* and *Sphenolithus heteromorphus*. This suggests that the deposition of volcanic ash was accompanied by extensive redeposition from older strata. Lithologies in the interval below Core 184-1143C-49X are very similar to those above. Nannofossil assemblages in the interval between Samples 184-1143C-50X-CC (480.0 mcd) and 54X-CC (512.9 mcd) indicate increased dissolution, whereas discoasters are very difficult to identify to species level because of heavy overgrowth. However, *Discoaster neohamatus* can still be recognized in these samples. This places the bottom of Hole 1143C in Zone NN9/CN7 with an age greater than 9.6 Ma (Berggren et al., 1995).

Planktonic Foraminifers

Planktonic foraminifers were examined from all core-catcher samples at Site 1143. Removing the clay in these samples often required soaking in a heated solution of equal parts Calgon, hydrogen peroxide, and tap water for several hours before washing through a 150-µm sieve.

Site 1143 yielded a moderate abundance of planktonic foraminifers, except for Sample 184-1143C-49X-CC (470.6 mcd), which consisted almost entirely of volcanic ash (glass) and very few planktonic foraminifers. Sample 184-1143A-31X-CC (289.1 mcd) also had a very low yield of foraminifers and contained mostly clay. Samples 184-1143A-37X-CC (347.6 mcd) and 184-1143B-35X-CC (327.4 mcd) yielded high amounts of planktonic foraminifers, possibly because of downslope transport.

Planktonic foraminiferal preservation at Site 1143 was good to very good, as documented by infrequent test breakage (fragmentation <10%), little to no evidence of dissolution or diagenetic alteration, the presence of delicate species such as *Beella digitata,* and the observation of numerous clear tests.

A complete planktonic foraminiferal biostratigraphy for Site 1143 is based on the compilation of detailed studies on Hole 1143A and the lower part of Hole 1143C (see Tables T7, T9 for complete details). The biostratigraphy of Site 1143 had several notable conventions and exceptions.

T9. Planktonic foraminifer checklist, p. 93.

Within Zone N22 we used the LO (0.12 Ma; Thompson et al., 1979) and FO (0.40 Ma; Li, 1997) of pink *Globigerinoides ruber* as biostratigraphic references. We noted that the LO of *Globigerinoides fistulosus* and the FO of *Globorotalia truncatulinoides* (bottom of Zone N22) occurred within Sample 184-1143-10H-CC (93.5 mcd) (Blow, 1969).

Within Zone N21, the LO of *Globorotalia multicamerata* was found to occur at a level corresponding to an age of 2.4 Ma instead of at its datum of 3.09 Ma. This observation is supported by studies of the South China Sea northern shelf (Wang et al., 1991). The bottom of Zone N21 was defined by the FO of *Globorotalia tosaensis* at 142.4 mcd. The coiling change of *Pulleniatina* spp. from sinistral to dextral (161.7 mcd) was quite distinct and served as a marker for the bottom of Zone N20. At Site 1143, *Sphaeroidinella dehiscens* disappeared within Zone N20, and so we were not able to use this species as a marker for the bottom of Zone N19. Thus, having only the FO of *Globorotalia tumida* to mark the bottom of Zone N18, we assigned the ages of several core catchers to Zones N19–N18 (213.0–241.0 mcd). The FO of common *Globorotalia margaritae* was used to help indicate the bottom of Zone N19 and the latest late Miocene.

Although *Pulleniatina primalis* was observed higher in the section, we did not find its FO to be a useful marker of the bottom of Subzone N17b. Instead, we relied on the FO of *Globigerinoides conglobatus* and *G. margaritae* as markers for Subzone N17b. Also, the coiling change of *Neogloboquadrina acostaensis* at 6.6 Ma (within Subzone 17a) was found to be inconsistent, and it was not used as a datum. We marked the bottom of Subzone 17a by both the LO of *Globigerinoides extremus* and *Globorotalia plesiotumida,* resulting in an age of 8.58 Ma. Because gradational forms of the species *N. acostaensis* and *Globorotalia mayeri* were observed from 452 mcd to 470.6 mcd, we assigned this interval to a combined zone of N15–N16 (8.58 to 10.49 Ma). Below this level and to the bottom of the hole, we observed typical *G. mayeri* and *Globoturborotalita nepenthes*. Thus, we assigned an age of <11.19 Ma (Zone N14) to the bottom of the hole (512.9 mcd).

Benthic Foraminifers

Although the paleontological focus of Leg 184 was to investigate calcareous nannofossils and planktonic foraminifers, we also tried to make note of the benthic foraminifers in the samples collected at Site 1143. Generally, Site 1143 yielded rare deep-sea benthic foraminifers that comprised ~3% of the total foraminiferal fauna. The proportion of benthic foraminifers increased markedly at ~44 and 224 mcd, possibly indicating high organic carbon flux and/or increased carbonate dissolution. The LO of one useful genus of benthic foraminifer *Stilostomella* was observed at 53.71 mcd, which indicates an age of ~0.75 Ma (Schönfeld, 1996) for this latitude.

Summary

At Site 1143, calcareous nannofossils are abundant and well preserved above the Pliocene, although preservation deteriorates through the Miocene. Planktonic foraminifers are abundant and have good preservation for the entire interval at this site. Benthic foraminifers are generally very rare but become more abundant in two short intervals.

An age-depth plot shows that biohorizons from the three fossil groups generally agree with each other (Fig. **F11**). The Pleistocene/Pliocene boundary is constrained by the FO of medium *Gephyrocapsa* spp., the LO of *G. fistulosus,* and the LO of *D. brouweri* and is located between 93.5 and 94.3 mcd. The Pliocene/Miocene boundary is constrained by the FO and LO of *C. acutus,* between 213.0 and 200.6 mcd. The sedimentation rate at Site 1143 has been calculated based on biostratigraphic data (Table **T7;** Fig. **F11**) and is 54 m/m.y. in the Pleistocene, 32 m/m.y. in the Pliocene, 63 m/m.y. in the uppermost Miocene, and 72 m/m.y. between 7.39 and 8.58 Ma. Below 432.8 mcd, the sedimentation rate was not calculated because the last two datums (LO *G. mayeri* and FO *D. neohamatus*) showed a wide disparity.

F11. Age-depth plot, **p. 50.**

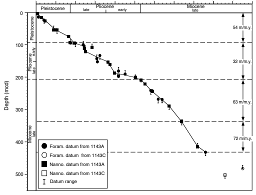

PALEOMAGNETISM

Shipboard paleomagnetic measurements for Holes 1143A, 1143B, and 1143C consisted of long-core measurements of natural remanent magnetization (NRM) at intervals from 2 to 4 cm before and after alternating field (AF) demagnetization, usually up to 20 mT (see **"Paleomagnetism,"** p. 12, in the "Explanatory Notes" chapter). Measurements were carried out on the archive halves of all APC and a large number of XCB cores. In this last case, however, intervals affected by coring disturbances, clearly visible as reoriented and broken or crumbled biscuits, were not measured. In addition, discrete samples were also collected from the working halves of Hole 1143A and Cores 184-1143C-42X through 53X, at a spacing of one sample per section (1.5 m). Most of these samples were subjected to progressive AF demagnetization up to 60 mT and were kept for shore-based rock magnetic analysis. Cores 184-1143A-4H through 21H, 184-1143B-3H through 19H, and 184-1143C-3H through 19H were oriented using the Tensor tool.

Hole 1143A

Long-core measurements were carried out at 2-cm intervals with AF demagnetization steps at 10 and 20 mT. The NRM is on the order of 10^{-3} A/m in APC cores and 10^{-4} A/m in XCB cores. This difference probably results from interference of the magnetization of partially reoriented biscuits on a scale smaller than the measuring bandwidth of the instrument (~15 cm) and from interference between the magnetization of reconstituted mud and that of the biscuits.

Below the first five to six cores, the NRM is almost invariably oriented parallel to the +X direction in the ODP coordinate scheme, which is orthogonal to the scribed double line on the core liner. Since the core liner is arbitrarily oriented with respect to the direction of the Earth's magnetic field, this is certainly an artifact. This orientation could derive from a radially inward magnetization induced by the coring process (Fig. **F12**) (Feary et al., 2000; Stokking et al., 1993). Inclinations are sometimes very shallow, although more often unrealistically steep. Alternating field demagnetization to 20 mT removed a large fraction (>70%) of the NRM, mainly along the z-axis (i.e., the axis along which the overprint is maximum) but could not isolate realistic paleomagnetic directions, even when demagnetization steps up to 60 mT were used.

Stokking et al. (1993) observed that the overprint was not as strong in discrete samples taken from the center of working-half sections, suggesting that the intensity of the overprint decreases radially from the edge to the center of the core. For this reason, we have taken discrete cubic samples (one from the center of each section of the different cores). Alternating field demagnetization of these samples to 60 mT yielded very good quality demagnetization results (Fig. **F13**). The final direction, however, was still highly contaminated by the overprint. A possible explanation is that the coercivity spectrum of the overprint and of the primary magnetization largely overlap, so that AF demagnetization removes both components simultaneously.

This strong overprint hindered retrieval of reliable paleomagnetic directions from most of the core. Tensor-corrected declination and inclination values obtained from long-core measurements for 0–100 mcd after demagnetization at 20 mT are reported in Figure **F14.** The first three cores were not oriented, so declinations have no meaning. After

F12. Explanation of the 0° declination observation, **p. 51.**

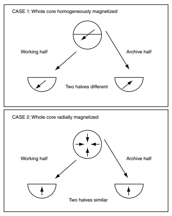

F13. AF demagnetization to 60 mT of Sample 184-1143A-7H-4, 93 cm, **p. 52.**

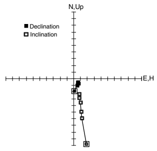

F14. Tensor-corrected declination and inclination, Hole 1143A, 0–100 mcd, **p. 53.**

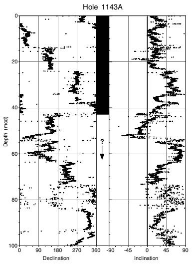

reorientation using Tensor tool data, Core 184-1143A-4H has a declination of 260° and a normal inclination too steep for the latitude of the site, indicating some contamination from the overprint. Despite the contamination, we have interpreted this core as indicating normal (Brunhes) polarity. Core 184-1143A-5H has a positive inclination of ~15° (with an unexplained peak to very steep values) and declination of ~360°, except in the bottom ~1 m, where the declination starts pointing to nearly 180°. A transition to negative inclinations with south-seeking declination is clearly visible in Core 184-1143A-6H at ~42.5–43.8 mcd. We interpret this transition as the Brunhes/Matuyama polarity reversal.

Below this depth, the results are difficult to interpret. A short interval of normal declination occurs at the bottom of Core 184-1143A-6H and the top of Core 7H from 51.8 to 54.2 mcd. Core 184-1143A-7H has an average declination of ~150°, indicating continued reversed declinations. However, inclinations have unrealistically steep values (~70°), suggesting pervasive drill-string overprint. Core 184-1143A-8H has reversed declination (~220°) but a shallow positive inclination. Core 184-1143A-5H shows high scattering of both inclination and declination with a slightly lower intensity, possibly indicating another type of coring disturbance.

Farther downcore, the measurements produce unrealistically rapid changes in inclination and declination with both reverse and normal polarity in both APC and XCB cores. Figure **F15** shows inclination and uncorrected declination from 110 to 180 mcd after AF demagnetization at 20 mT. The uncorrected declinations cluster around 0°, indicating a radial overprint as mentioned above. This ambiguity could not be resolved using data from discrete samples.

F15. Declination and inclination data, Hole 1143A, 110–185 mcd, **p. 54.**

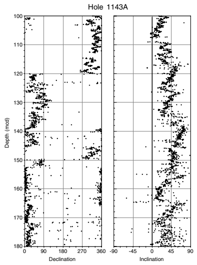

Hole 1143B

To mitigate the overprint observed in Hole 1143A, nonmagnetic core barrels and cutting shoes were used every second core in Hole 1143B (only one nonmagnetic assembly was available on board). This assembly was used during Leg 182 with some encouraging results (Feary et al., 2000).

At Hole 1143B, unfortunately, the nonmagnetic assembly did not produce any improvement in the quality of the data. The overprint appeared to be just as large in cores taken with the nonmagnetic assembly as in those taken with the standard assembly. Overall, the results are just as disappointing as in Hole 1143A.

Inclinations are ~15°–20° for the upper 43 m, followed by a transition to negative values. This could indicate the presence of the Brunhes/Matuyama boundary at this level. The declinations corrected with the Tensor tool data (starting at 28 mcd) are predominantly south seeking, in contrast to the inclination data. However, a clear declination change of nearly 180° at 43.2 mcd in the middle of Core 184-1143C-5H correlates with the inclination change to negative values and suggests that this could be the Brunhes/Matuyama reversal.

Farther downcore, the results are difficult to interpret. Numerous 180° changes occur in declination—sometimes between different cores and sometimes within a core, such as the one observed at 88 mcd. However, inclination data are very scattered and are predominantly positive. A polarity stratigraphy is therefore impossible to retrieve from these results.

Hole 1143C

In an additional attempt to lessen the overprint, the nonmagnetic shoe was used with a standard core barrel on every second core in Hole 1143C. This hybrid assembly produced good results during Leg 182 and was suggested to us by Mike Fuller (pers. comm., 1999). Unfortunately, it did not reduce the overprint. In fact, the nonmagnetic cutting shoe actually produced a steeper vertical overprint than that of the standard cutting shoe (Fig. F16). In the end, the lack of results from Hole 1143C was similar to that from Holes 1143A and 1143B.

No reliable magnetostratigraphy could be obtained from this hole.

F16. Inclination of cores cut with a nonmagnetic and a standard cutting shoe, p. 55.

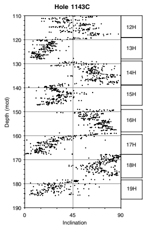

Nature of the Overprint

Long-core measurement of both the archive and working halves, occasionally made at different depths, usually gave the same result, providing clear evidence for the presence of a radially inward horizontal magnetization component. If this component were the only overprint, it would correspond to inclinations close to 0°. This is not usually the case; in fact, inclinations are more often quite steep. Therefore, a vertical component related to drill-string remagnetization is also present in the overprint. Both components appear to be less intense in the upper part of each hole. Above 50 mcd the vertical overprint seems to be more transient, often occurring in the top several meters of the various cores. A strong radial overprint is observed in most cores below ~50 mbsf. The relative intensity of the two components varies along the cores, suggesting that some physical properties of the sediment itself may play a role in the acquisition of the overprint. The core barrel assembly also has a very strong effect on the overprint. The average inclination of the cores recovered using the standard assembly is clearly different from that of the cores where the nonmagnetic assembly was used. In either case, the overprints are pervasive and could not be removed by either AF or thermal demagnetization. Therefore, the primary magnetization proved impossible to recover below ~50 mcd.

SEDIMENTATION AND ACCUMULATION RATES

Paleomagnetic analysis provided only one age control point at Site 1143; namely, the Brunhes/Matuyama boundary (0.78 Ma, 43.2 mcd). Thus, the age model of Site 1143 is based primarily on biostratigraphy. The combined calcareous nannofossil and foraminiferal biostratigraphy yielded 39 event levels and age assignments, using the shipboard stratigraphic framework (see "Biostratigraphy," p. 9, in the "Explanatory Notes" chapter). Of those, 21 are based on nannofossils, 17 on planktonic foraminifers, and one on benthic foraminifers. Because of limited sampling (mainly core-catcher samples) and some redeposition, a certain amount of depth uncertainty is associated with the datum levels in Table T7. Particularly controversial in age are bioevents of two fossil groups near the bottom of the hole: the LO of *G. mayeri* (10.49 Ma) at 480.03 mcd and the FO of *D. neohamatus* (9.6 Ma) at 488.79 mcd. The latter is used for calculations presented in this volume.

Figure F17 (also given as Synergy Software KaleidaGraph plots and Microsoft Excel data files [see the "Supplementary Materials" contents list]) shows the linear sedimentation rate (LSR) and mass accumulation rate (MAR) curves based on calculations described in "Sedimentation

F17. Age-depth model, LSR, and MAR, p. 56.

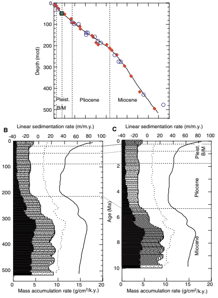

and Accumulation Rates," p. 13, in the "Explanatory Notes" chapter. The results show a high sedimentation rate before 6–7 Ma (60–80 m/m.y.), decreasing sedimentation rates toward the Pliocene (~30 m/m.y.), and rising sedimentation rates in the late Pleistocene (>50 m/m.y.) (Table **T10**). The carbonate accumulation rate decreases from nearly 4 g/cm^2/k.y. ~7 m.y. ago (with relatively high values until the end of the Miocene [~2 g/cm^2/k.y.]) to ~0.6 g/cm^2/k.y. in the last 0.8 m.y. Noncarbonate accumulation rates show high values in the Miocene, exceeding 4 g/cm^2/k.y. before 7 Ma, but they increase slightly at ~3 Ma (Fig. **F17C**), unlike carbonate accumulation. The remarkable variations in accumulation rates of biogenic carbonate and mainly terrigenous noncarbonate material yield significant paleoenvironmental information.

T10. Sedimentation and accumulation rates for selected intervals, **p. 94.**

In order to understand the changes more precisely, the sum of all recognizable turbidites or slump thicknesses (see **"Lithostratigraphy,"** p. 8) is subtracted from the total sediment thickness for each time interval. The "corrected thickness" is then used for re-estimating the average accumulation rate, as well as the carbonate and noncarbonate accumulation rates (Table **T11**). As seen from the table, sediment redeposition is negligible (<1%) for the upper part (Pliocene and Pleistocene) but significant (~10%) for the lower part of the section (upper Miocene). This redeposition should be taken into account when the sedimentation history is interpreted.

T11. Corrected sediment thickness, **p. 95.**

ORGANIC GEOCHEMISTRY

At Site 1143, the shipboard organic geochemistry analysis consisted of determinations of total organic carbon (TOC), total carbon (TC), total nitrogen (TN), total sulfur (TS), and carbonate as well as Rock-Eval pyrolysis and hydrocarbon (HC) monitoring. The analytical procedures are outlined in **"Organic Geochemistry,"** p. 14, in the "Explanatory Notes" chapter.

Volatile Hydrocarbons

As part of the shipboard safety and pollution-prevention monitoring program, hydrocarbon gases were analyzed in every core of Hole 1143A and in the lower 100 m of Hole 1143C (Cores 184-1143C-44X through 54X) by the headspace (HS) technique. No gas expansion voids or hydrates were observed. Only trace amounts of methane (≤10 ppmv) were detected, and no ethane was found in the headspace gas. Higher methane values were in the top 120 m; below this level, concentrations decreased, slowly increasing again in the bottom 190 m of the hole (especially Cores 184-1143C-49X through 54X), partly because of increased sample size. Because the values were so low, a headspace vial and cap without sediment were similarly analyzed with a result of 1.9 ppmv methane, approximately the minimum value recorded downcore. This corresponds to the ambient atmospheric methane concentration in the laboratory. Low methane concentrations at Site 1143 may have resulted either from very low levels of TOC or because sulfate reduction was not complete (see **"Inorganic Geochemistry,"** p. 20). Therefore, methanogenic bacteria were not able to successfully compete for organic matter.

Inorganic Carbon

Analytical methods for inorganic carbon (IC), TC, and TOC determination are discussed in **"Inorganic Geochemistry,"** p. 17, in the "Explanatory Notes" chapter. Sampling was conducted in three sections per core for carbonate and at least one sample per core for carbon-nitrogen-sulfur (CNS) analysis. Carbonate varies generally from 10 to 60 wt%, with only four values above and four below this range. The carbonate plot (Fig. **F18**) tends to mirror that of TOC (Fig. **F19**) in the upper 200 mcd (Cores 184-1143A-1H through 21H), suggesting that the carbonate concentrations reflect varying amounts of noncarbonate sediment input (e.g., clastics and admixed volcanic ash). Below this depth, carbonate values rise markedly from ~20 wt% in the upper 150 mcd to an average of 45 wt% below that depth. Below 300 mcd, carbonate increases to ~50 wt% to the bottom of the hole. The higher carbonate content is also reflected in the interstitial water Ca^{2+} and alkalinity data (see **"Inorganic Geochemistry,"** p. 20). Two exceptionally high carbonate samples at 413 and 433 mcd were remeasured and confirmed as calcite rich and are coincident with foraminifer sand layers.

F18. Carbonate values vs. depth, **p. 57.**

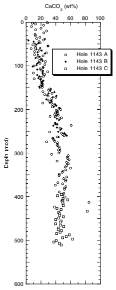

Organic Carbon

The TOC values at Site 1143 are consistently low (mostly between 0.1 and 0.4 wt%) except in the top 70 m of the core, where half of the data are between 0.4 and 0.6 wt% (Table **T12**). The percentage of TOC declines rapidly from >0.3 wt% in the upper 70 m (Cores 184-1143A-1H through 8H) to <0.3 wt% throughout the remainder of the hole, except Sections 184-1143A-30X-4 and 33X-3. These latter samples were characterized by higher TOC (>0.8 wt%) and correspond to two discrete samples with lower carbonate concentrations.

Calculated C/N ratios are remarkably low (Table **T12**). A value of 5 to 6 indicates that most of the organic matter is derived from fresh marine phytoplankton. However, the low values (<5) measured on samples from Site 1143 are likely an artifact caused by a combination of very low organic carbon concentrations and the absorption of ammonium-nitrogen by abundant clay minerals (see **"Organic Geochemistry,"** p. 11, in the "Site 1145" chapter), (Müller, 1977).

F19. Total organic carbon (by difference) values vs. depth, **p. 58.**

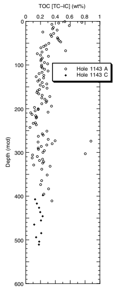

T12. IC, $CaCO_3$, TC, TOC, Rock-Eval, TN, and TS contents, **p. 96.**

Sulfur Analysis

One hundred samples were analyzed for CNS content, but many were found to give low or zero values (there is no SO_2 peak). The problem is sorption or reaction of SO_x on the CaO that remains in the furnace. Total sulfur varies from 0.1 to 0.8 wt%, with most values ranging from 0.1 to 0.4 wt% (Table **T12**). We assume that this is all pyrite-S because pyrite is observed in many cores as thin burrow fillings and fine-grained black concentrations.

Rock-Eval Analysis

Rock-Eval pyrolysis analysis was made on seven samples with higher TOC (by difference) values. The results are presented in Table **T12.** The sample from Section 184-1143A-30X-4 was run in duplicate with two different masses. The reproducibility for the replicate analysis is quite good, with precision of better than 10 wt% for all parameters. Rock-Eval TOC and TOC by difference (TC – IC) do not agree. On only one sample do the results by both methods agree; on the other samples, Rock-Eval shows TOC values from 15 wt% to a factor of 4 lower than TOC by difference. The two samples that show the best agreement in TOC are also those with the highest TOC values. It is unclear whether the TOC values obtained by subtracting a carbonate value >96 wt% of the TC value, or by Rock-Eval analysis, are more reliable at such low concentrations. However, a possible systematic error in the by-difference method does not invalidate the discussion of relative TOC variations with carbonate. Because of the low TOC, none of the other Rock-Eval parameters is considered reliable (Tissot and Welte, 1984) and cannot be used to examine the origin of the organic matter at this site.

Contamination

All routine headspace samples were taken from sediment exposed during division of the core on the catwalk, usually from the upper 5 cm of Section 4. Sediment disturbance during extended core barrel usage, especially below 250 meters below seafloor, may have resulted in some of HS samples containing mainly drilling-disturbed sediment. For this reason, an aliquot of interval 184-1143A-29X-1, 145–150 cm, was also analyzed on the natural gas analyzer (see **“Organic Geochemistry,”** p. 14, in the “Explanatory Notes” chapter). A very marked C_5 peak, with a concentration of 3376 ppmv, was noted. Upon further investigation, a similar result was obtained from Section 184-1143A-27X-CC, and the source was identified as acetone contamination (liberally used to seal section end-caps). Such an isolated peak without HC homologues should be immediately regarded as contamination, a valuable indicator for future organic geochemical analyses.

INORGANIC GEOCHEMISTRY

Inorganic chemical analyses were conducted on 23 interstitial water samples squeezed from whole-round samples at a frequency of one per core in the first six cores and one every third core thereafter from Holes 1143A and 1143C. Analytical methods are detailed in **“Inorganic Geochemistry,”** p. 17, in the “Explanatory Notes” chapter. The concentrations of dissolved interstitial constituents are presented in Table **T13**, and the profiles with depth are shown in Figure **F20.** Interstitial water profiles at Site 1143 are characteristic of sediments in which sulfate reduction and volcanic ash alteration are the primary reactions controlling the concentrations of dissolved constituents.

T13. Interstitial water composition, **p. 100.**

F20. Interstitial water measurements, **p. 59.**

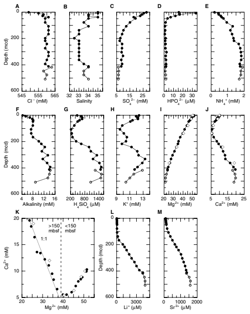

Chloride and Salinity

Chloride (Cl^-) concentrations in interstitial waters at Site 1143 are relatively constant, ranging from 549 to 563 mM (Fig. **F20A;** Table **T13**). A small increase in the Cl^- concentration occurs from 549 mM near the surface to 561 mM at 35.9 mbsf. Below this depth, the Cl^- concentration does not significantly change. Interstitial water salinities fluctuate between 33 and 35 (Fig. **F20B;** Table **T13**), with higher values in the uppermost section. The decrease in salinity observed from the top 0 to ~120 mbsf is probably a result of the removal of dissolved sulfate from interstitial waters during sulfate reduction.

Sulfate, Phosphate, Ammonium, Alkalinity, and pH

The major changes reflected in the sulfate (SO_4^{2-}), ammonium (NH_4^+), phosphate (HPO_4^{2-}), and alkalinity profiles from 0 to ~200 mbsf are interpreted to be caused by the diagenesis of organic matter via sulfate reduction. This process has led to the depletion of dissolved sulfate in interstitial waters by the sulfate reduction reaction (Emerson et al., 1980):

$$53SO_4^{2-} + C_{106}H_{263}O_{110}N_{16}P =$$

$$39CO_2^- + 67HCO_3^- + 16NH_4^+ + 53HS^- + 39H_2O + HPO_4^{2-}.$$

In this process, SO_4^{2-} is consumed, and alkalinity (i.e., HCO_3^-), NH_4^+, and HPO_4^{2-} are byproducts.

Dissolved SO_4^{2-} concentrations decrease from seawater values at the top of the core to 7.3 mM at 200 mbsf but never reach zero for the remainder of hole, indicating that sulfate reduction is incomplete (Fig. F20C; Table T13). Incomplete sulfate reduction suggests that methanogenesis is not an important process in these sediments, which is in agreement with the low methane values measured in sediment (<10 ppmv) (see **"Organic Geochemistry,"** p. 18). A deep zone of sulfate reduction also jibes with the relatively low organic matter contents at this site (see **"Organic Geochemistry,"** p. 18). In addition, the HS^- produced during organic matter diagenesis is likely to react with iron to form "iron sulfide" minerals (e.g., "FeS" and "FeS_2"), a conclusion supported by the fact that no H_2S was detected at Site 1143 (see **"Organic Geochemistry,"** p. 18). Disseminated pyrite as well as pyritized burrows were observed throughout much of the core (see **"Lithostratigraphy,"** p. 8).

As a result of sulfate reduction, dissolved HPO_4^{2-} concentrations show a distinct peak of 33.7 mM at 7.35 mbsf and then decrease rapidly to ~1.6 mM at 73.9 mbsf (Fig. F20D; Table T13). Sulfate reduction is also reflected in the NH_4^+ profile (Fig. F20E; Table T13), which has an inverse relationship with sulfate. The NH_4^+ concentration increases continuously in the sulfate-reduction zone to 1.4 mM and then is constant to the base of the hole.

Alkalinity increases from 4.3 mM at 1.45 mbsf (slightly higher than the 2.3 mM seawater value) to a maximum of 8.0 mM around 35.8 mbsf (Fig. F20F; Table T13), then declines slowly to a minimum of 7.3 mM around 102.3 mbsf before increasing again to reach 13.9 mM at the base of the Hole 1143A (398.3 mbsf). Increasing alkalinity in the uppermost interval may be attributed to HCO_3^- production accompanying sulfate reduction. The alkalinity increase below the zone of major sulfate reduction indicates some other source of alkalinity. However, pH remains in a narrow range (7.23–7.96) throughout the entire sedimentary column (Table T13).

Silica and Potassium

Silica (H_4SiO_4) climbs sharply from surficial values of 476 mM to a maximum of 693 mM at 16.9 mbsf before steadily declining to a minimum of 220 mM at 102.3 mbsf (Fig. F20G; Table T13). Between 75 and 160 mbsf, H_4SiO_4 concentration values are low (<300 mM). Below this interval, H_4SiO_4 concentrations gradually increase to a maximum value of 1467 mM at the bottom of Hole 1143A. The two high H_4SiO_4 concentration intervals (0–75 mbsf; 160–400 mbsf) are associated with intervals of higher biogenic silica content (see **"Lithostratigraphy,"** p. 8) and may result from the high solubility of amorphous, biogenic silica (opal-A).

Dissolved potassium concentrations (K^+) decrease downhole from ~12.4 mM near the surface to 9.5 mM at 102.4 mbsf, and the profile then has a small positive inflection in the interval at 100–200 mbsf (Fig. **F20H;** Table **T13**). Below this interval, the K^+ increases to 13.3 mM at 321.7 mbsf and decreases to 11.7 mM at the bottom of Hole 1143A. The interval of low values in the K^+ concentration is also characterized by low values of the H_4SiO_4 and corresponds to the interval in which large numbers of green clay layers are observed in the sediments (see **"Lithostratigraphy,"** p. 8). The decrease of K^+ in this interval may reflect uptake of K^+ during clay mineral formation or alteration.

Magnesium, Calcium, Lithium, and Strontium

Magnesium concentrations (Mg^{2+}) decrease linearly with depth from near-seawater values at the top (51.5 mM) to a minimum of ~23.7 mM at the bottom of Hole 1143A (Fig. **F20I;** Table **T13**). The profile of dissolved calcium concentration (Ca^{2+}) decreases from near-seawater values at the surface (10.3 mM) to 5.5 mM at ~102.4 mbsf (Fig. **F20J;** Table **T13**). Below this level, Ca^{2+} increases continuously, reaching maximum values of 19.6 mM near the bottom of Hole 1143A. The Ca^{2+} minimum suggests that sulfate reduction and alkalinity production are promoting inorganic calcite precipitation in the upper 100 mbsf (Fig. **F20I;** Table **T13**).

The slope of the Ca^{2+} vs. Mg^{2+} relationship is positive and close to unity below 150 mbsf (Fig. **F20K;** Table **T13**), suggesting the loss of 1 mM of Mg^{2+} for every gain of 1 mM Ca^{2+}. This exchange of cations suggests that alteration of volcanic materials may be driving the concentrations of these elements in the interstitial waters. Calcium increases and magnesium decreases downhole can reflect upward diffusion of the signal of chemical alteration in underlying oceanic crust, or in situ alteration of volcanic material to smectite in the sediment. Although we do not know the composition of the basement rock, a number of volcanic ashes are observed throughout the sediments at this site (see **"Lithostratigraphy,"** p. 8).

The upper part of the lithium (Li^+) profile exhibits a minor increase in concentration from the top to 88 mM at ~100 mbsf (Fig. **F20L;** Table **T13**). Below this depth, the Li^+ strongly increases, reaching the unusually high values of 3940 mM in interstitial waters near the bottom of Hole 1143A. The low values in Li^+ concentrations at the top of Hole 1143A are probably a result of Li^+ uptake during authigenic calcite precipitation. Dissolved strontium concentrations (Sr^{2+}) increase from 93 mM near the top of Hole 1143A to 1367 mM at the bottom (Fig. **F20M;** Table **T13**). The increases in both Li^+ and Sr^{2+} concentrations below 100 mbsf most likely reflect dissolution of biogenic silica and/or reactions involving dissolution of volcanic glass.

The alkalinity, K^+, H_4SiO_4, Li^+, and Ca^{2+} profiles all increase substantially below 200 mbsf (Fig. **F20;** Table **T13**). This interval corresponds to lithologic Subunit IB, which was recognized primarily based on its higher carbonate content (see **"Lithostratigraphy,"** p. 8). This higher carbonate interval also corresponds to the major increase in density and decrease in porosity in the downhole logs (see **"Wireline Logging,"** p. 26) and in the physical properties measurements (see **"Physical Properties,"** p. 23). These changes in lithology and physical properties may contribute to the interstitial water profiles by increasing the availability of carbonate for dissolution and recrystallization processes and by reducing the diffusional capacity of the sediments so that signals of sediment/water interactions are more localized within lithologic Subunit IB.

PHYSICAL PROPERTIES

Sampling

At Site 1143, physical properties were measured on whole-round sections, split-core sections, and discrete samples from the latter. Whole-core logging with the multisensor track included GRA bulk density, MS, and NGR on all cores as well as *P*-wave velocity logging from the top of the holes down to Sections 184-1143A-22X-3, 184-1143B-20X-1, and 184-1143C-21X-1. Sampling intervals were 2 cm for Hole 1143A and 4 cm for Holes 1143B and 1143C (except for Cores 184-1143C-13X and 14X, which were measured at 2-cm intervals). The *P*-wave logger (PWL) data were bad because of instrument problems and/or cracks or a void in the sediment cores. One to two thermal conductivity measurements per core were also performed on the whole-round sections. Color reflectance (CR) was measured on the archive halves of all split cores, at 2-cm sampling intervals for Holes 1143A and 1143B and at 4-cm intervals for Hole 1143C. Moisture, density, and *P*-wave velocity (using the *P*-wave velocity sensors 1, 2, and 3 [PWS1, PWS2, PWS3]) were measured on discrete samples from split-core sections at intervals of one measurement per section (1.5 m) (see **"Physical Properties,"** p. 18, in the "Explanatory Notes" chapter).

Results

Core physical properties measurements show three first-order features. One is related to the change from APC to XCB coring (201.1 mcd in Hole 1143A, 184.3 mcd in Hole 1143B, and 187 mcd in Hole 1143C). The XCB cores are disturbed significantly by biscuiting, partial remolding, and incorporation of drilling slurry. In addition, XCB cores are reduced in diameter by ~10%. This affects the GRA bulk density and, to a smaller degree, signals from instruments that measure constant volumes such as MS and NGR. This effect is not compensated for because time is not available to perform a careful correction on board ship.

The other two primary features are related to lithologic changes. The first is defined by a downhole change in grain density, a prime indicator of changes in mineralogy, between ~150 and ~190 mcd. The second is marked by repeated inversions in the downhole trend of porosity and related properties that form two apparently anomalous intervals at ~200–300 mcd and ~360–410 mcd. These features are described in more detail in the following sections.

Grain Density, Bulk Density, and Porosity

In Hole 1143A, between ~150 and 200 mcd, there is a major change in grain density (Fig. **F21**) that is compatible with the increase in car-

F21. Grain density measurements, **p. 60.**

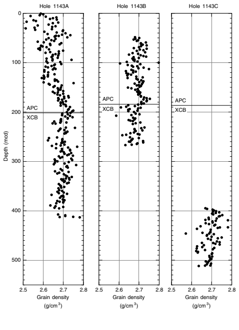

bonate over this interval (Fig. **F18**; see **"Organic Geochemistry,"** p. 18). Above this transitional interval, the carbonate mean values and standard deviations are 19 ± 7%, and below the interval they are 45 ± 10 wt%. This compares to grain density values above and below the transition interval of 2.66 ± 0.05 g/cm^3 and 2.70 ± 0.04 g/cm^3, respectively. A preliminary calculation indicates that the increased carbonate concentration accounts for only half the average increase in grain density. Therefore, the grain density of the noncarbonate component must also increase downhole.

Especially in the interval between 150 and 250 mcd, the GRA bulk density shows cycles that span the lengths of cores (Fig. **F22**). The lower parts of these core cycles show densities higher by ~0.01 g/cm^3 relative to the upper parts. These cycles give us a clear example of how the coring process changes the physical properties of the sediment. With the APC technique, core compression and stretching that result from the coring process probably have the strongest influence on the sediment properties. Cycles in the GRA data, when drilled with the XCB, may represent a function of the time that the sediment had been exposed to drilling vibrations.

F22. Bulk density measurements from GRA and MAD methods, **p. 61.**

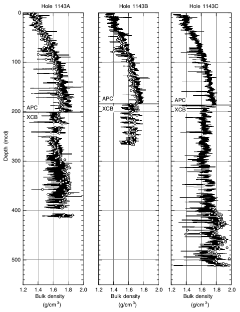

Between ~180 and ~190 mcd (the exact position depends on the hole), GRA bulk density shows a sharp decrease resulting from the change to XCB coring (Fig. **F22**). The effect of the reduced diameter on GRA measurements becomes very clear when compared with the more accurate bulk density data obtained from the moisture and density (MAD) method, which reveal a much smaller offset at that depth. Figure **F23** illustrates how GRA and MAD data correlate much better for APC than for XCB cores. In the XCB section, the GRA values are noisy with a bias to lower values because measurements of remolded sediment and drill slurry are included. The highest GRA values, obtained randomly from intact core pieces, are reliable because they correspond to the MAD values obtained from selected, intact core pieces.

F23. Comparison of bulk density measurements from GRA and MAD methods, **p. 62.**

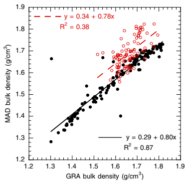

Porosity data indicate a compaction trend that varies between two simple envelope trends (Fig. **F24**). The envelopes are power curve fits to extreme values at a number of depth intervals and represent homogeneous lithology and compaction end-members at Site 1143. The same characteristics are also observed in the MAD bulk density record (Fig. **F22**), which is largely related to porosity. The uppermost 0–150 m of the section (and the interval between ~300 and ~360 mcd) appear to approach the higher density, lower porosity envelope, whereas the intervals between ~150–300 mcd and 360–420 mcd approach the lower density, higher porosity envelope. The most striking porosity inversion, between 200 and 300 mcd, is also one of the most characteristic features in the wireline logging records of this site (see **"Wireline Logging,"** p. 26). The bulk density excursion is as much as 0.2 g/cm^3; the porosity inversion, as much as 12%.

F24. Porosity values obtained from the MAD method, **p. 63.**

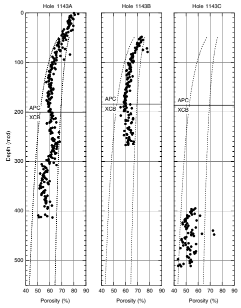

Grain density values also mirror these variations to a lesser degree and indicate a lower carbonate content (lower grain density values) in the higher porosity intervals (e.g., 200–300 mcd). This observation is not compatible with the simple assumption that more carbonate increases bulk density and reduces porosity. Higher porosity with increased carbonate could be explained by an increased amount of foraminifers slowing compaction. This hypothesis is supported by the observation of foraminifer turbidite layers, most of which could have been reworked into the sediment by bioturbation and thus would not be accounted for by tabulating preserved sand layers.

Magnetic Susceptibility and Natural Gamma Radiation

Both MS and NGR records show the most significant decrease in values near the transition to XCB coring (Figs. **F25**, **F26**). Both measurements are volume specific, and their absolute values are affected by core disturbance that reduces the average bulk density. A good example is that the core-stretching effect at the base of the APC section, shown so well on the GRA record, can also be observed in the NGR data. Much of the general downhole increase in MS and NGR values from 0 to 180 mcd can be accounted for by the overall decrease in porosity.

The change from APC to XCB coring and its effect on the MS and NGR data, however, may well be related to a change in lithologic parameters, such as a pronounced increase in stiffness resulting from the increasing carbonate content. The drop in the MS signal does not occur exactly at the change to XCB cores but ~10 m above. Also, the drop in magnitude from ~25 × 10^{-5} to ~10 × 10^{-5} SI in MS, and from ~35 to 25 counts per second (cps) in NGR, cannot be fully explained by the decrease in bulk density as a result of coring disturbance. The decrease in MS and NGR at ~185 mcd, therefore, represents a significant lithologic change at Site 1143.

The NGR, which generally provides a rough estimate of the clay abundance, also shows a slight decrease in values between 130 and 180 mcd (Fig. **F26**). This cannot be explained either by coring effects and associated porosity changes or by changes in carbonate content, which does not increase until 30 m farther downhole. A decrease in the abundance of the radioactive component (e.g., clays such as illite) may therefore occur in that interval.

The MS shows a number of significant spikes that correspond to observations of volcanic ash layers. The spikes are particularly abundant in the intervals 20–30 and 70–100 mcd (Fig. **F25**) and also appear between 120 and 190 mcd in the record from Hole 1143A.

F25. Magnetic susceptibility measurements, **p. 64.**

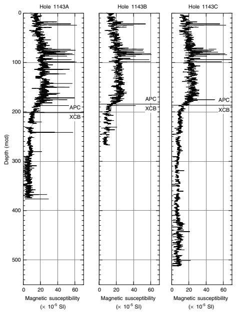

F26. Natural gamma radiation measurements, **p. 65.**

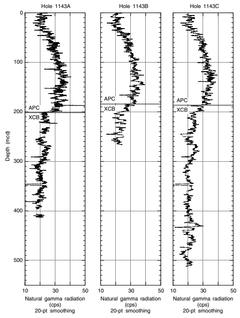

Color Reflectance

The CR data are presented as records of two parameters from the L*a*b* color system: L*, representing the lightness in percent; and a*/b*, the ratio of the two chromaticity parameters (Fig. **F27**). L* can be used as a first-order approximation of the relative concentration of carbonate. The major increase in carbonate between 150 and 200 mcd is represented by an increase in L* from ~50% to 58%. More subtle trends in carbonate concentration and the L* record appear to correlate as well, although the sampling intervals for carbonate are presently too low for a rigorous analysis of the relationship. The a*/b* ratio is a proxy for color change that can be related to a combination of carbonate or organic matter content, clay mineralogy, oxidation, and so forth. This parameter shows a sharp decrease at ~200 mcd and regains its amplitude at ~280 mcd.

F27. Color reflectance measurements, **p. 66.**

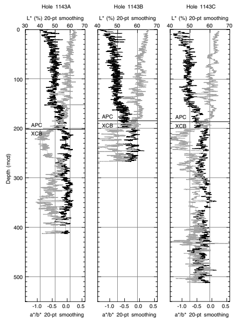

P-wave Velocity

Because of technical problems, the value of the PWL measurements is very limited. A comparison of PWS3 and PWL measurements reveals that the PWL significantly underestimates *P*-wave velocities. No useful data can be obtained from XCB cores. For these reasons, the PWL data are not shown in this text.

In the uppermost 150 mcd, PWS3 data range from 1600 to 1800 m/s and show little variability (Fig. **F28**). Below that depth, values increase uniformly to ~1900 m/s at 320 mcd, presumably as a result of compaction and also, perhaps, because of the increase in carbonate content. In the interval between 320 mcd and the bottom of the hole (which comprises many turbidite layers), the *P*-wave velocity trend is constant around 1900 m/s and shows a much higher scatter of values than above this interval. Individual measurements revealed values >2200 m/s, which were measured on the coarser grained layers of turbidite sequences, whereas the fine-grained turbidite layers showed much lower velocities. Because of an operational error that produced inaccurate transducer displacement measurements, the velocities determined with the PWS3 sensor may be overestimated by ~100–200 m/s.

F28. *P*-wave velocity measurements, **p. 67.**

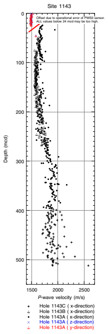

T14. Thermal conductivity measurements, **p. 101.**

Thermal Conductivity

Thermal conductivity data from the APC and XCB cores range from 0.81 to 1.19 W/(m·K) (Table **T14,** also in **ASCII format;** Fig. **F29**). The values from XCB cores are compromised by poor core quality, particularly in the upper XCB interval. The values from APC cores show a distinct increase around 150 mcd, compatible with the rise in carbonate concentration. Comparison of the APC thermal conductivity and MAD bulk density values interpolated at corresponding depths illustrates the intrinsic relationship between the two properties (Fig. **F30**).

F29. Thermal conductivity measurements, **p. 68.**

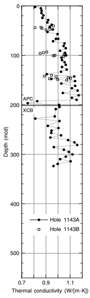

F30. Comparison of bulk density and thermal conductivity measurements, **p. 69.**

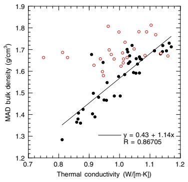

Heat Flow

Four downhole temperature measurements with the APC (Adara) temperature tool were taken in Hole 1143A at depths of 31.4, 59.9, 90.0, and 145.4 mbsf, respectively. In addition, a bottom-water temperature measurement was taken before coring in Hole 1143B (Fig. **F31**). The objective was to establish the local heat flow. Original temperature records were analyzed using the "Tfit" software to establish the equilibrium temperature at depth. The estimated errors in equilibrium temperature vary from 0.2° to 0.4°C, reflecting the amount of heat introduced by the ship's heave during the 10-min-long measurements. Depth errors are on the order of ±0.5 m. The measurements between 0 and 145.4 mbsf yielded a thermal gradient of 86°C/km (Fig. **F32**).

F31. Downhole temperature measurements, **p. 70.**

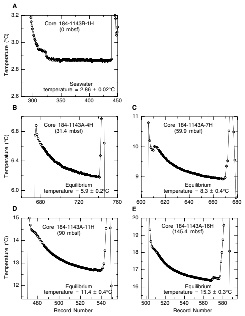

WIRELINE LOGGING

Logging Operations

After reaching the target coring depth of 400 mbsf, Hole 1143A was filled with viscous mud, reamed, and flushed of debris. We ran one full pass and a shorter repeat pass with the triple combo tool suite, including the hostile environment natural gamma-ray sonde (HNGS), accelerator porosity sonde, hostile environment lithodensity sonde (HLDS), dual-induction tool (DIT; resistivity), and Lamont-Doherty Earth Observatory temperature/acceleration/pressure tool (LDEO TAP); and one pass with the FMS, long-spaced sonic (LSS), and natural gamma-ray spectrometry tool (NGT) tool string (Fig. **F33;** also see **"Wireline Logging,"** p. 21, in the "Explanatory Notes" chapter). (The raw data are given on the **"Related Leg Data"** contents list.) The GHMT string was not run because of deteriorating hole conditions. Since the computer driving the LDEO TAP tool crashed during the first pass, the temperature data could not be off-loaded at the end of the triple combo run. Logging operations started at 0015 hr on 6 March and finished at 2315 hr on 6 March (Table **T15**). Because the sea state was stable, the triple combo was run without the wireline heave compensator (WHC). The WHC was used only for the FMS because it acquires data every 2.5 mm and thus requires greater stability of the tool string.

Clay swelling was observed on the logs during the triple combo run (the hole was as small as 10 cm in places). Subsequently, a pipe trip was made before the next descent. The first run with the FMS-dipole sonic imager (DSI)–NGT tool string started off with a failure of the DSI, which had to be replaced by the LSS. Running this new tool string, we encountered an obstruction <20 m below the end of the pipe. After several attempts to pass it, we used the pumps to try to push it through, since the top of the tool was still in the sealbore. This gained us only about 3 m; upon coming up, a moderate overpull was necessary to free the tool. After coming out and laying aside the tools and wireline, the pipe was short tripped to a depth of 163 mbsf and then pulled back and set at 134 mbsf. After the tool string reached open hole, well over an hour was required for it to work through the clays. Finally, however, it reached a depth of 378 mbsf. The hole was then logged up to pipe with no repeat section.

F32. Downhole temperature gradient, **p. 71.**

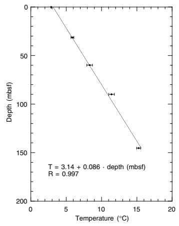

F33. Graphic summary of downhole logging operations for Hole 1143A, **p. 72.**

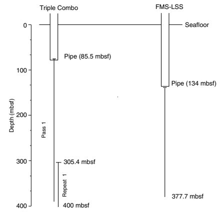

T15. Summary of logging operations at Site 1143, **p. 103.**

Log Quality

Because the hole fills with debris falling from the borehole wall over time, logging-tool runs vary in the maximum depth that they reach. The triple combo, which was the first tool-string run, reached the bottom of the hole, whereas the FMS-LSS reached within 23 m of the bottom. The two triple combo runs showed excellent repeatability for all the log parameters.

The hole was generally in good shape below 200 mbsf. Borehole caliper measurements showed that the lower part of the hole was typically 25 cm in diameter, yielding good data. The upper part of the hole, however, showed zones of washout reaching 45 cm in diameter (Fig. **F34**), alternating with narrow ledges caused by swollen clays. The washed-out zones resulted in poor contact with the borehole wall and hence negative spikes in the density log and positive spikes in the porosity log. Although some of the sections with excessive hole diameter were probably caused by the drill bit rotating at the same depth for a length of time (e.g., between taking cores), there is also a lithologic control. The deeper penetrating logs, such as medium resistivity, are much less affected by changing borehole diameter: whereas the upper part of the resistivity values from the spherically focused log (SFL) is characterized by many spikes, the medium and deep resistivity values from the DIT are undisturbed (Fig. **F34**). Despite this, the three resistivity curves show excellent agreement throughout the entire logged interval.

F34. Downhole logs and interpretation of FMS images from Hole 1143A, **p. 73.**

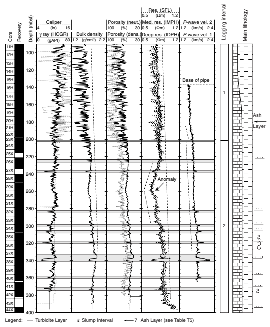

The LSS log is of good quality from total depth (366 m) up to ~158 mbsf; the two *P*-wave velocity measurements are almost completely superimposed (Fig. **F34**). Above this depth, the recorded velocity seems too slow, probably indicating fluid velocity. The FMS measurements were also of good quality, with one apparent dead button on the right side of pad 3. The WHC was charged with nitrogen and run. Stick and slip on the log was on the order of .25 m, which is typical even when the WHC is functioning at its best. The effect on the data was corrected during the processing of the FMS images with the Geoframe software.

Again, above 200 mbsf, image quality is poor because of rugosity of the hole.

In general, standard gamma ray (HSGR) and computed gamma ray (HCGR) from the HNGS tool in the triple combo run read 10% to 25% higher than spectroscopy gamma ray (SGR) or computed gamma ray (CGR) from the NGT tool in the FMS-LSS run, a difference easily accounted for by eccentering and hole-size correction. Contrary to the NGT, the HNGS corrects for borehole diameter and potassium in the borehole fluid. The HNGS is the more sensitive of the two; hence, its results are presented in Figures **F34** (column 1) and **F35.**

Results

We observed a general trend of increasing *P*-wave velocities below 250 mbsf in both the split-core samples and logs (Fig. **F36;** also see **"Physical Properties,"** p. 23). Some velocity peaks of the log curve are not seen in the core data. These discrepancies might have resulted from the lower sampling rate on the split cores.

The absolute values of gamma-ray attenuation bulk density data from cores and the downhole log generally agree, apart from the anomalous log density lows at washouts in the upper part (Fig. **F36**). At ~190 mbsf, core data from MST measurements show an offset not visible in the log data and are somewhat lower (0.1 g/cm^3) than the logging densities in the lower part of the hole. This suggests that the offset seen in core-derived data is a result of changing coring from APC to XCB.

Natural gamma-ray data from core and downhole logging show similar general trends on a first-order approximation (Fig. **F37**) but are offset in value. As for the density values, reduced core diameter and lower average density as a result of remolding during XCB coring caused lower gamma radiation values from the cores below 190 mbsf (see **"Physical Properties,"** p. 23).

Downhole neutron porosity and porosity calculated from the moisture content of core samples also show similar general trends apart from the intervals with large hole diameter (Fig. **F37**). A major turbidite (around 338 mbsf) is visible on both downhole and core data but with an offset of ~5 m (Figs. **F34, F37, F38**).

The sedimentary sequence could be divided into two intervals based on changes in the character of some downhole logs (Figs. **F34, F35, F38**).

Interval 1 (Base of Pipe at 85.5 mbsf to a Depth of 200 mbsf)

This interval is characterized by bad hole conditions. Spikes resulting from the washouts can be seen on the logs, especially on HCGR, bulk density, porosity, and SFL resistivity logs (Fig. **F34**).

In interval 1, the photoelectric effect (PEF) log has an average value of 2.6 barn/e$^-$. This interval generally shows high gamma-ray and porosity values as well as low density values (Figs. **F34, F38**). These conditions are compatible with a nannofossil clay (see **"Lithostratigraphy,"** p. 8).

Within interval 1, we can define two different features based on *P*-wave velocity and PEF logs (Figs. **F34, F38**). The first extends to 190 mbsf, nearly where the dark ash layer in Core 184-1143A-20H affects the logs. This feature shows a slight downhole increase in the base level of density and resistivity variations, whereas gamma ray and porosity

F35. Downhole logs from the HNGS tool on the triple combo tool suite, **p. 75.**

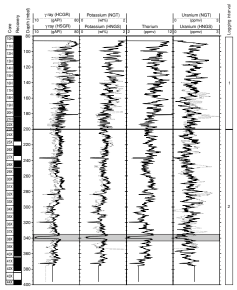

F36. Comparison of *P*-wave velocities with physical properties measurements, **p. 76.**

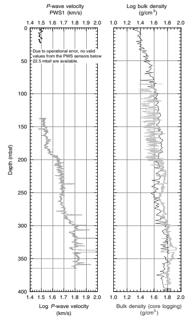

F37. Comparison of spectral gamma ray with MST natural gamma-ray data, **p. 77.**

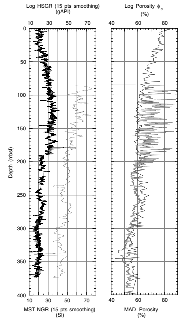

F38. Comparison of the HCGR, IMPH, and PEF logs with carbonate content, **p. 78.**

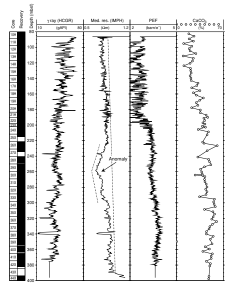

behave in the opposite way. The second feature is marked by a downhole step increase in *P*-wave velocity and in PEF values (Figs. **F34, F38**). This increase is related to the second increase of carbonate content measured on the core at ~190 mbsf (Figs. **F34, F38;** see **"Organic Geochemistry,"** p. 18).

Interval 2 (200 mbsf to Bottom of Hole at 400 mbsf)

The transition from interval 1 to interval 2 is marked by smaller increasing trends in density, smaller decreasing trends in natural gamma and porosity, and a jump in the PEF curve. In interval 2, PEF log values lie mostly between 2.5 and 3.4 barn/e^- (Fig. **F38**), closer to the carbonate PEF value. Generally lower gamma ray and porosity together with higher density and resistivity also indicate higher carbonate and less clay content. This interval contains a major anomaly from 220 to 300 mbsf, where a change in the increasing trend of resistivity can be seen; at 220 mbsf, we noticed a steady downhole decrease in resistivity to ~0.7 Ωm. *P*-wave velocity keeps increasing steadily, whereas porosity keeps decreasing gently. Resistivity and gamma ray show a slight increase in variability (Fig. **F34**). Near 320 mbsf, we distinguished small cycles between low gamma ray–high resistivity layers and high gamma ray–low resistivity layers that are easily seen in the FMS images (Fig. **F39**). This alternation between dark and light layers suggests cycles with more or less clay, respectively. The FMS images also show the particular slump seen in Core 184-1143A-36X (Fig. **F39**).

All the major turbidite layers described in the cores are clearly distinguishable both in logging data and FMS images (Fig. **F34**). The base of the turbidites (sandy part) is characterized by lower gamma-ray, density, and resistivity and higher porosity and *P*-wave velocity values; the opposite is true for the top (clayey part). The major turbidite layer (Cores 184-1143A-37X and 38X) seen in the FMS images is presented in Figure **F40**. Although usually darker intervals in FMS images are conductive (clay layer) and lighter ones are resistive (sand layer), turbidites look darker at the base and lighter at the top. Here, the resistivity is much lower than the clayey part because the sandy base has higher grain size, reflecting less matrix and more fluid. This is why the color scale is reversed for a turbidite. By looking at both the standard logs and FMS images, we are able to count the number of turbidite layers present in the lower part of Hole 1143A.

F39. FMS image displaying alternation of darker and lighter intervals, **p. 79.**

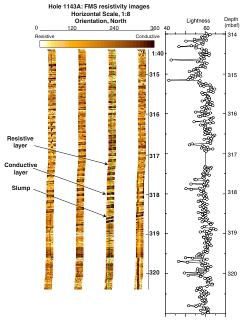

F40. FMS image displaying the major turbidite in Cores 184-1143A-37X and 38X, **p. 80.**

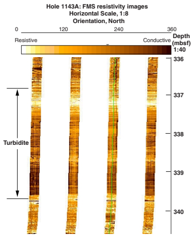

REFERENCES

Berggren, W.A., Kent, D.V., Swisher, C.C., III, and Aubry, M.-P., 1995. A revised Cenozoic geochronology and chronostratigraphy. *In* Berggren, W.A., Kent, D.V., Aubry, M.-P., and Hardenbol, J. (Eds.), *Geochronology, Time Scales and Global Stratigraphic Correlation.* Spec. Publ.—Soc. Econ. Paleontol. Mineral. (Soc. Sediment. Geol.), 54:129–212.

Blow, W.H., 1969. Late middle Eocene to Recent planktonic foraminiferal biostratigraphy. *In* Brönnimann, P., and Renz, H.H. (Eds.), *Proc. First Int. Conf. Planktonic Microfossils, Geneva, 1967:* Leiden (E.J. Brill), 1:199–422.

Bouma, A.H., 1962. *Sedimentology of Some Flysch Deposits: A Graphic Approach to Facies Interpretation:* Amsterdam (Elsevier).

Emerson, S., Jahnke, R., Bender, M., Froelich, P., Klinkhammer, G., Bowser, B., and Setlock, G., 1980. Early diagenesis in sediments from the Eastern Equatorial Pacific. I. Pore water nutrients and carbonate results. *Earth Planet. Sci. Lett.,* 49:57–80.

Feary, D.A., Hine, A.C., Malone, M.J., et al., 2000. *Proc. ODP, Init. Repts.,* 182 [CD-ROM]. Available from: Ocean Drilling Program, Texas A&M University, College Station, TX 77845-9547, U.S.A.

Fuller, M., Hastedt, M., and Herr, B., 1998. Coring-induced magnetization of recovered sediment. *In* Weaver, P.P.E., Schmincke, H.-U., Firth, J.V., and Duffield, W. (Eds.), *Proc. ODP, Sci. Results,* 157: College Station, TX (Ocean Drilling Program), 47–56.

Gardner, J.V., Nelson, C.S., and Baker, P.A., 1986. Distribution and character of pale green laminae in sediment from Lord Howe Rise: a probable late Neogene and Quaternary tephrostratigraphic record. *In* Kennett, J.P., von der Borch, C.C., et al., *Init. Repts. DSDP,* 90 (Pt. 2): Washington (U.S. Govt. Printing Office), 1145–1159.

Gartner, S., 1967. Calcareous nannofossils from Neogene of Trinidad, Jamaica, and Gulf of Mexico. *Univ. Kansas Paleontol. Contrib.,* 29:1–7.

Huang, W., and Wang, P., 1998. A quantitative approach to deep-water sedimentation in the South China Sea. *Sci. China, Beijing,* Ser. D, 41:195–201.

Li, B., 1997. Paleoceanography of the Nansha Area, southern South China Sea since the last 700,000 years [Ph.D. dissert.]. Nanjing Inst. Geol. Paleontol., Academica Sinica, Nanjing, China. (in Chinese, with English abstract)

Lind, I.L., Janecek, T.R., Krissek, L.A., Prentice, M.L., and Stax, R., 1993. Color bands in Ontong Java Plateau carbonate oozes and chalks. *In* Berger, W.H., Kroenke, L.W., Mayer, L.A., et al., *Proc. ODP, Sci. Results,* 130: College Station, TX (Ocean Drilling Program), 453–470.

Müller, P.J., 1977. C/N ratios in Pacific deep sea sediments: effect of inorganic ammonium and organic nitrogen compounds sorbed by clays. *Geochim. Cosmochim. Acta,* 41:765–776.

Sarnthein, M., Pflaumann, U., Wang, P.X., and Wong, H.K. (Eds.), 1994. Preliminary Report on Sonne-95 Cruise "Monitor Monsoon" to the South China Sea. *Rep. Geol.-Paläontol. Inst. Univ. Kiel.,* 68.

Schönfeld, J., 1996. The "*Stilostomella* Extinction": structure and dynamics of the last turnover in deep-sea benthic foraminiferal assemblages. *In* Mogurlevsky, A., and Whatly, R. (Eds.), *Microfossils and Oceanic Environments:* Aberystwyth (Univ. Wales, Aberystwyth Press), 27–37.

Stokking, L.B., Musgrave R.J., Bontempo, D., and Autio, W., 1993. Handbook for Shipboard Paleomagnetists. *ODP Tech. Note,* 18: College Station, TX (Ocean Drilling Program).

Thompson, P.R., Bé, A.W.H., Duplessy, J.-C., and Shackleton, N.J., 1979. Disappearance of pink-pigmented *Globigerinoides ruber* at 120,000 yr BP in the Indian and Pacific oceans. *Nature,* 280:554–558.

Tissot, B.P., and Welte, D.H., 1984. *Petroleum Formation and Occurrence* (2nd ed.): Heidelberg (Springer-Verlag).

Wang, P., Xia, L., Wang, L., and Cheng, X., 1991. Lower boundary of the marine Pleistocene in northern shelf of the South China Sea. *Acta Geol. Sinica,* 2:176–187.

Figure F1. Smoothed (11-point running average)/correlated MS data and the splice for the three holes at Site 1143 (spliced MS data for this figure are also available in **ASCII format**). The order of the four arrays (the splice and Holes 1143A through 1143C) increases outward from the origin. The hole arrays are offset from each other—and from the splice—by a constant (10.0 × 10^{-5} SI units) so that only the splice is plotted relative to the MS value. Data from the top and bottom 7 cm of the first and last section of each core have been culled. Lines identify the splice tie points. (Continued on next two pages.)

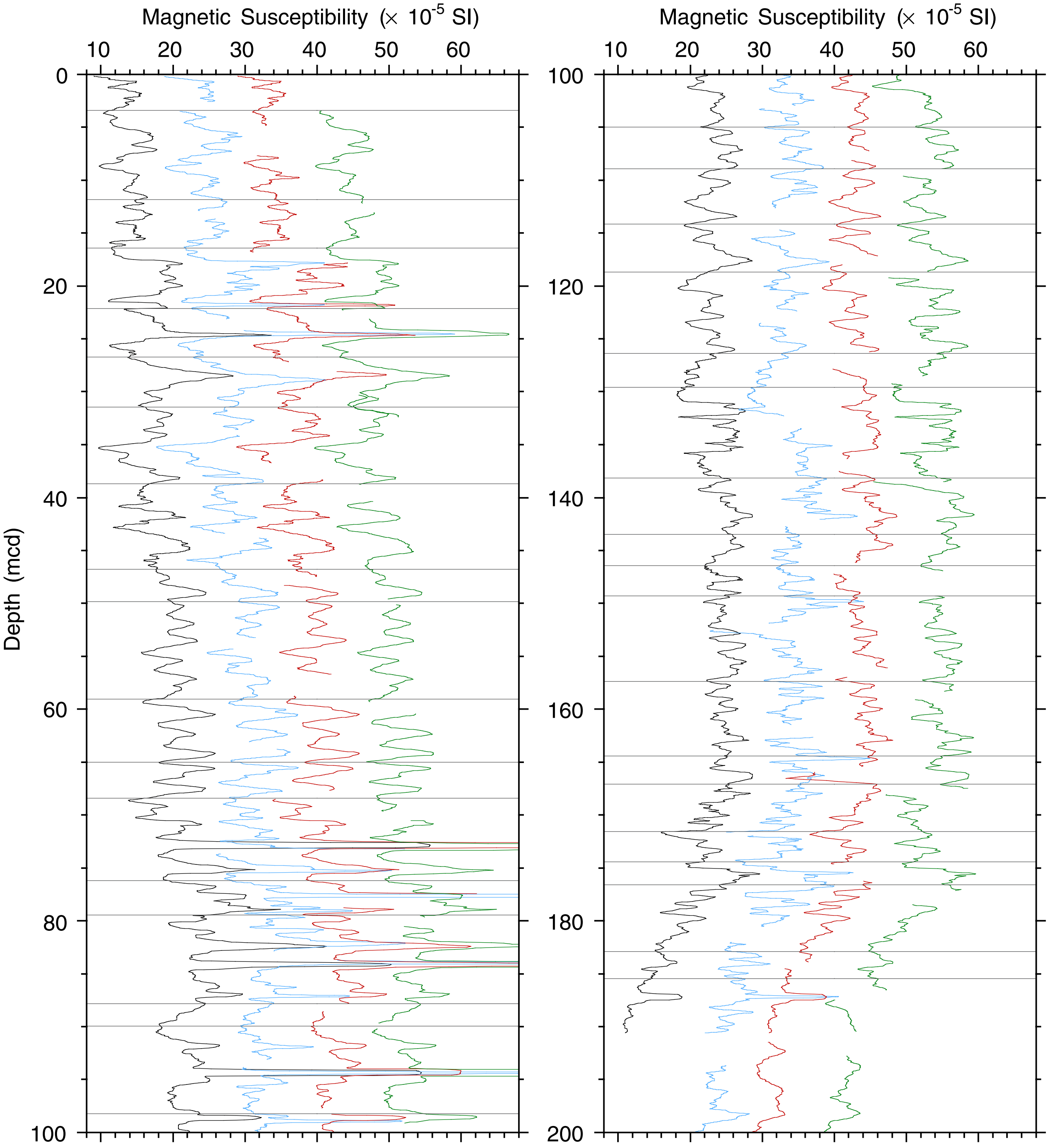

Figure F1 (continued).

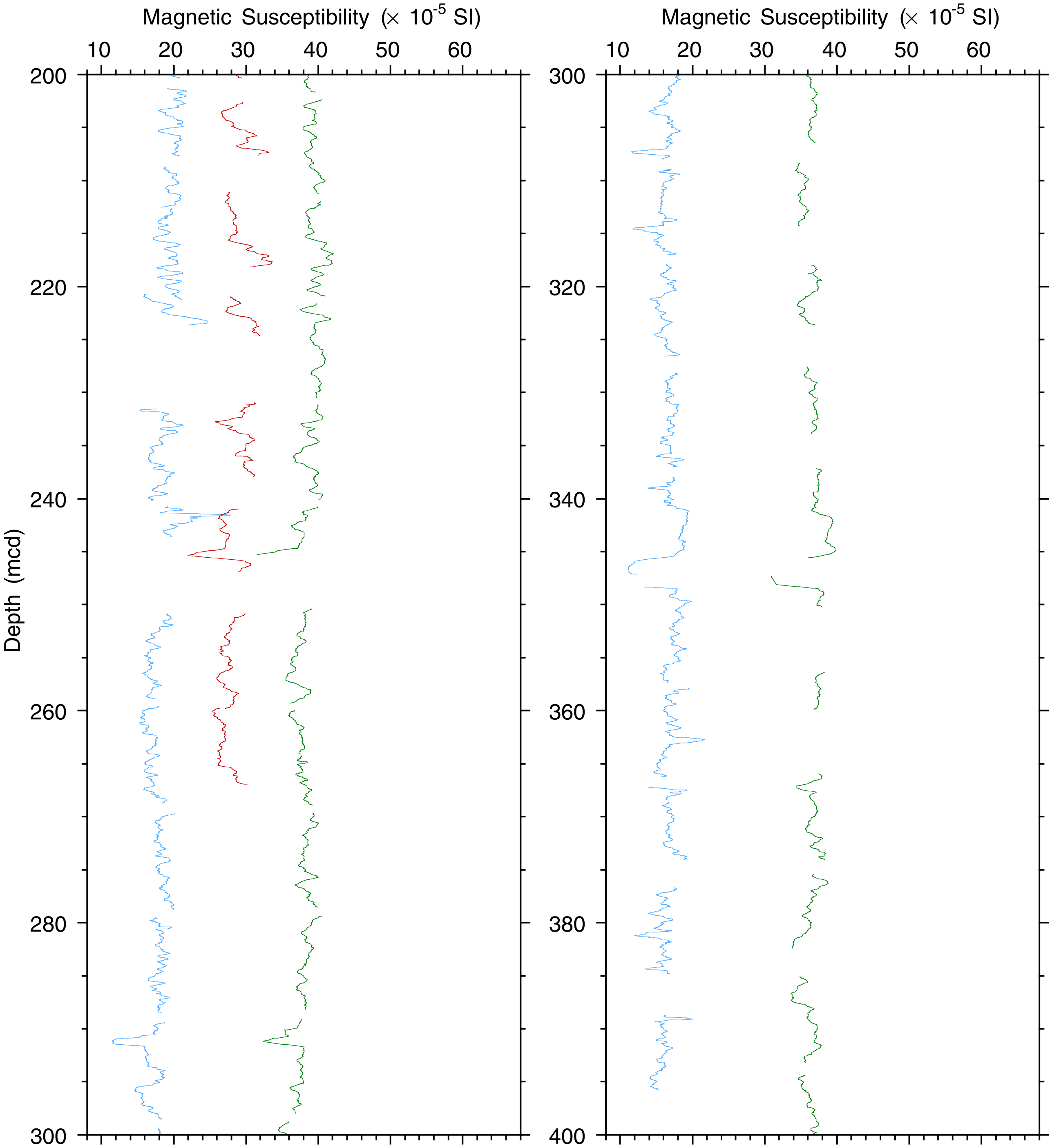

Figure F1 (continued).

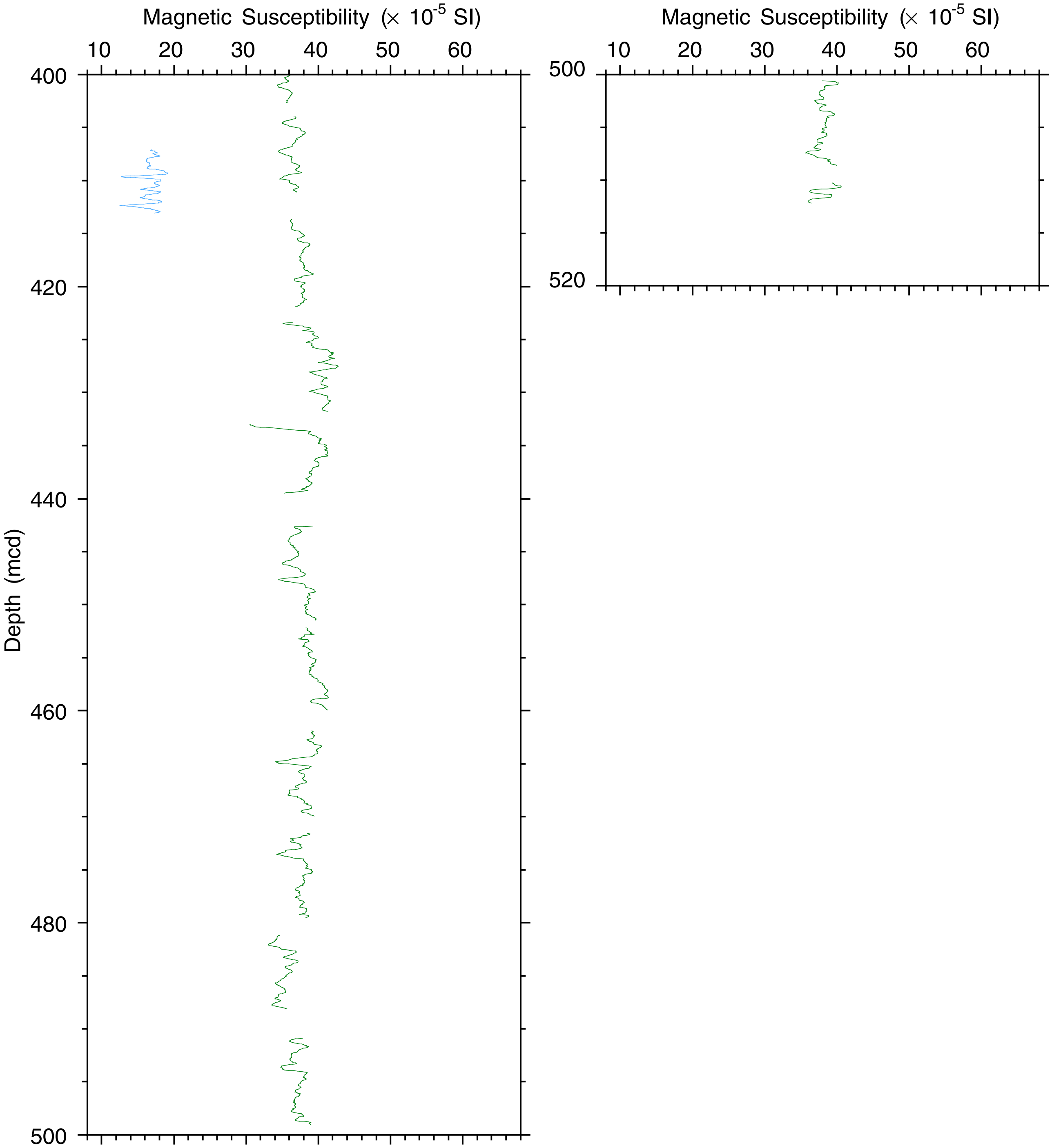

Figure F2. Smoothed (11-point running average)/correlated NGR data and the splice for the three holes at Site 1143 (spliced NGR data for this figure are also available in **ASCII format**). The order of the four arrays (the splice and Holes 1143A through 1143C) increases outward from the origin. The hole arrays are offset from each other—and from the splice—by a constant (9 cps) so that only the splice is plotted relative to the absolute NGR value. Data from the top and bottom 7 cm of the first and last section of each core, as well as values ≤0 (cps), have been culled. Lines identify the splice tie points. (Continued on next two pages.)

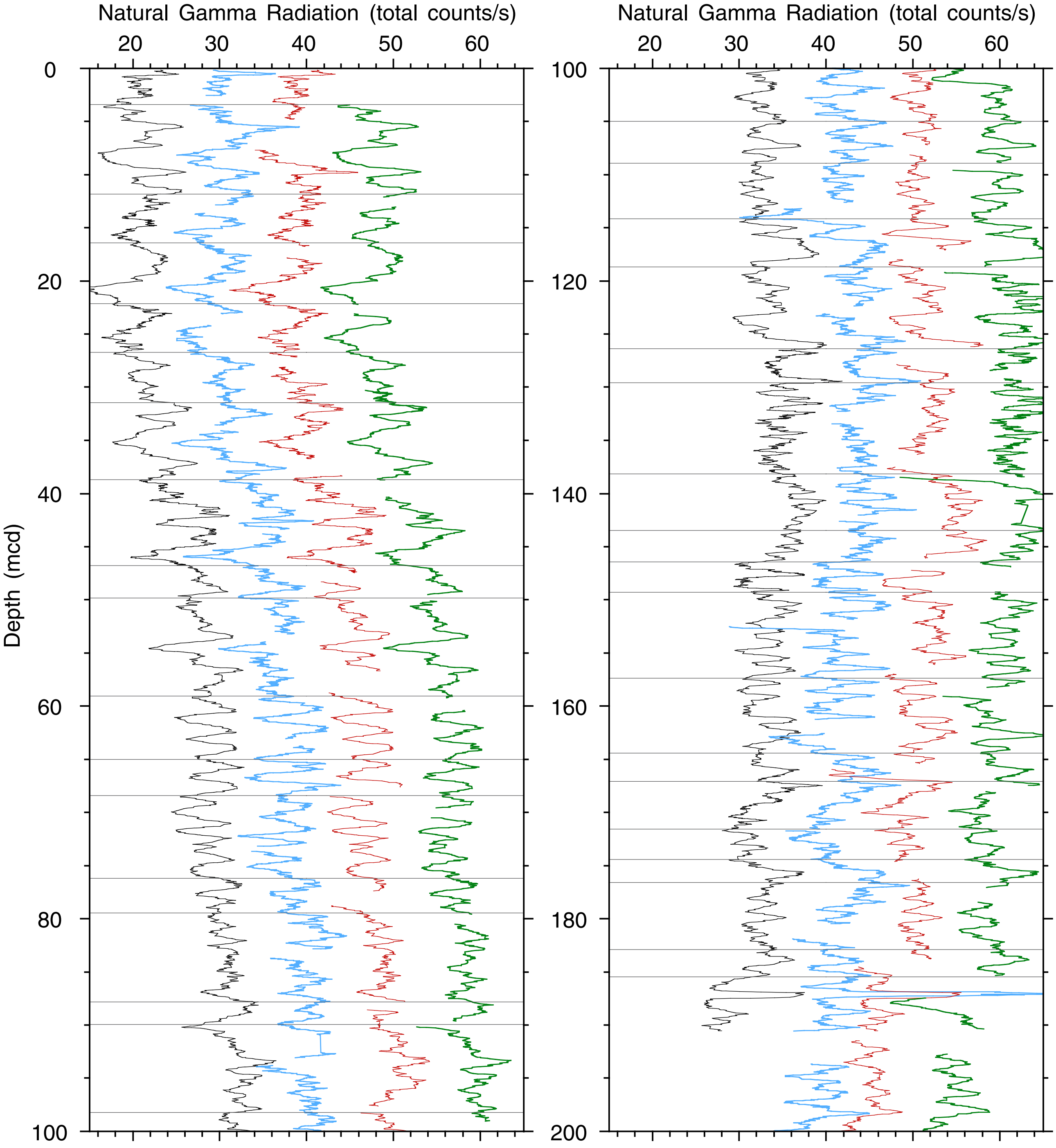

Figure F2 (continued).

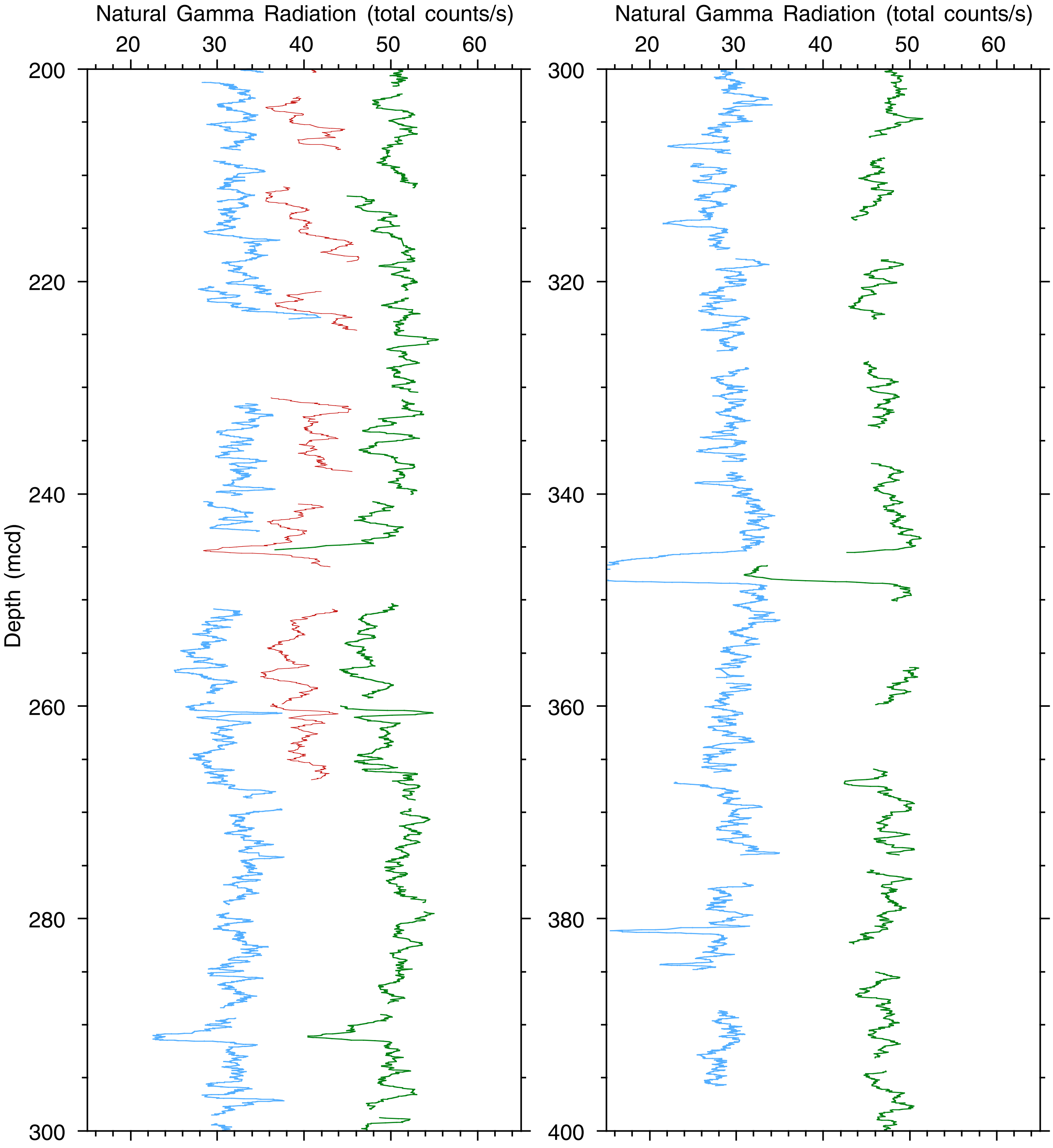

Figure F2 (continued).

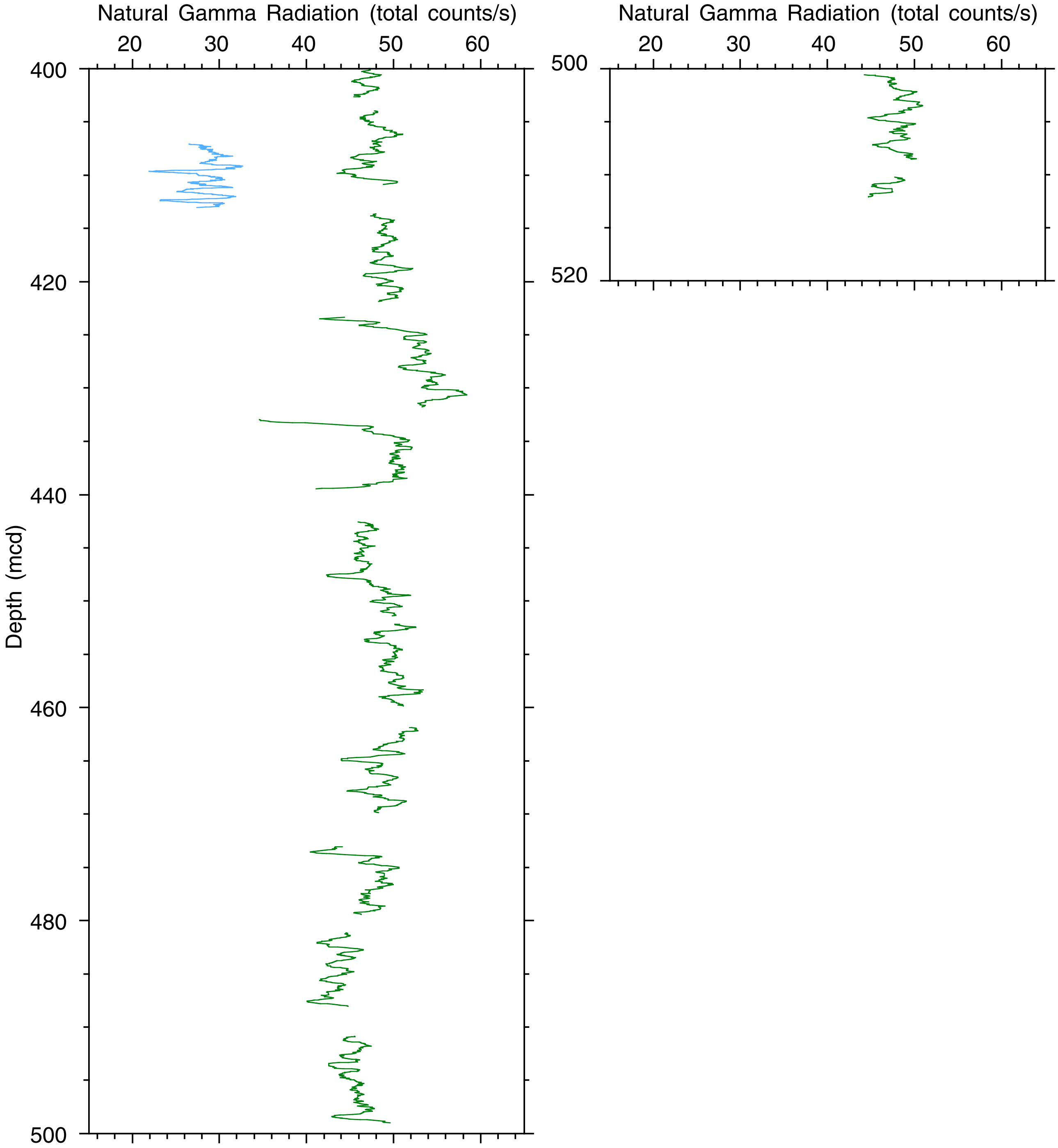

Figure F3. Smoothed (11-point running average)/correlated GRA (gamma-ray attenuation) data and the splice for the three holes at Site 1143 (spliced GRA data for this figure are also available in ASCII format). The order of the four arrays (the splice and Holes 1143A through 1143C) increases outward from the origin. The hole arrays are offset from each other—and from the splice—by a constant (0.15 g/cm³) so that only the splice is plotted relative to the absolute GRA value. Values ≤1.03 and ≥2.4 (g/cm³) have been culled. Lines identify the splice tie points. (Continued on next two pages.)

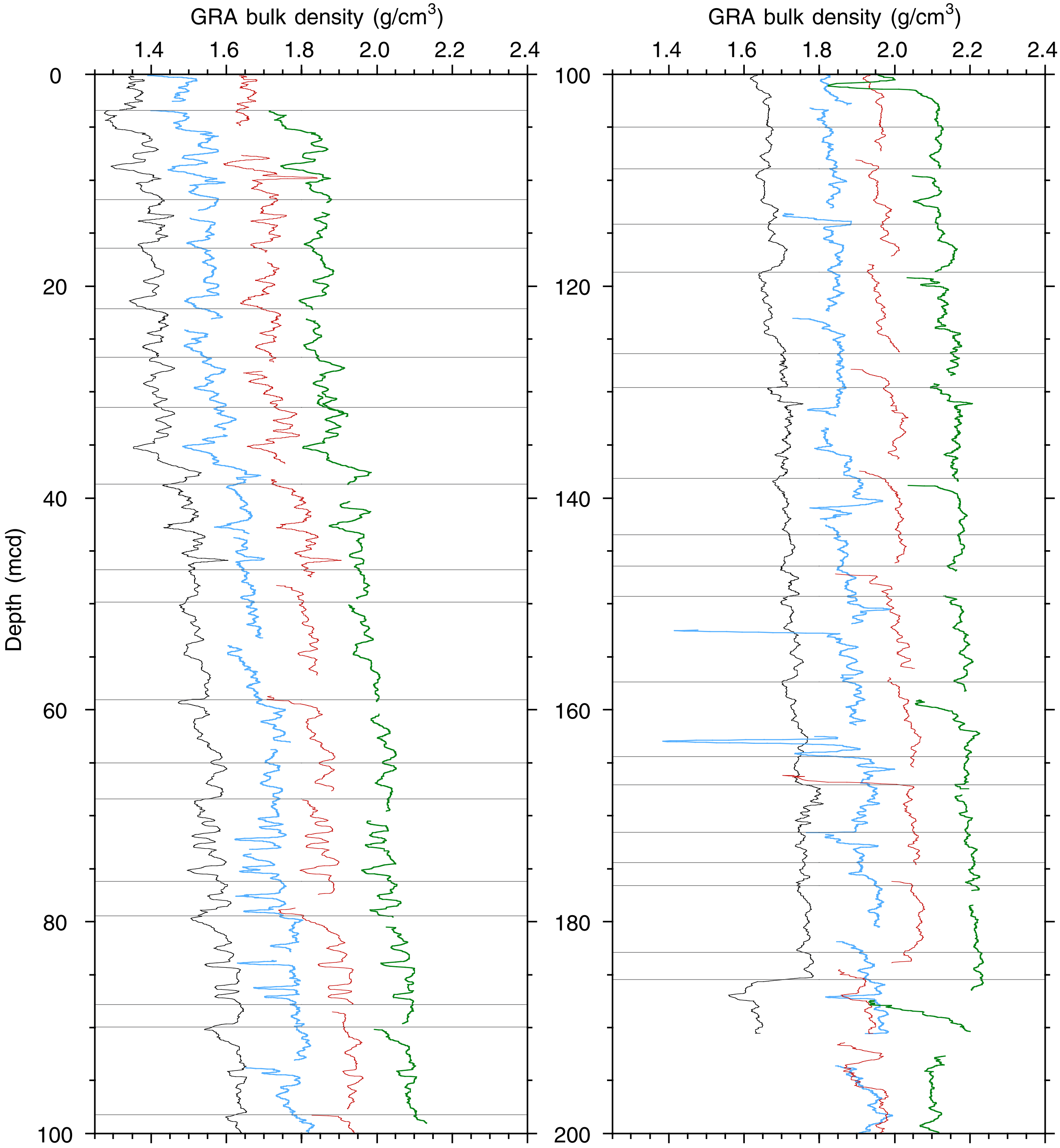

Figure F3 (continued).

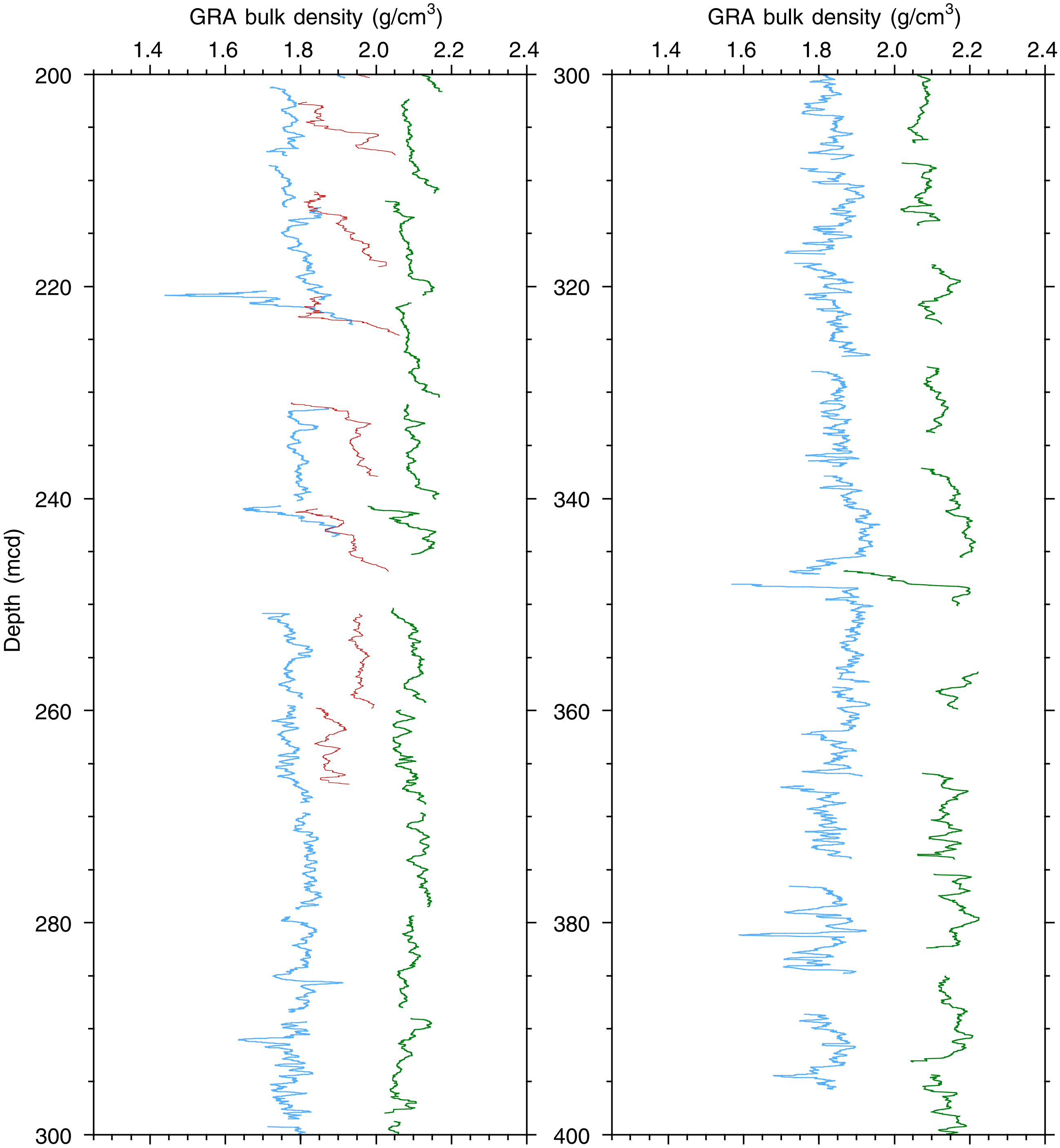

Figure F3 (continued).

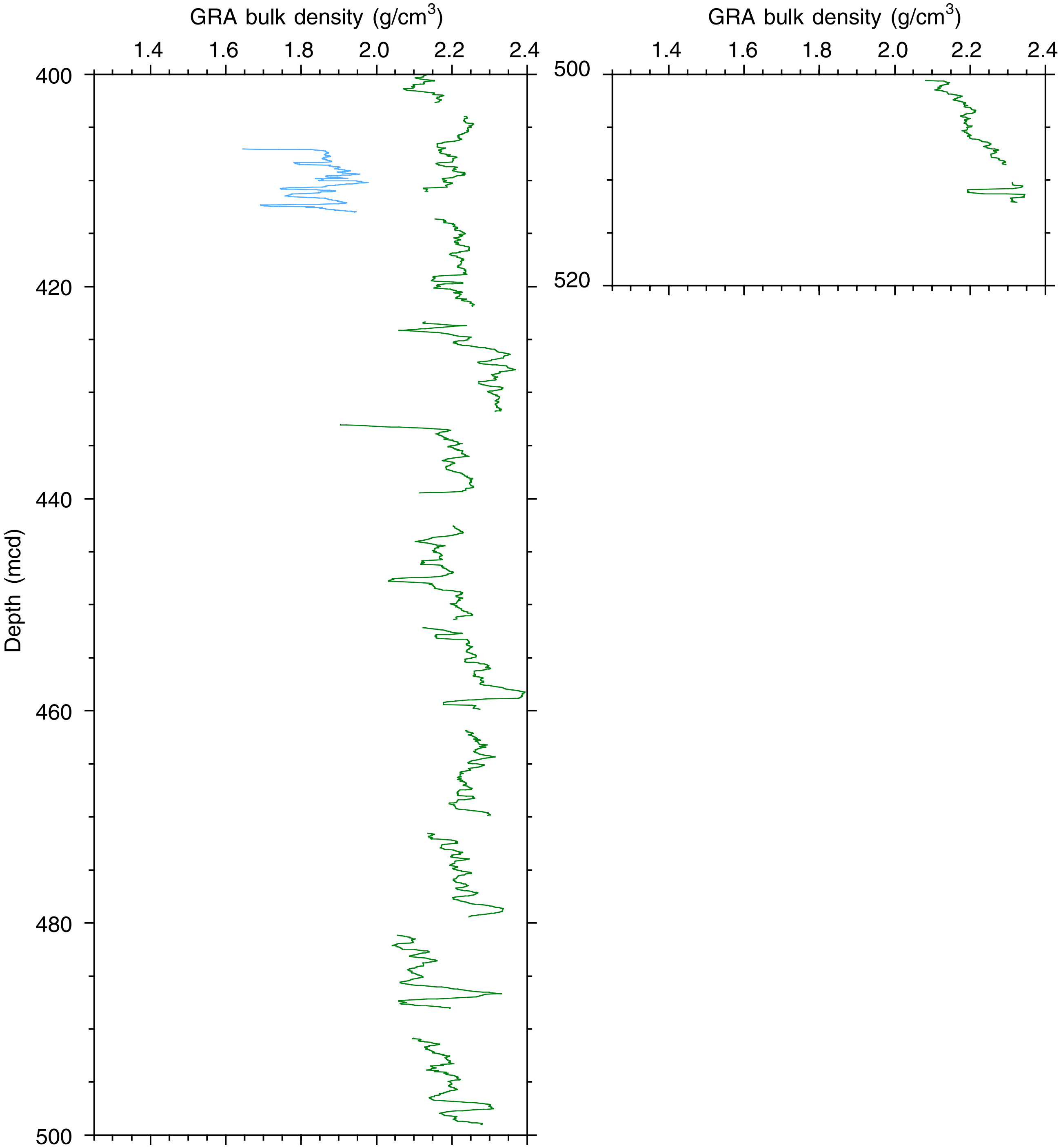

Figure F4. Smoothed (11-point running average)/correlated L* ("lightness") values from the CSR data and the splice for the three holes at Site 1143 (spliced CSR data for this figure are also available in ASCII format). The order of the four arrays (the splice and Holes 1143A through 1143C) increases outward from the origin. The hole arrays are offset from each other—and from the splice—by a constant (8%) so that only the splice is plotted relative to the absolute L* value. Values ≤1% have been culled. Lines identify the splice tie points. (Continued on next two pages.)

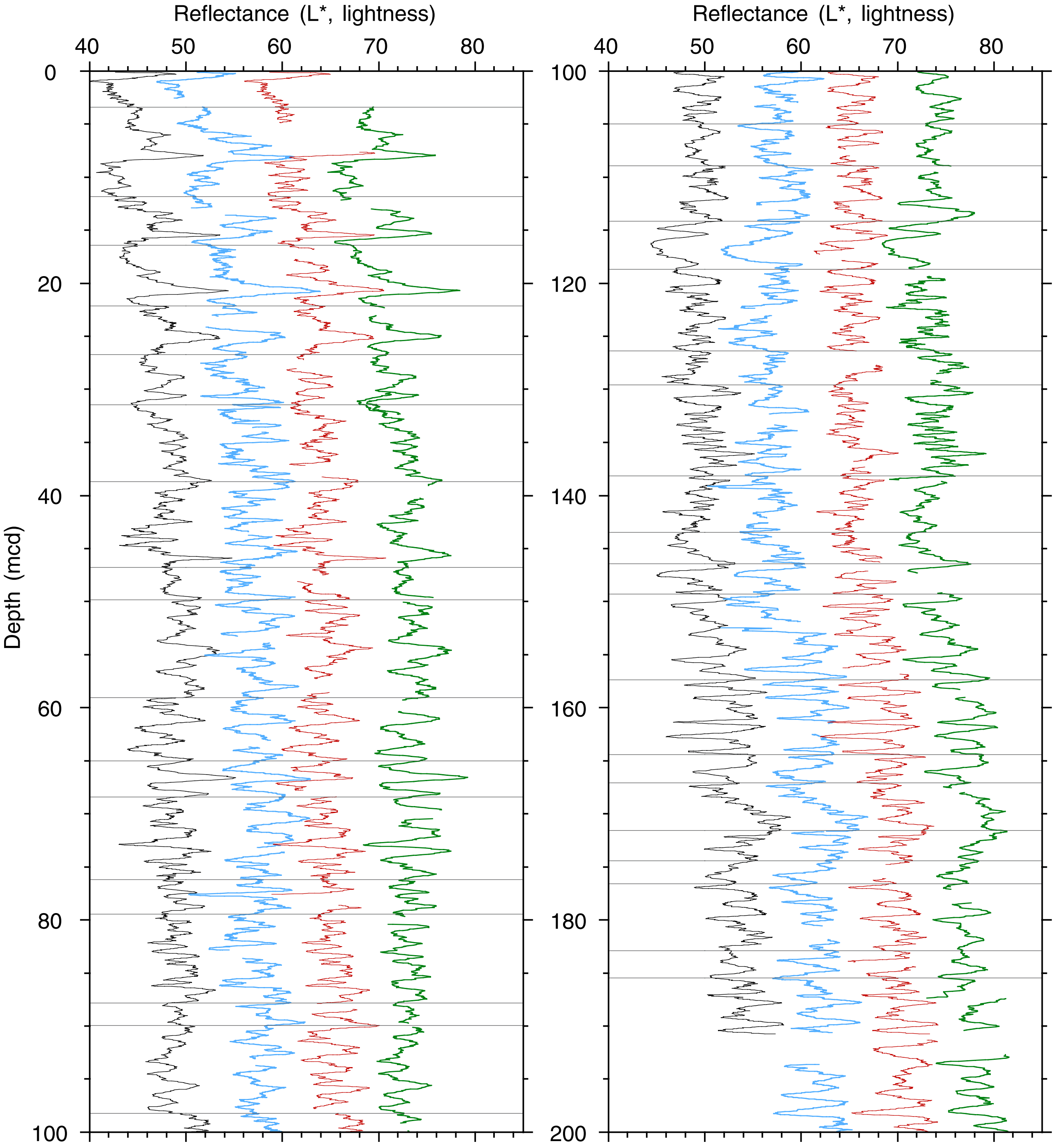

Figure F4 (continued).

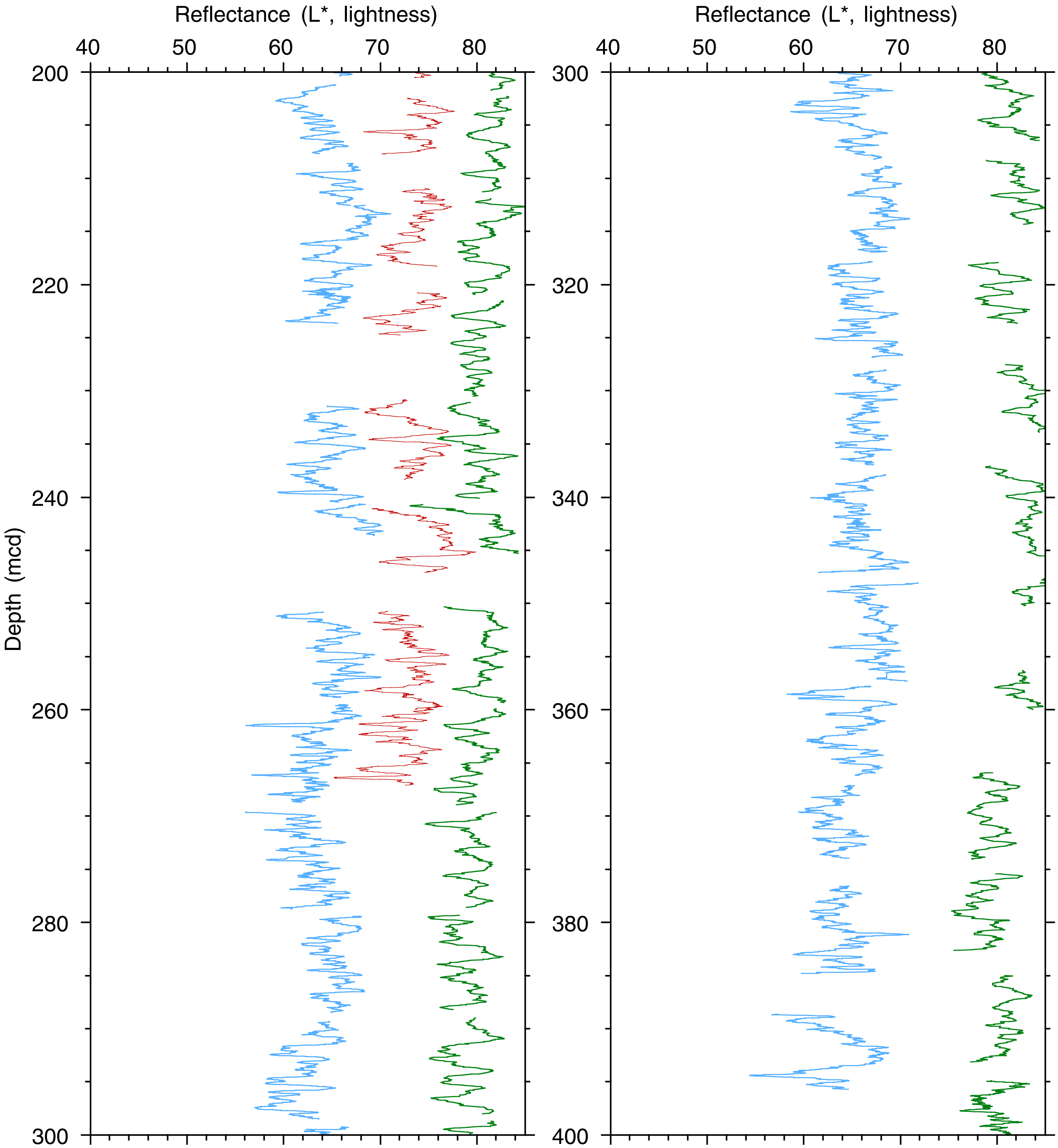

Figure F4 (continued).

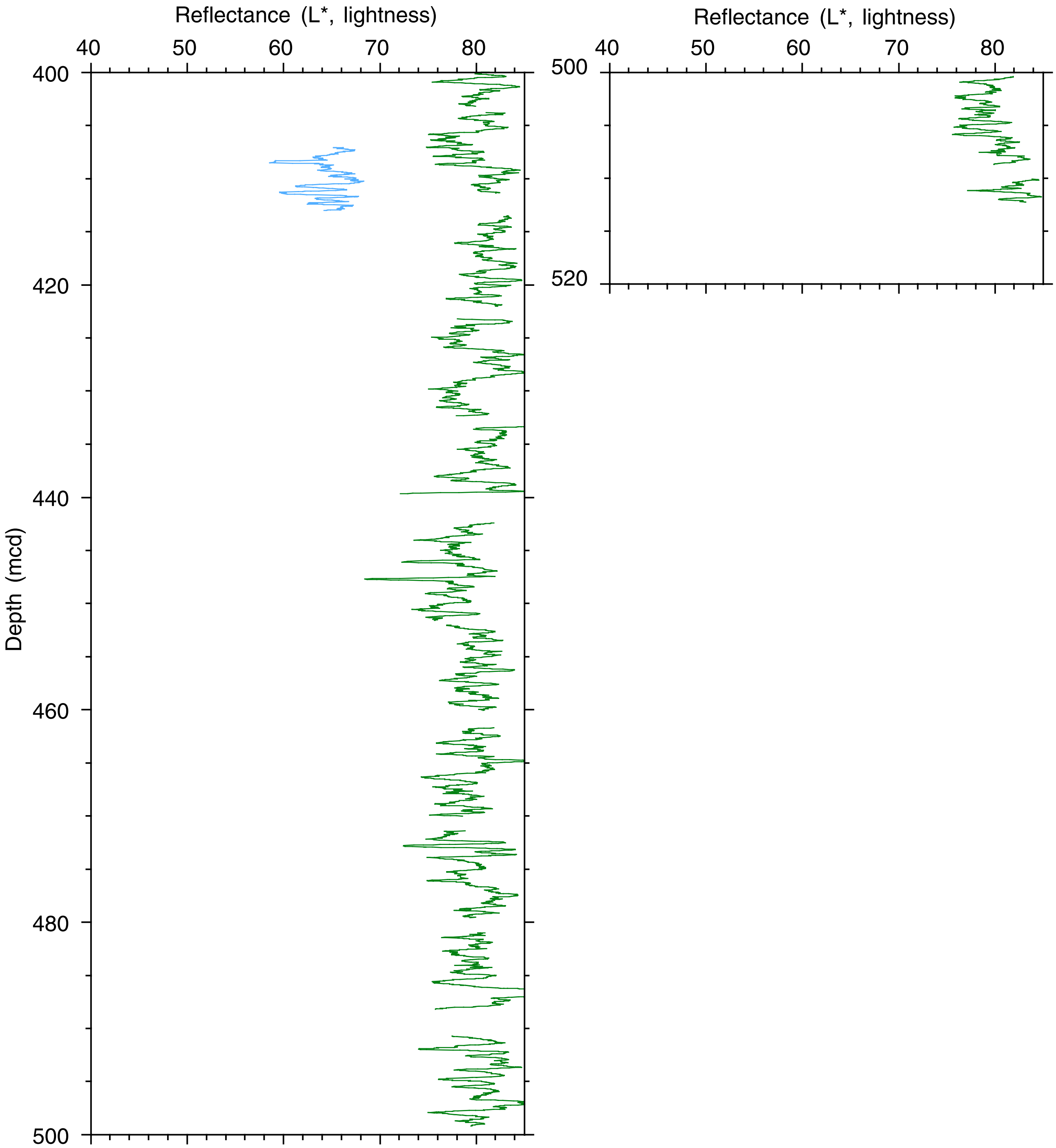

Figure F5. Summary of the sediments at Site 1143. T.D. = total depth.

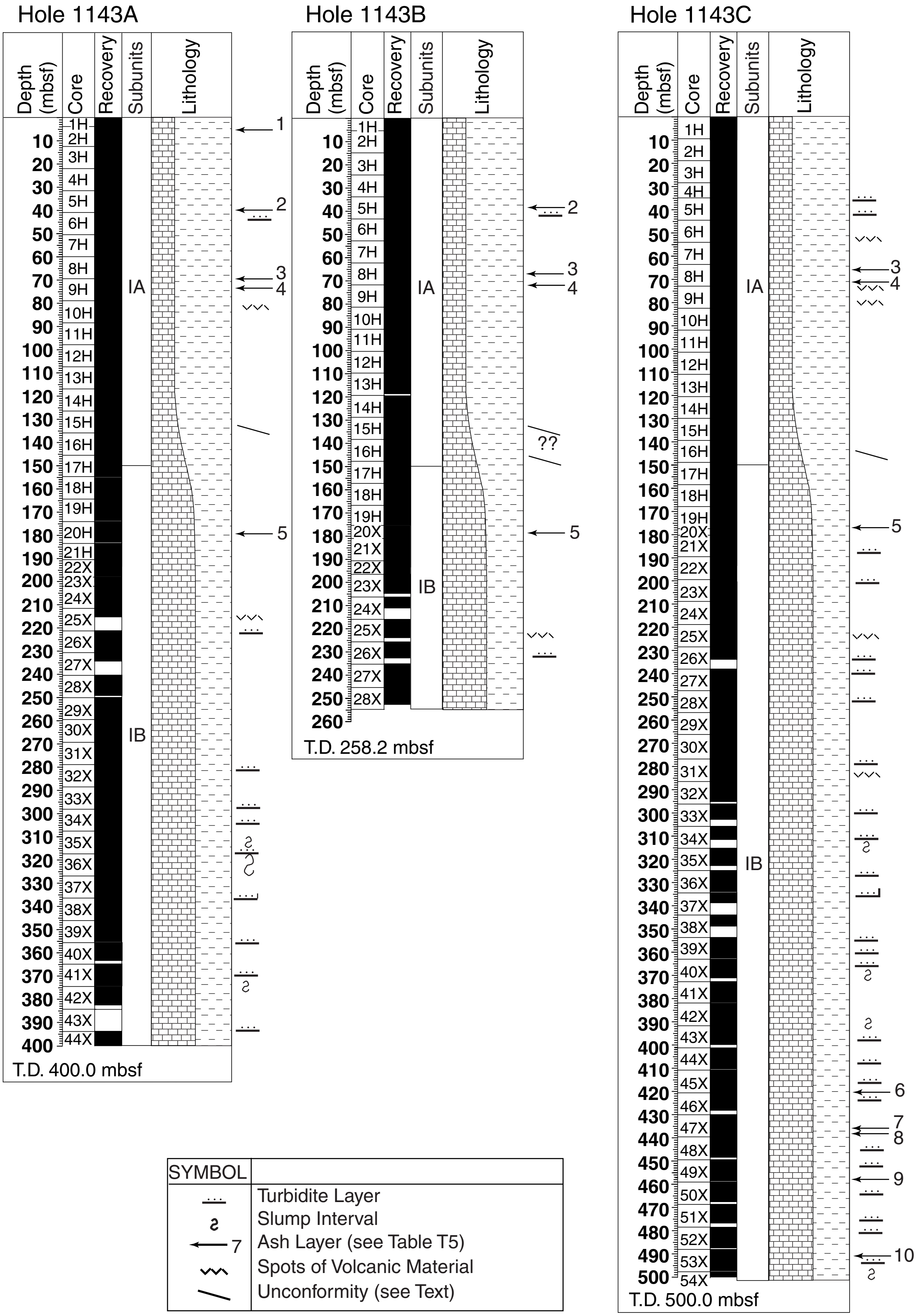

Figure F6. Frequency of green clay layers per core. T.D. = total depth.

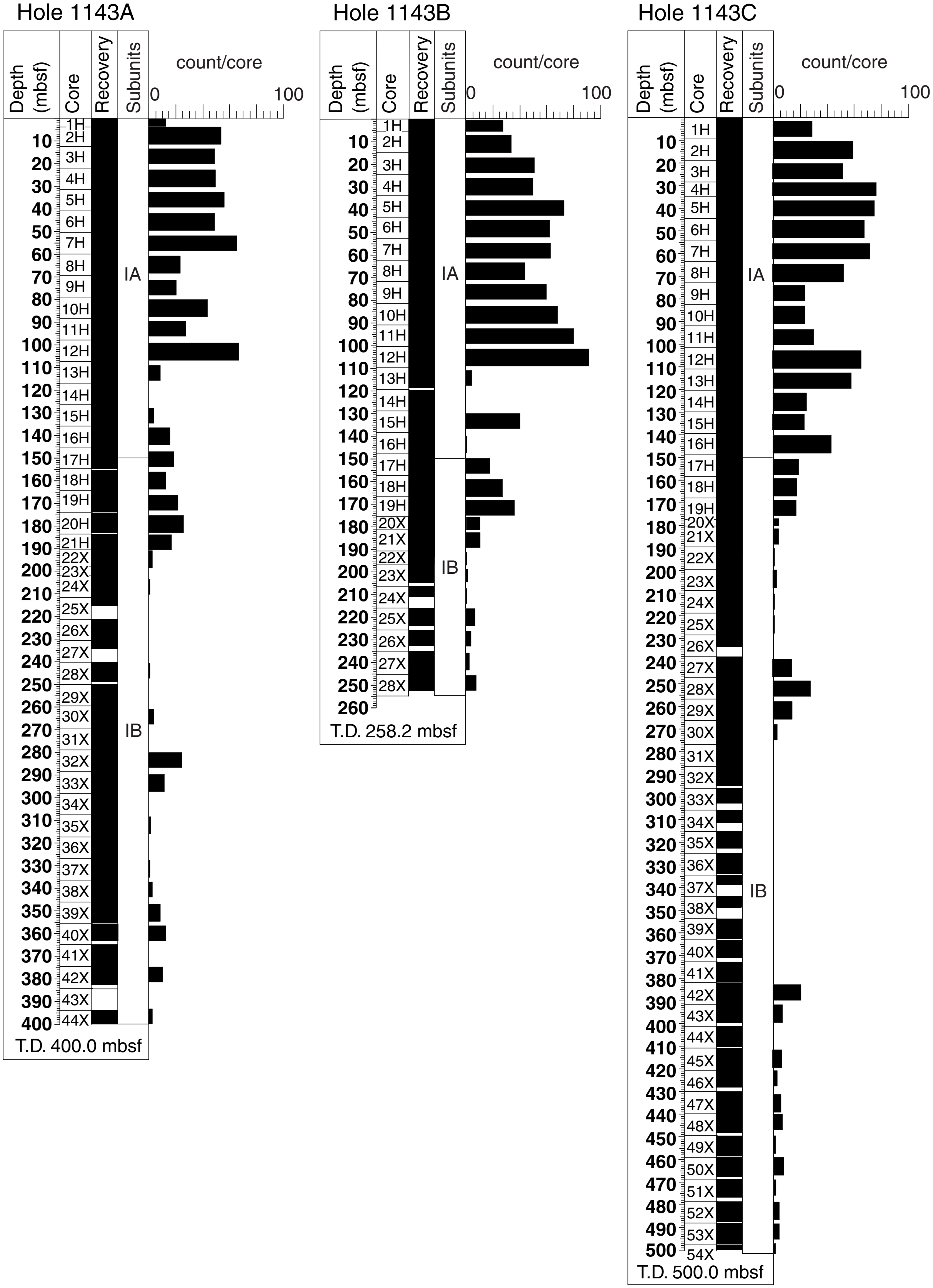

Figure F7. Green clay layer (interval 184-1143C-5H-3, 20–23 cm [38.10–38.13 mbsf; 39.76–39.79 mcd]).

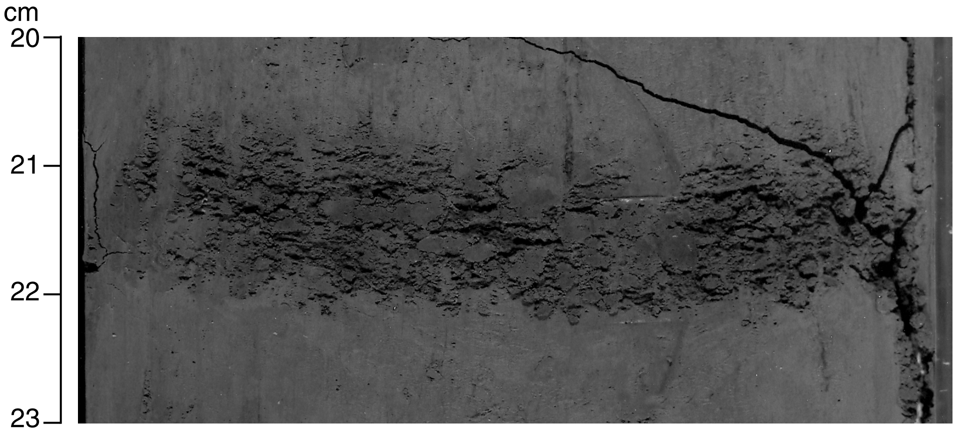

Figure F8. Inclined unconformity with black layer (interval 184-1143A-15H-5, 93–109 cm [133.33–133.49 mbsf; 140.21–140.37 mcd]).

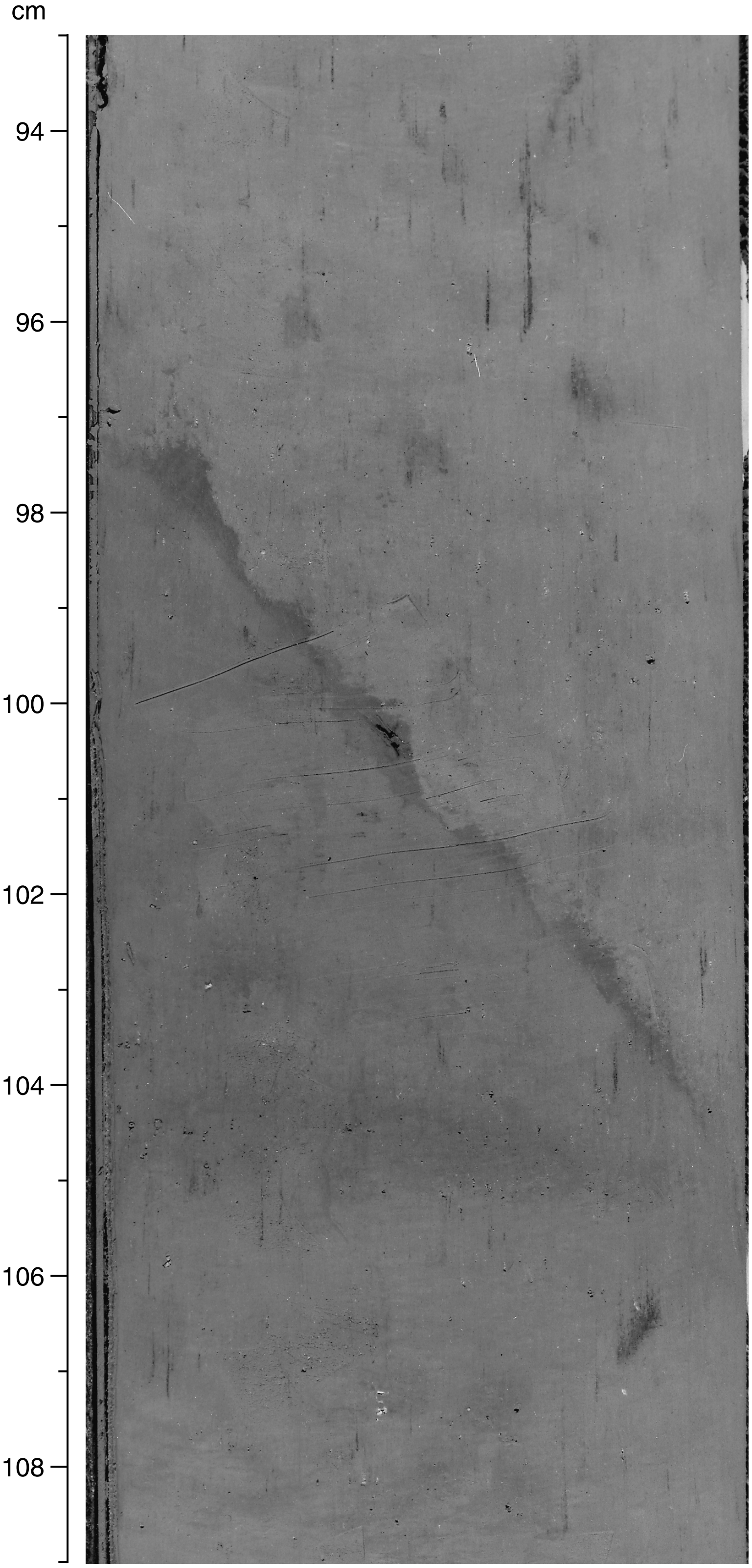

Figure F9. Black ash layer. Note bioturbation of the ash into the overlying sediments (interval 184-1143B-20X-2, 120–142 cm [178.10–178.32 mbsf; 186.97–187.19 mcd]).

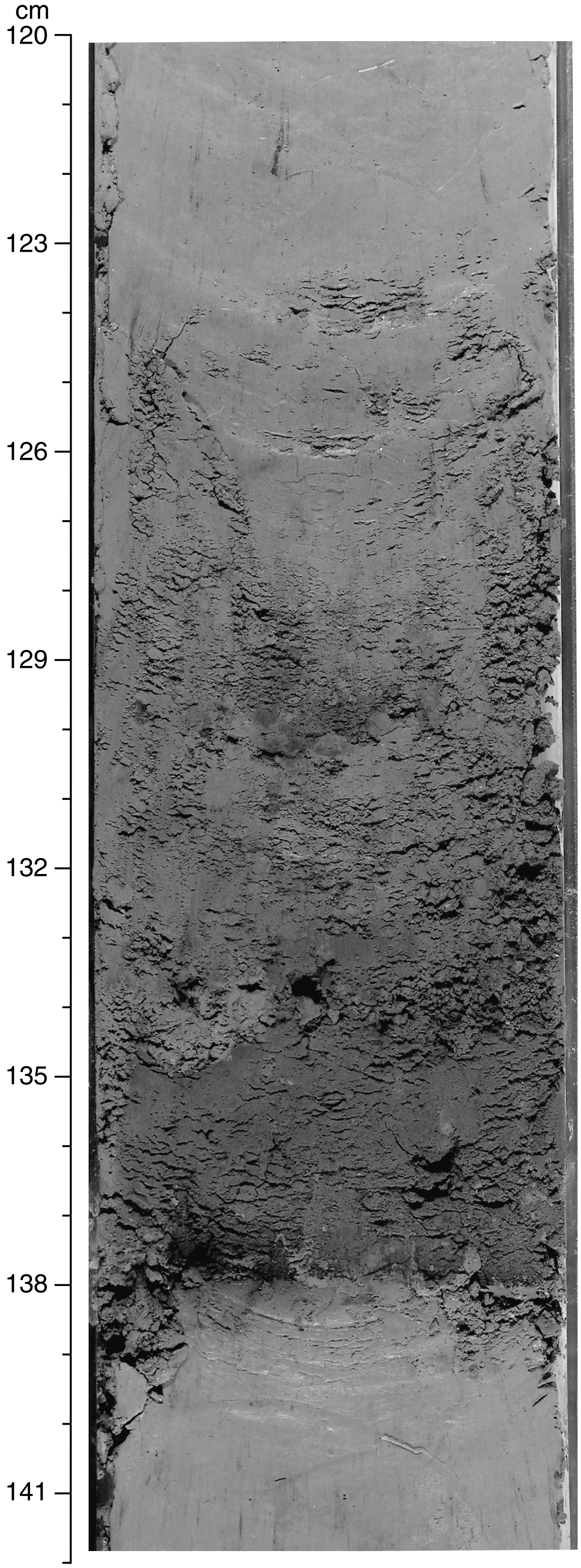

Figure F10. Base of a coarse turbidite layer (interval 184-1143C-52X-3, 13–32 cm [481.33–481.52 mbsf; 493.73–493.92 mcd]).

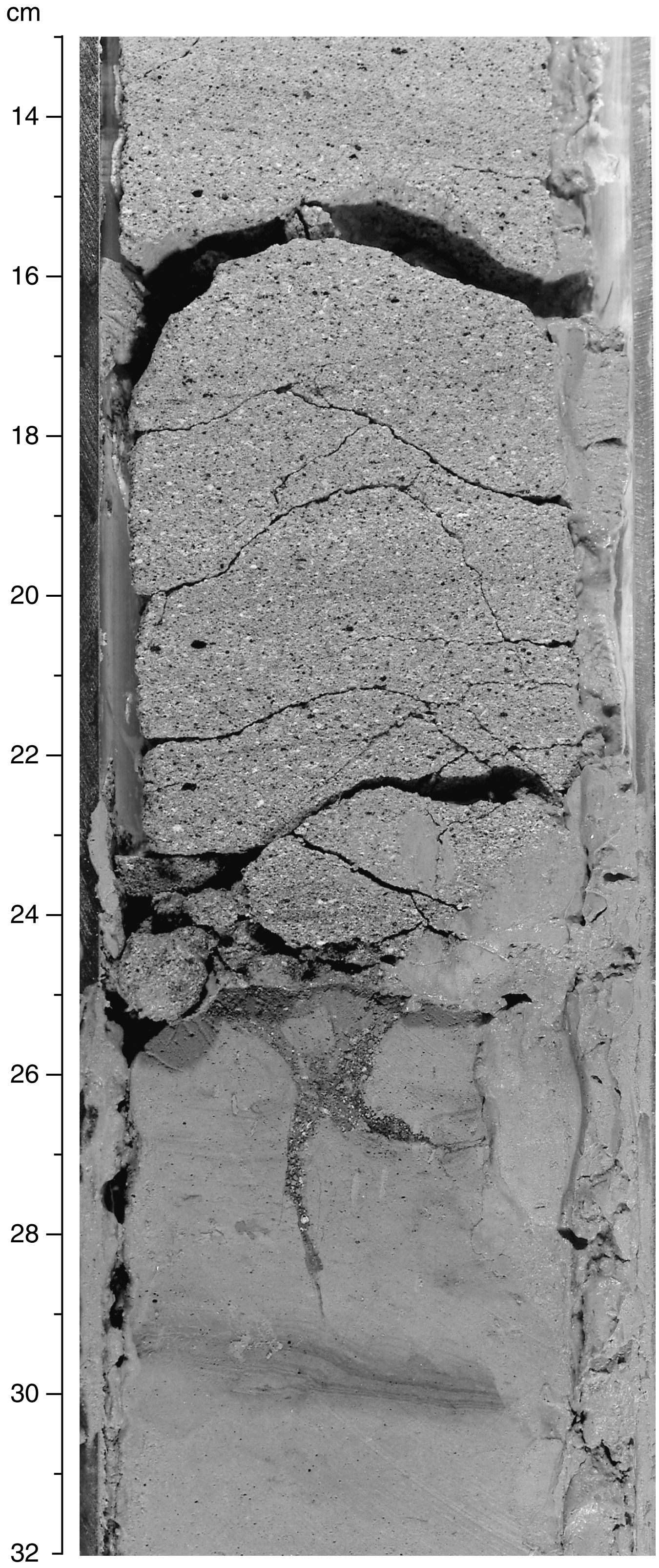

Figure F11. Age-depth plot for Site 1143. All biostratigraphic events are listed in Table T7,p. 90. The average sedimentation rate is calculated based on four control points (marked by * in Table T7, p. 90).

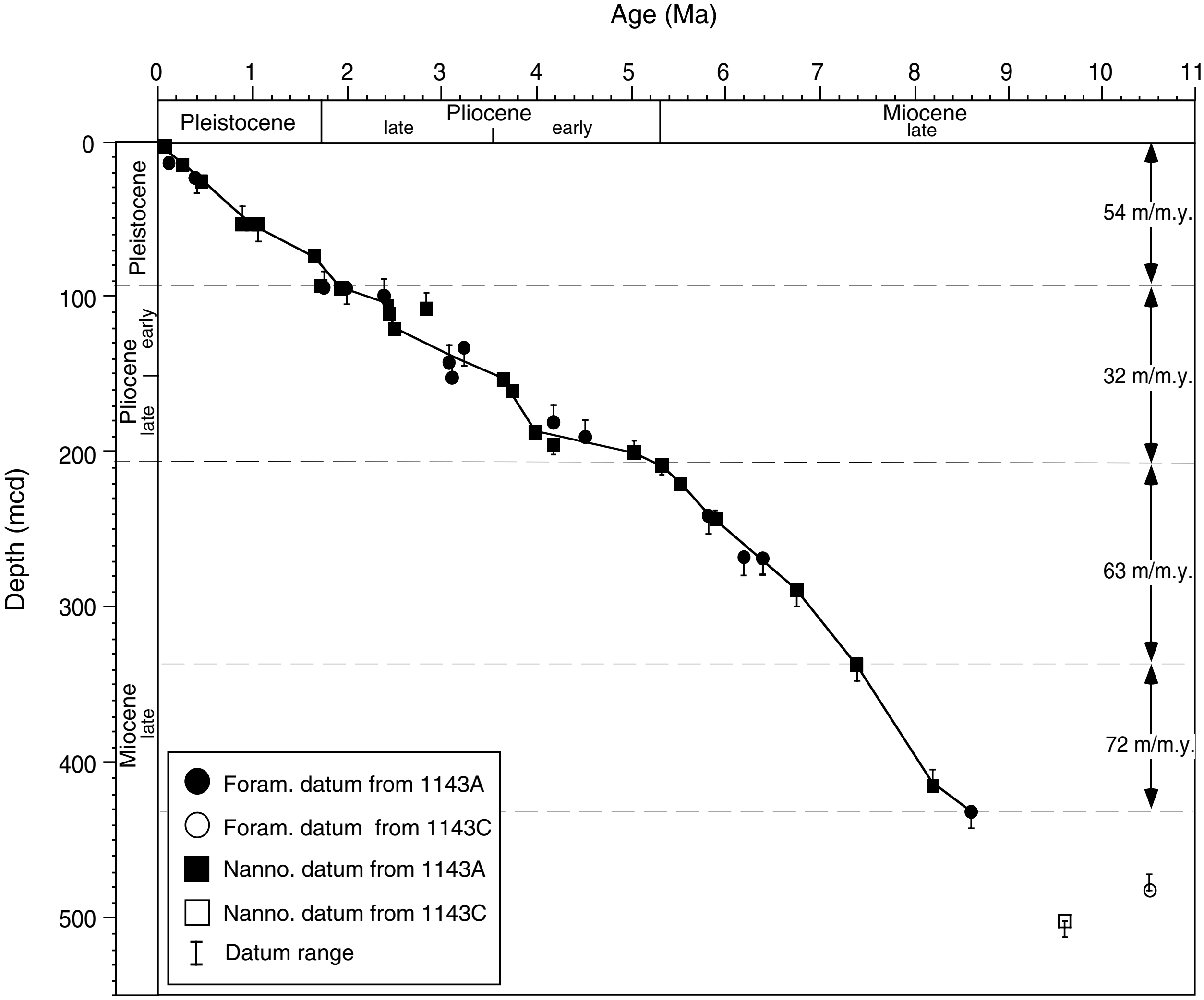

Figure F12. Explanation of the 0° declination observation by a radial inward horizontal component of magnetization (figure from Fuller et al., 1998, p. 50).

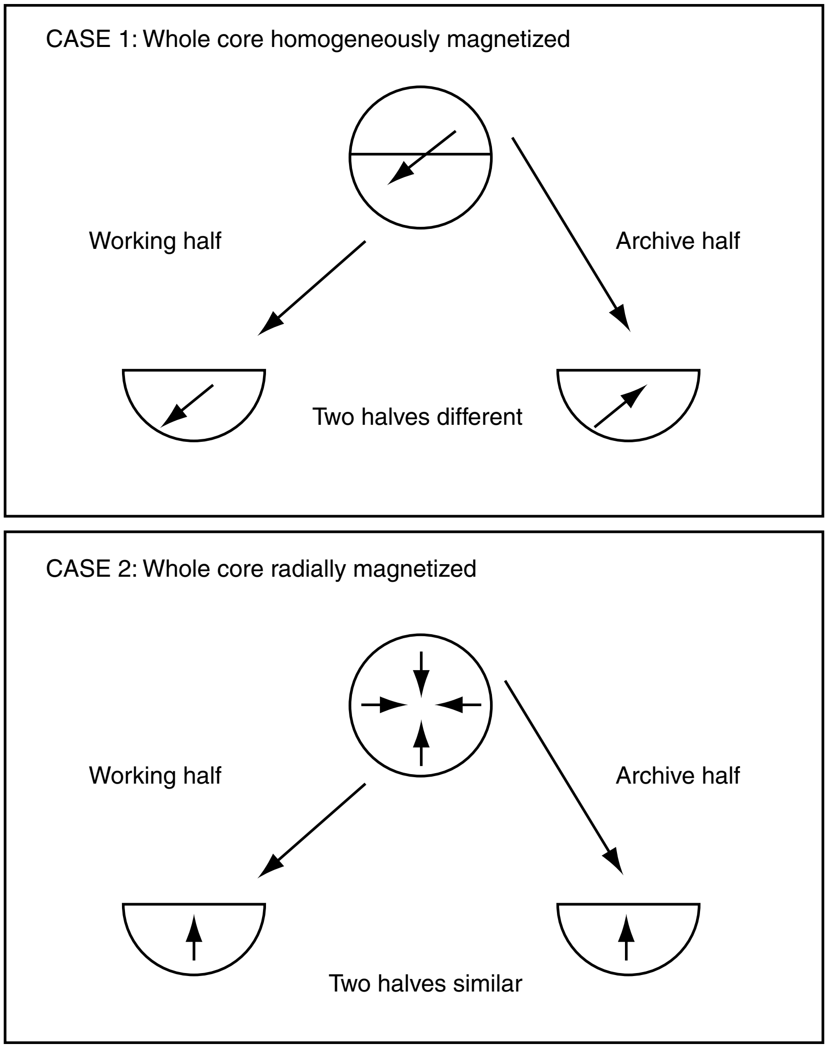

Figure F13. Alternating field demagnetization to 60 mT of Sample 184-1143A-7H-4, 93 cm. This is representative of the demagnetization characteristics of samples with strong vertical overprint. The coercivity spectra of the overprint and any remaining NRM probably overlap, leaving the final direction highly contaminated by the overprint.

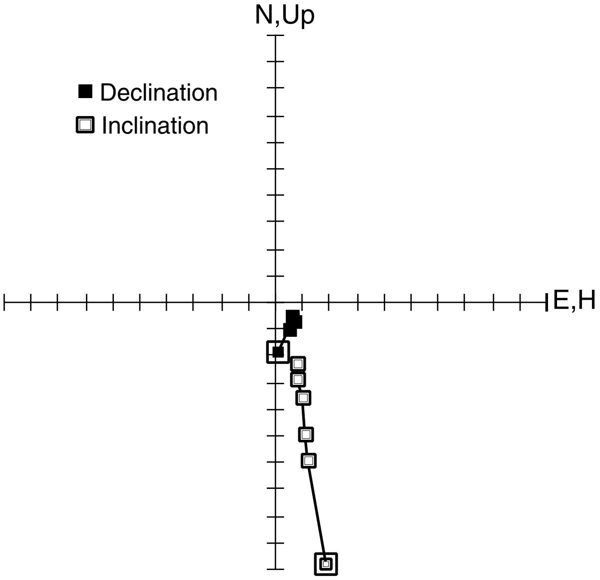

Figure F14. Tensor-corrected declination and inclination for Hole 1143A, 0–100 mcd (Cores 184-1143A-1H through 3H are not oriented). Normal polarity is observed from 0 to 43 mcd. At 43 mcd, declination changes from 0° to ~150° with a corresponding change from positive to negative inclinations. Declinations indicate reverse polarity down to ~75 mcd. Inclinations, however, become mostly steeply positive below 50 mcd.

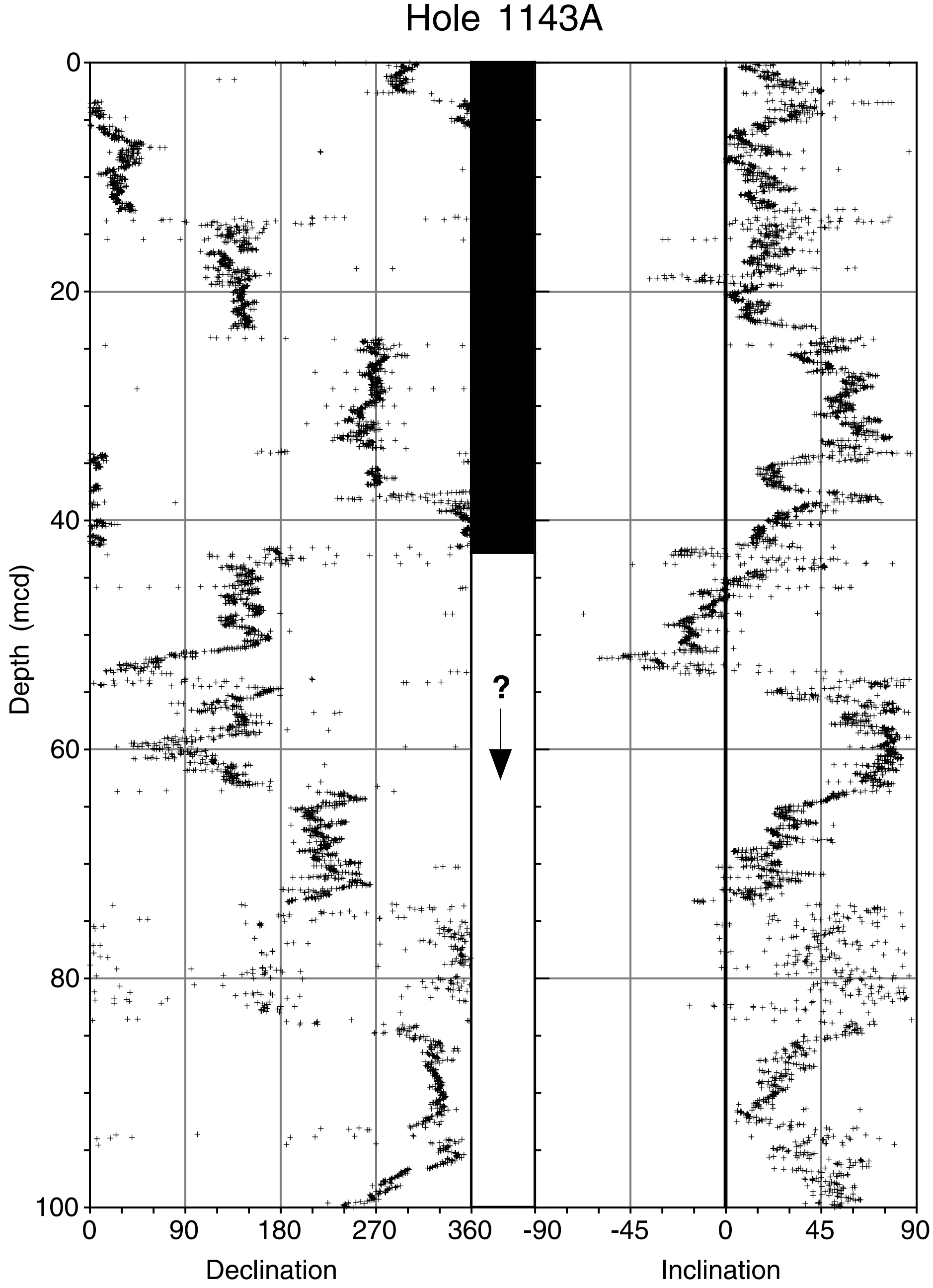

Figure F15. Declination and inclination data from Hole 1143A, 110–180 mcd. Inclinations tend to be steeply positive because of an overprint from the drill string, whereas declinations cluster around 0° due to a radial overprint. These overprints obscure the magnetostratigraphy and could not be removed by either AF demagnetization to 60 mT or thermal demagnetization to 330°C.

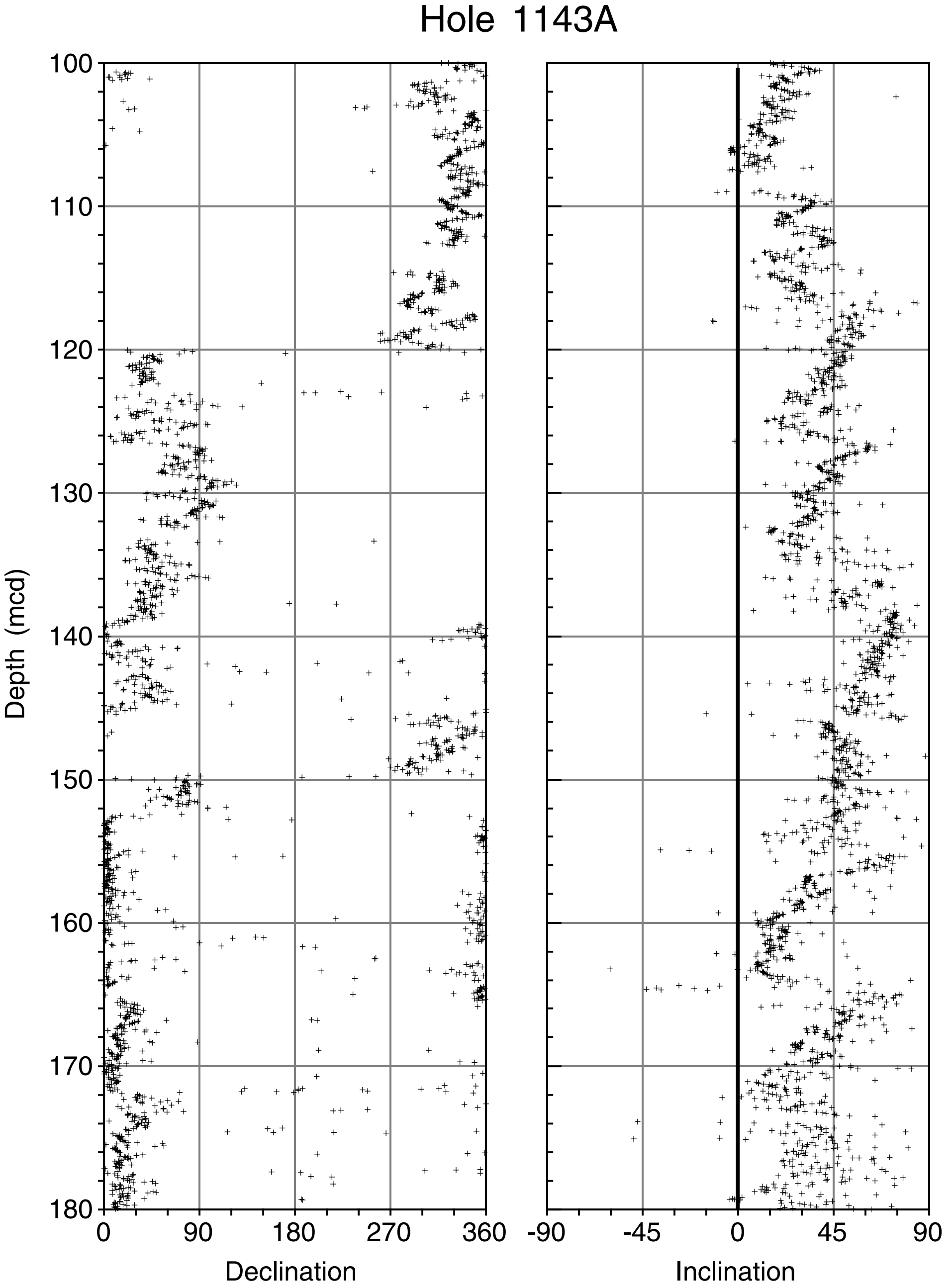

Figure F16. Inclination of cores cut with a nonmagnetic cutting shoe (even cores) and standard cutting shoe (odd cores) for Hole 1143C. Cores cut with the nonmagnetic shoe show systematically steeper inclinations than those cut with the standard shoe.

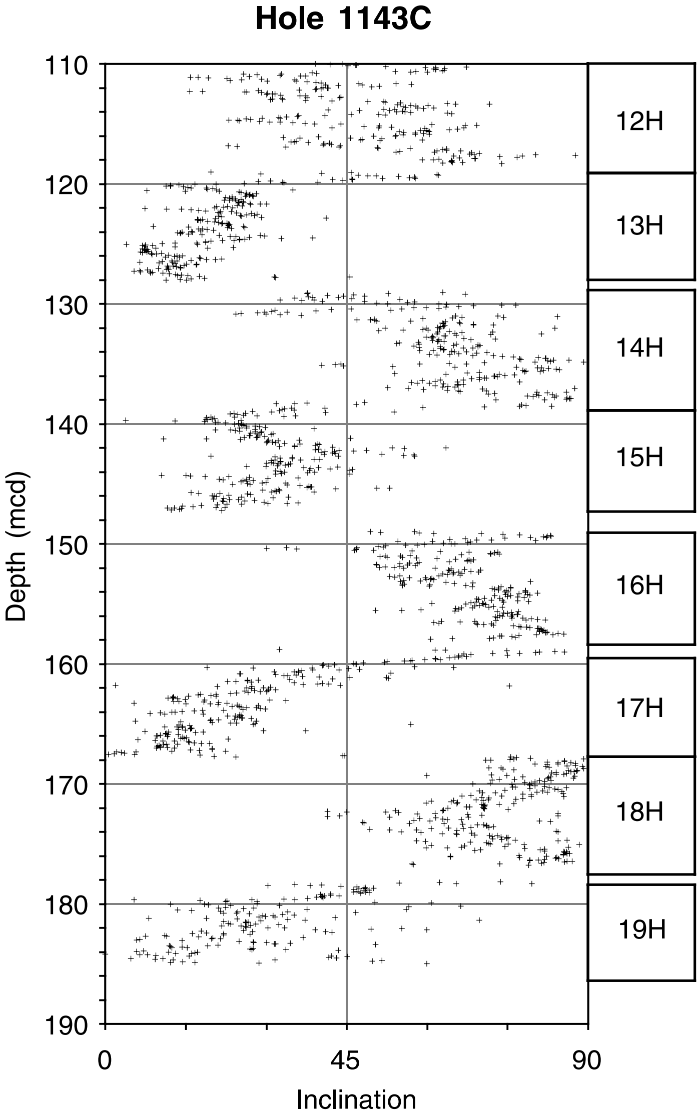

Figure F17. (**A**) Age-depth model, (**B**) linear sedimentation rates (LSR) and mass accumulation rates (MAR) vs. depth, and (**C**) LSR and MAR vs. age for Site 1143. Construction of model rates, LSR, and MAR is explained in **"Sedimentation and Accumulation Rates,"** p. 13, in the "Explanatory Notes" chapter. In (A), diamonds = calcareous nannofossils, circles = foraminifers, squares = paleomagnetic reversals; in (B) and (C), solid lines = total sediment LSR, dashed lines = carbonate LSR, stippled columns = total sediment MAR, solid columns = carbonate MAR. B/M = Brunhes/Matuyama.

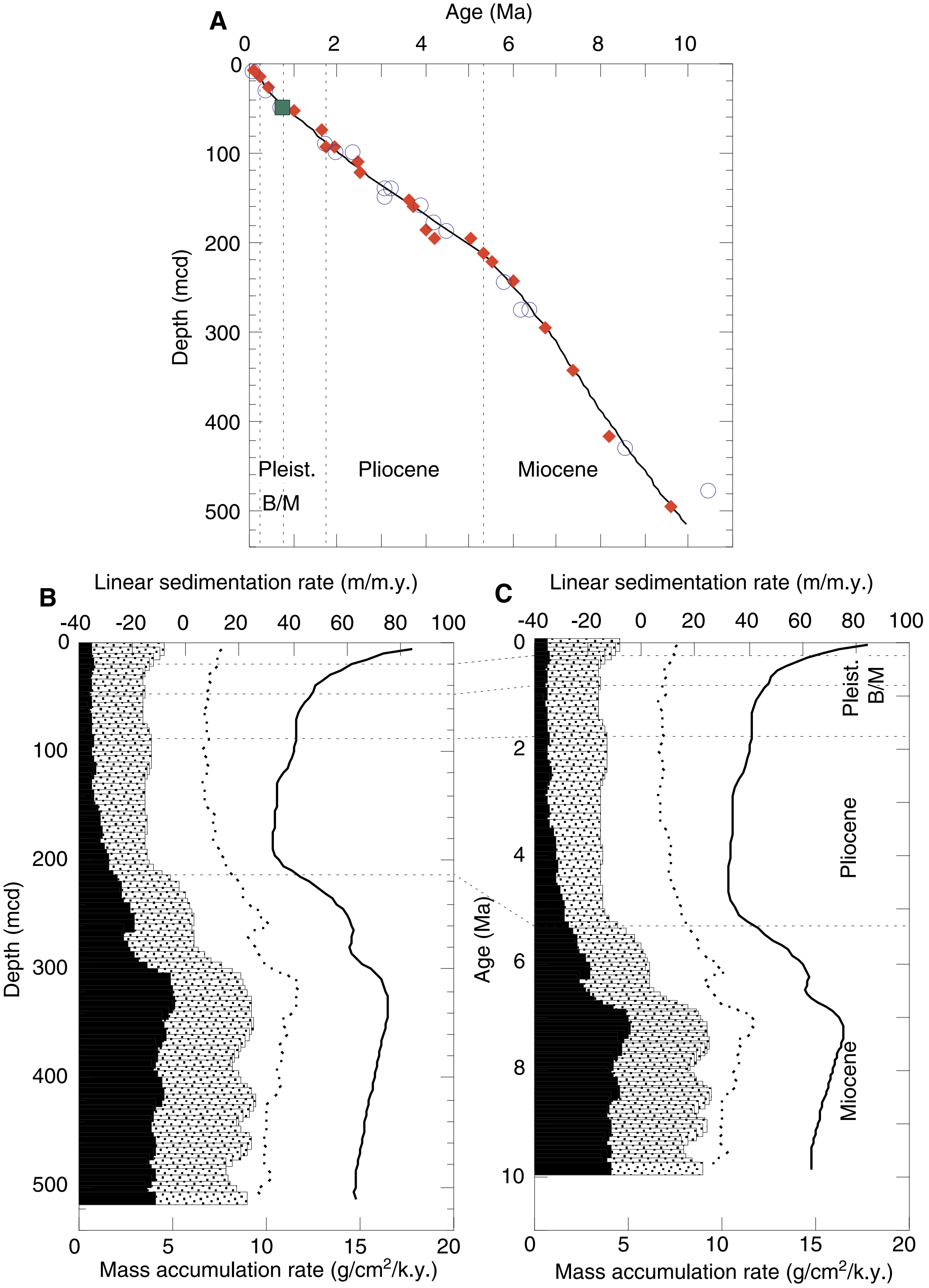

Figure F18. Carbonate values plotted vs. depth for Site 1143.

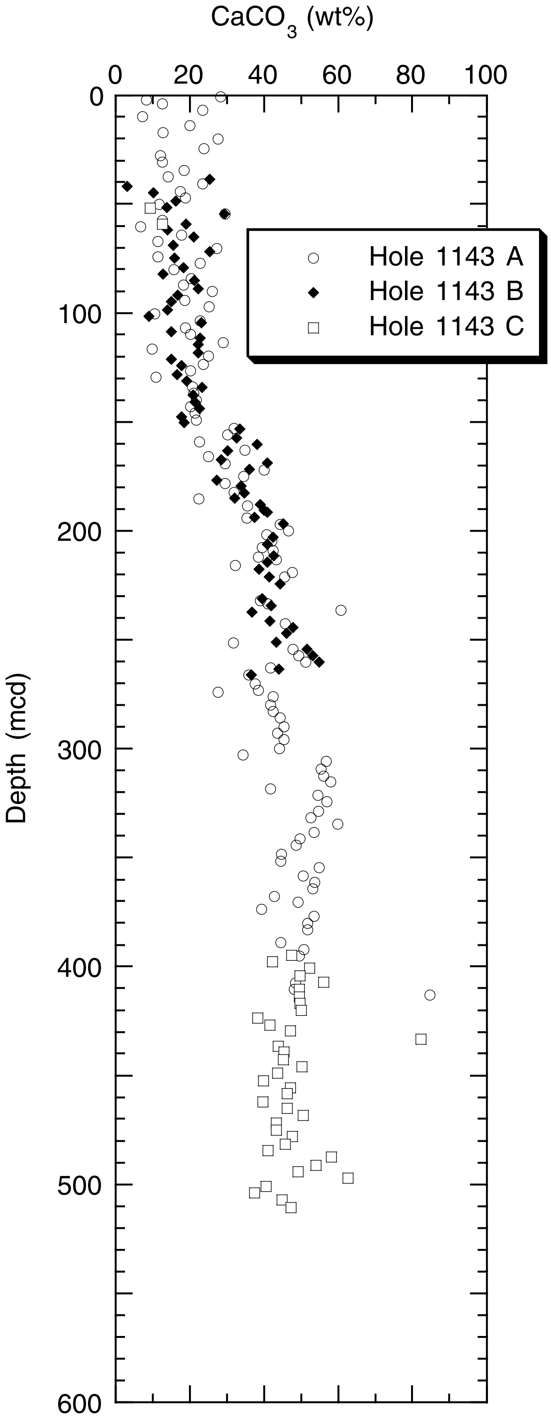

Figure F19. Total organic carbon (by difference) values vs. depth for Site 1143. TC = total carbon, IC = inorganic carbon.

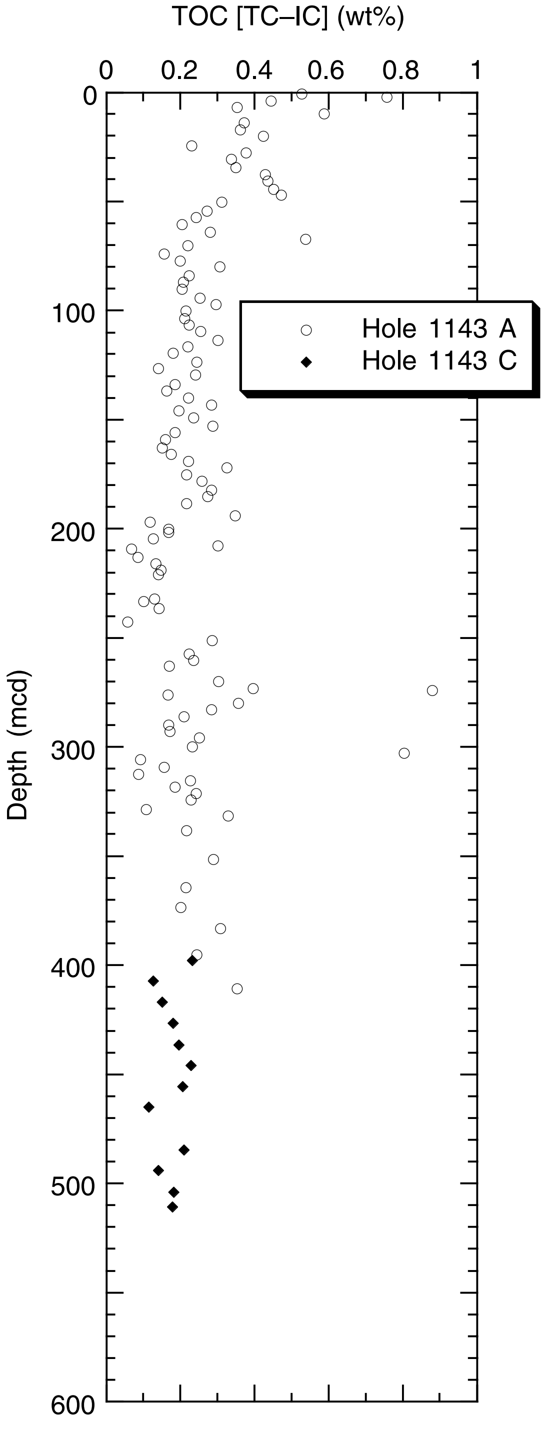

Figure F20. Vertical profiles of interstitial water measurements at Site 1143. **A.** Chloride. **B.** Salinity. **C.** Sulfate. **D.** Phosphate. **E.** Ammonium. **F.** Alkalinity. **G.** Silica. **H.** Potassium. **I.** Magnesium by ion chromatography and magnesium by titration (open diamonds). **J.** Calcium by ion chromatography and calcium by titration (open diamonds). **K.** Calcium vs. magnesium. **L.** Lithium. **M.** Strontium concentrations in Hole 1143A (solid circles) and Hole 1143C (open circles).

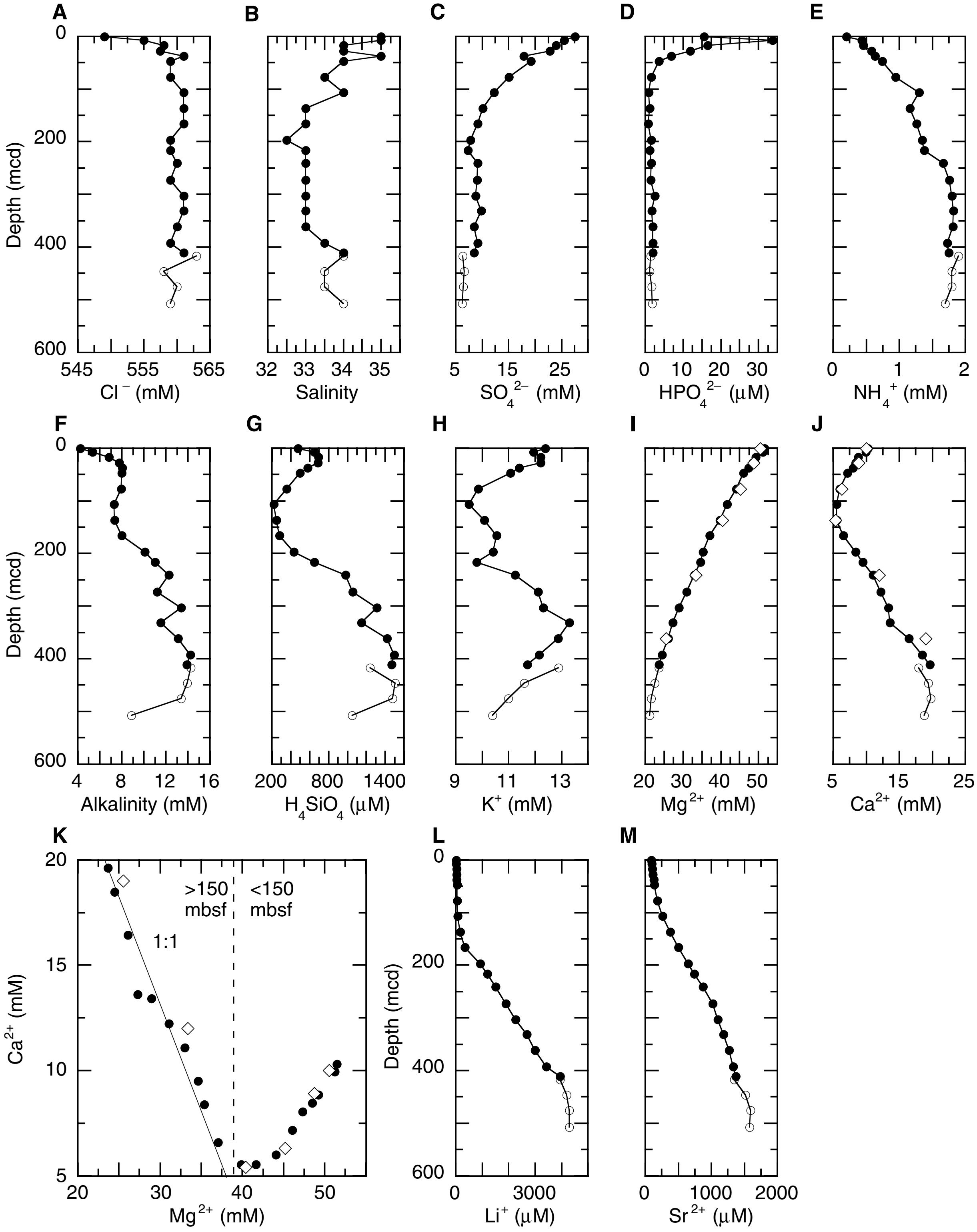

Figure F21. Grain density measurements (solid circles) at Site 1143 plotted for each hole. APC = advanced hydraulic piston corer, XCB = extended core barrel.

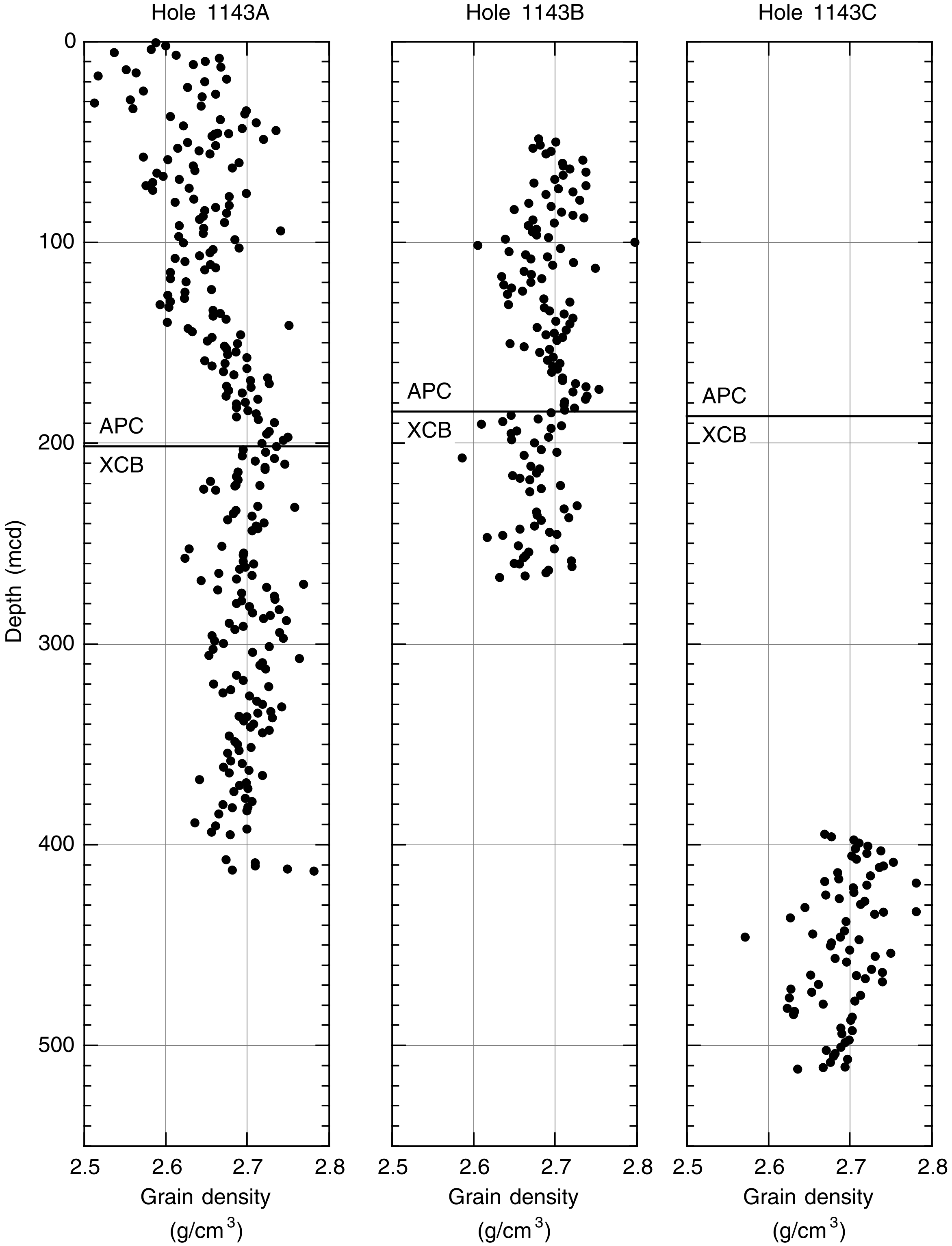

Figure F22. Bulk density measurements from GRA (line) and MAD (open circles) methods at Site 1143, plotted for each hole. APC = advanced hydraulic piston corer, XCB = extended core barrel.

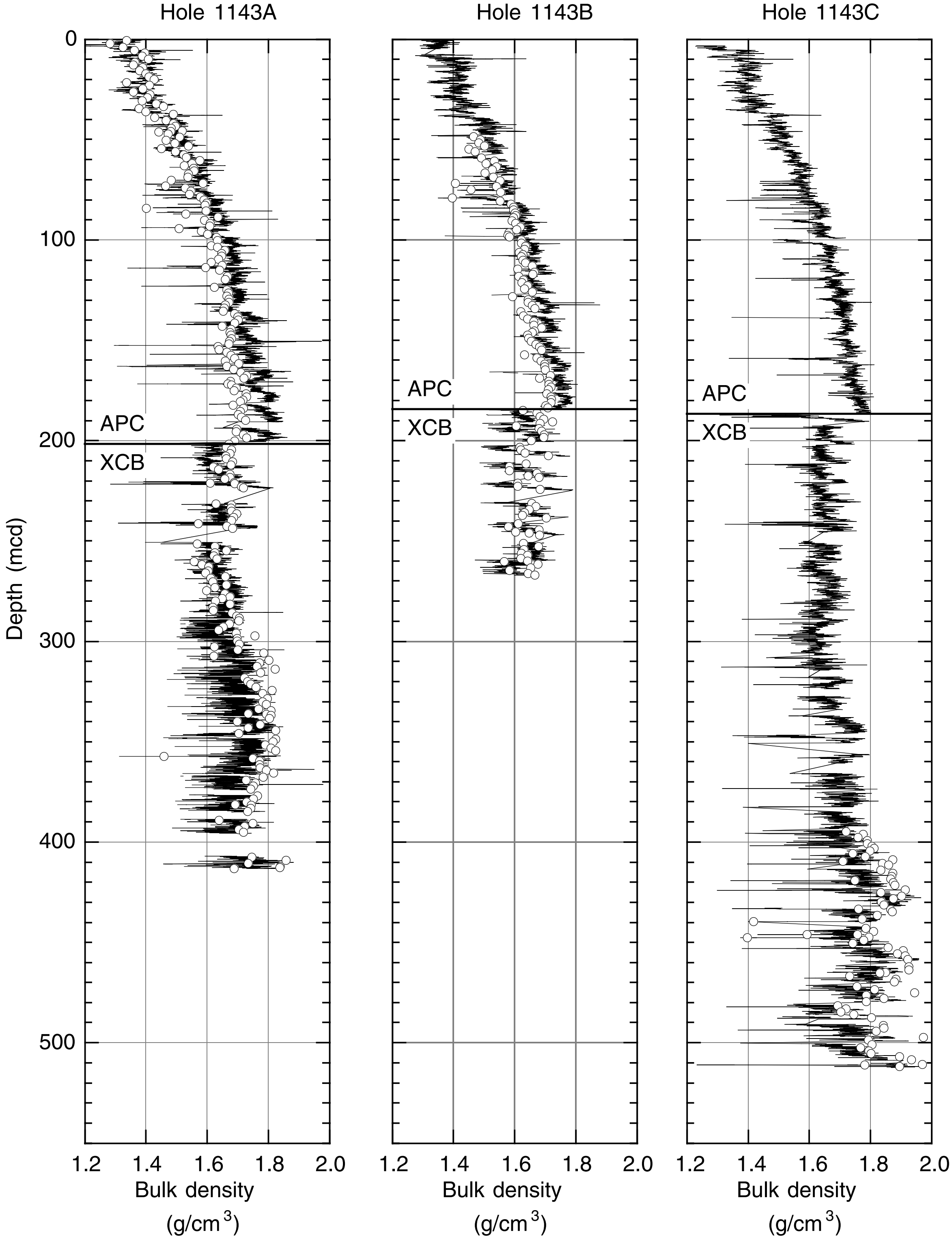

Figure F23. Comparison of bulk density measurements from gamma-ray attenuation (GRA) and moisture and density (MAD) methods at Site 1143. Solid circles = APC cores, open circles = XCB cores.

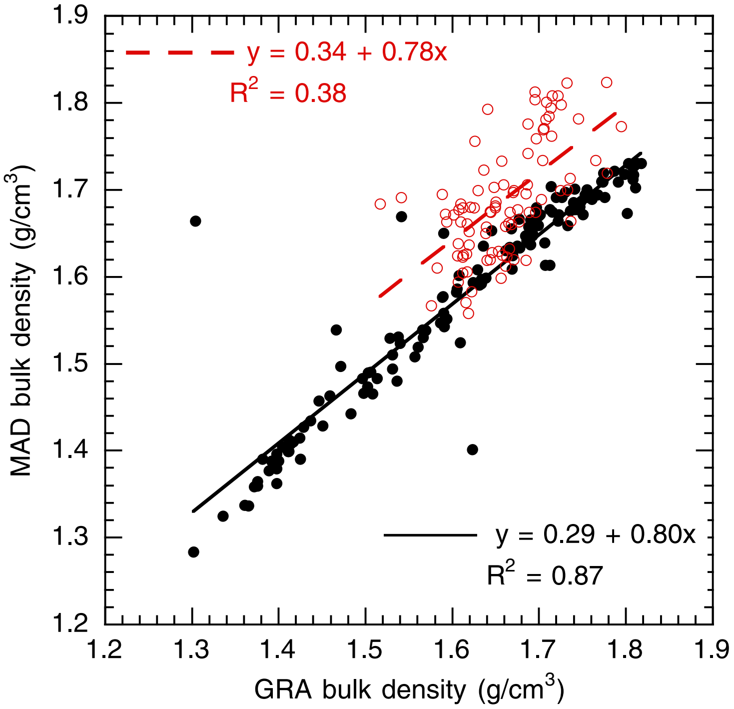

Figure F24. Porosity values (solid circles) obtained from the MAD method. Dashed lines are power curve fits to extreme values at given depth intervals and represent envelope trends. APC = advanced hydraulic piston corer, XCB = extended core barrel.

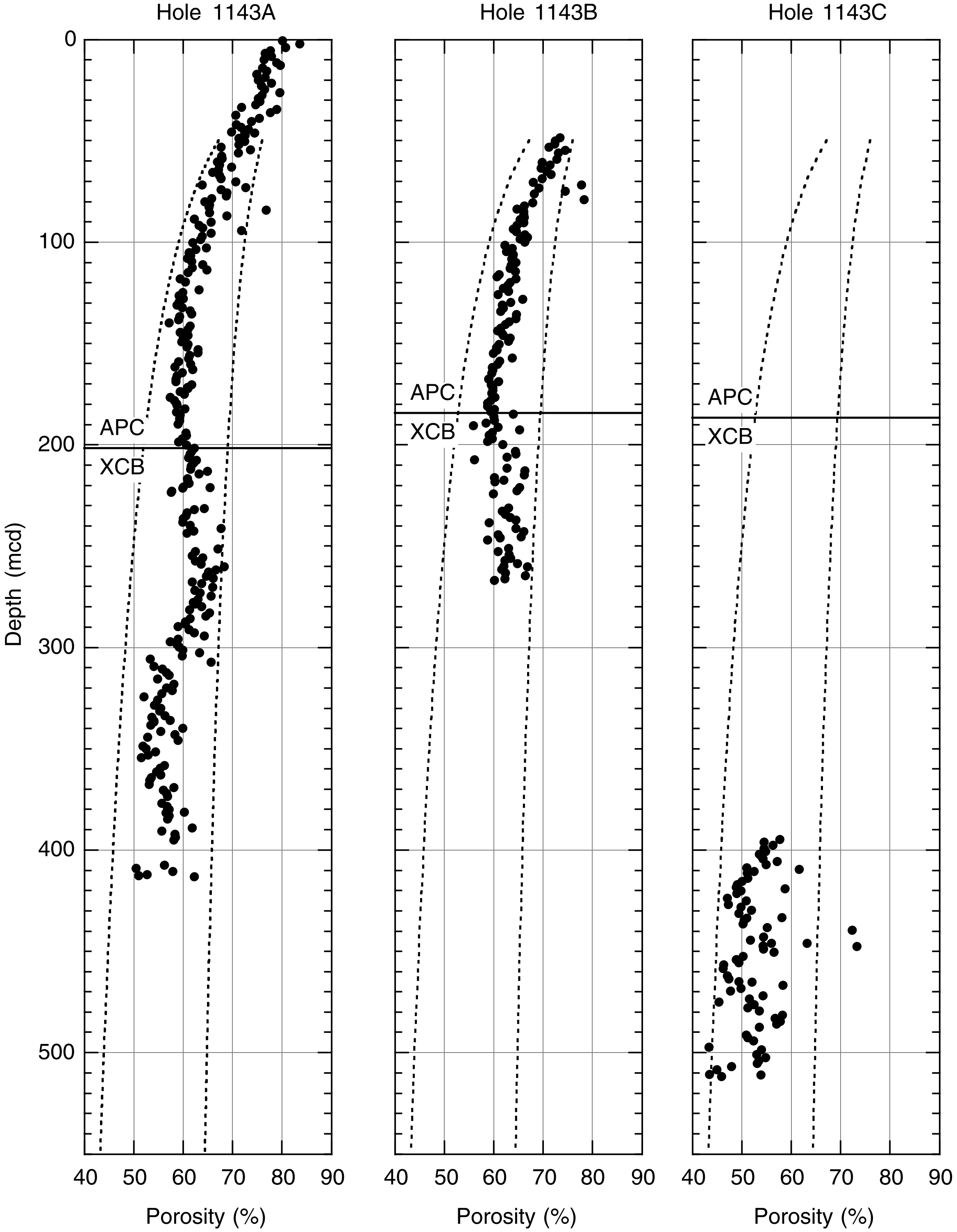

Figure F25. Magnetic susceptibility measurements at Site 1143 plotted for each hole. APC = advanced hydraulic piston corer, XCB = extended core barrel.

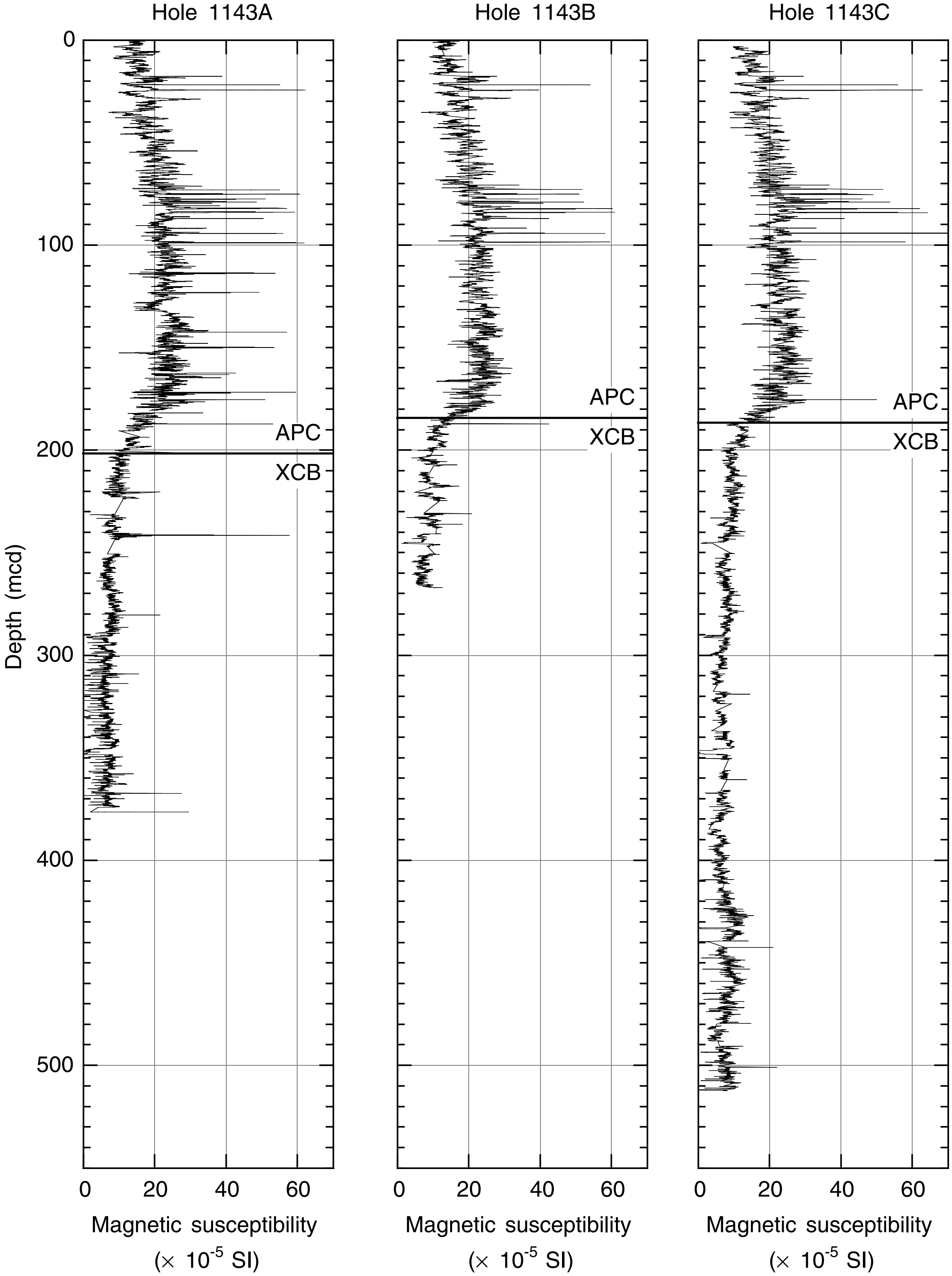

Figure F26. Natural gamma radiation measurements at Site 1143, smoothed with a 20-point moving average plotted for each hole. APC = advanced hydraulic piston corer, XCB = extended core barrel.

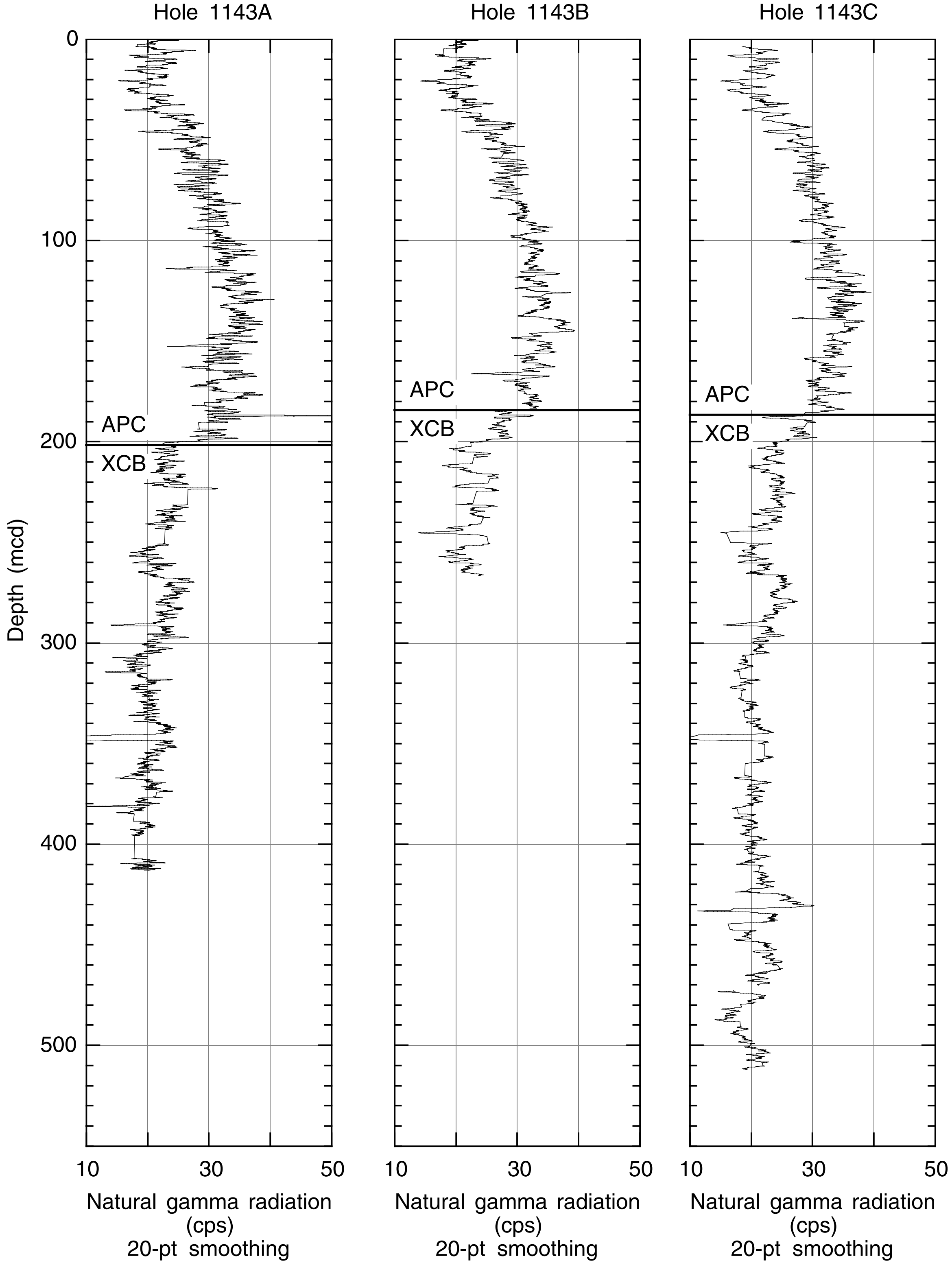

Figure F27. Color reflectance measurements from split-core surfaces at Site 1143, smoothed with a 20-point moving average, plotted for each hole. L*, a*, and b* are standard parameters calculated by the Minolta CM-2002 photospectrometer from the spectral data. L* = black line, a*/b* = gray line, APC = advanced hydraulic piston corer, XCB = extended core barrel.

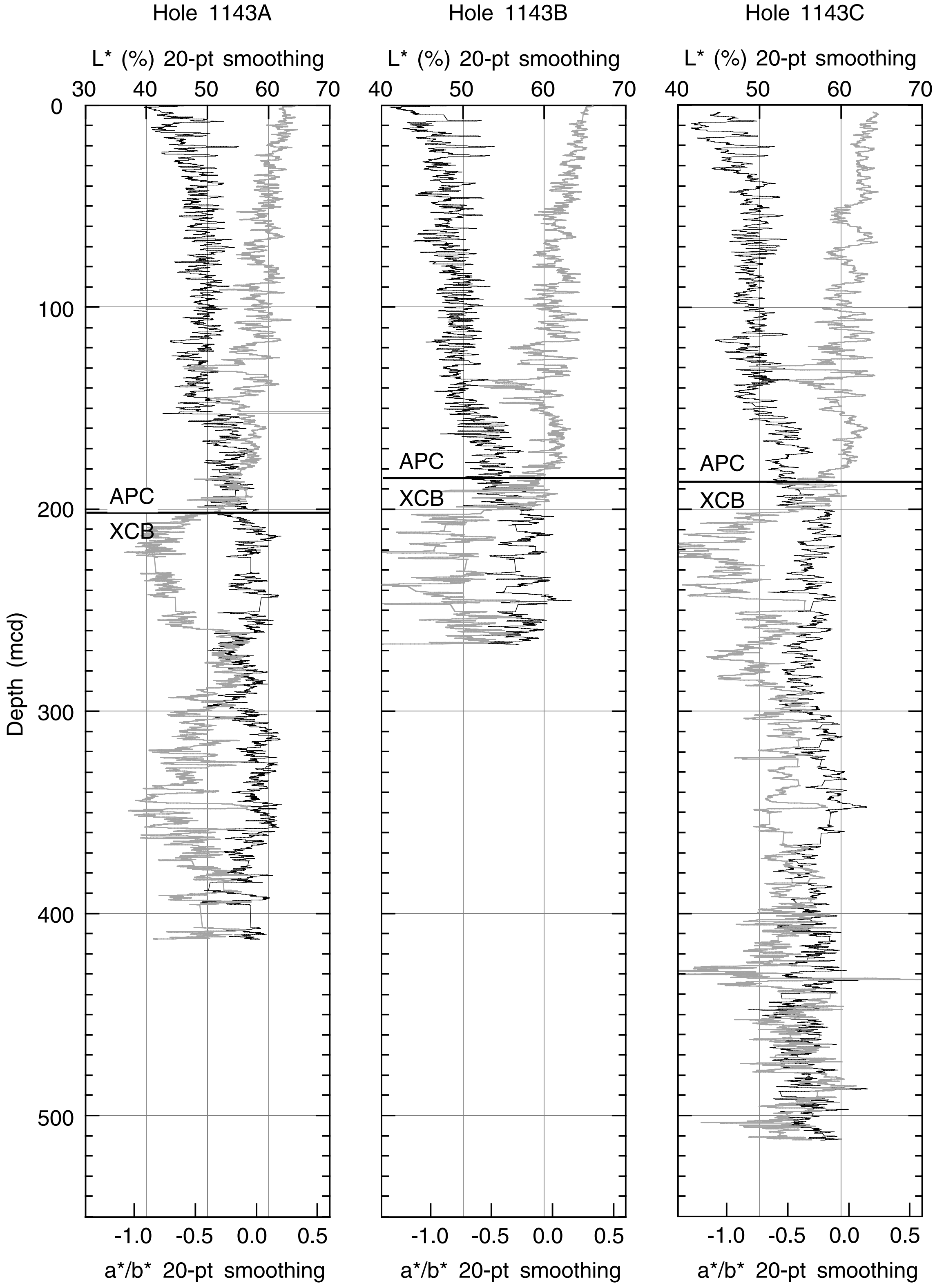

Figure F28. *P*-wave velocity measurements at Site 1143 plotted for each hole.

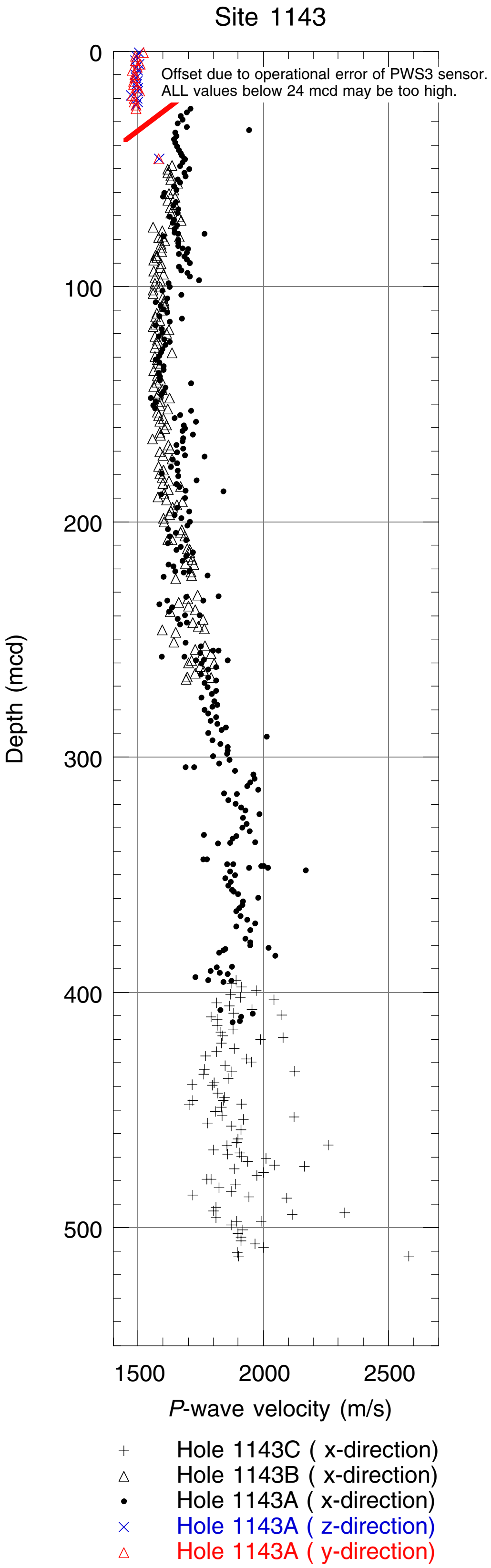

Figure F29. Thermal conductivity measurements at Site 1143. APC = advanced hydraulic piston corer, XCB = extended core barrel.

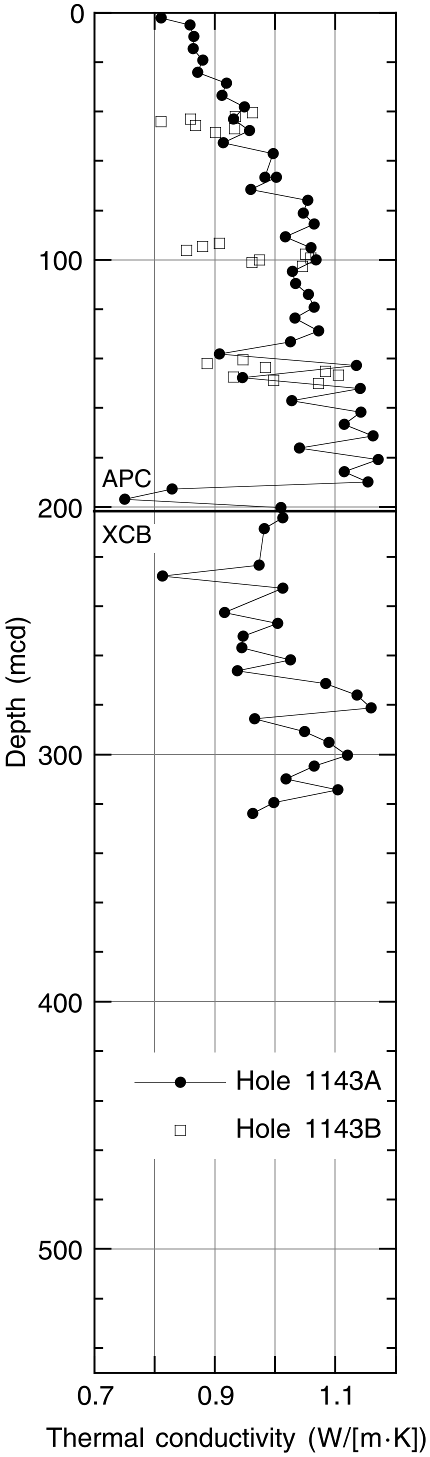

Figure F30. Comparison of bulk density (MAD) and thermal conductivity measurements at Site 1143. Solid circles = APC, open circles = XCB. Regression is for APC cores only.

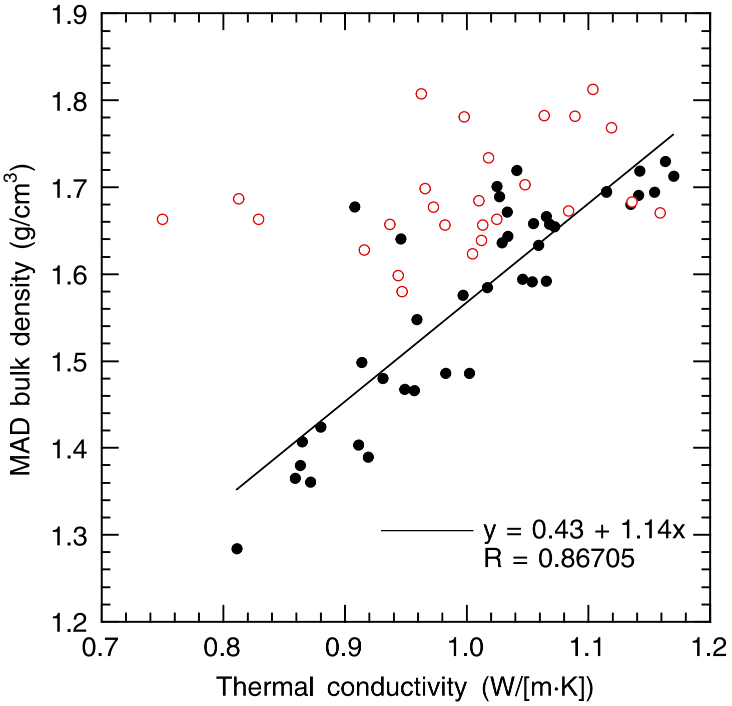

Figure F31. Downhole temperature measurements at Site 1143. **A.** Bottom-water temperature at Hole 1143B taken before Core 184-1143B-1H was shot. This value is taken as approximate bottom-water temperature at Site 1143. **B–E.** Downhole sediment temperature records and calculated equilibrium temperatures at Hole 1143A. Open circles = original temperature measurements, solid circles = selected section of data used in calculating the equilibrium temperature.

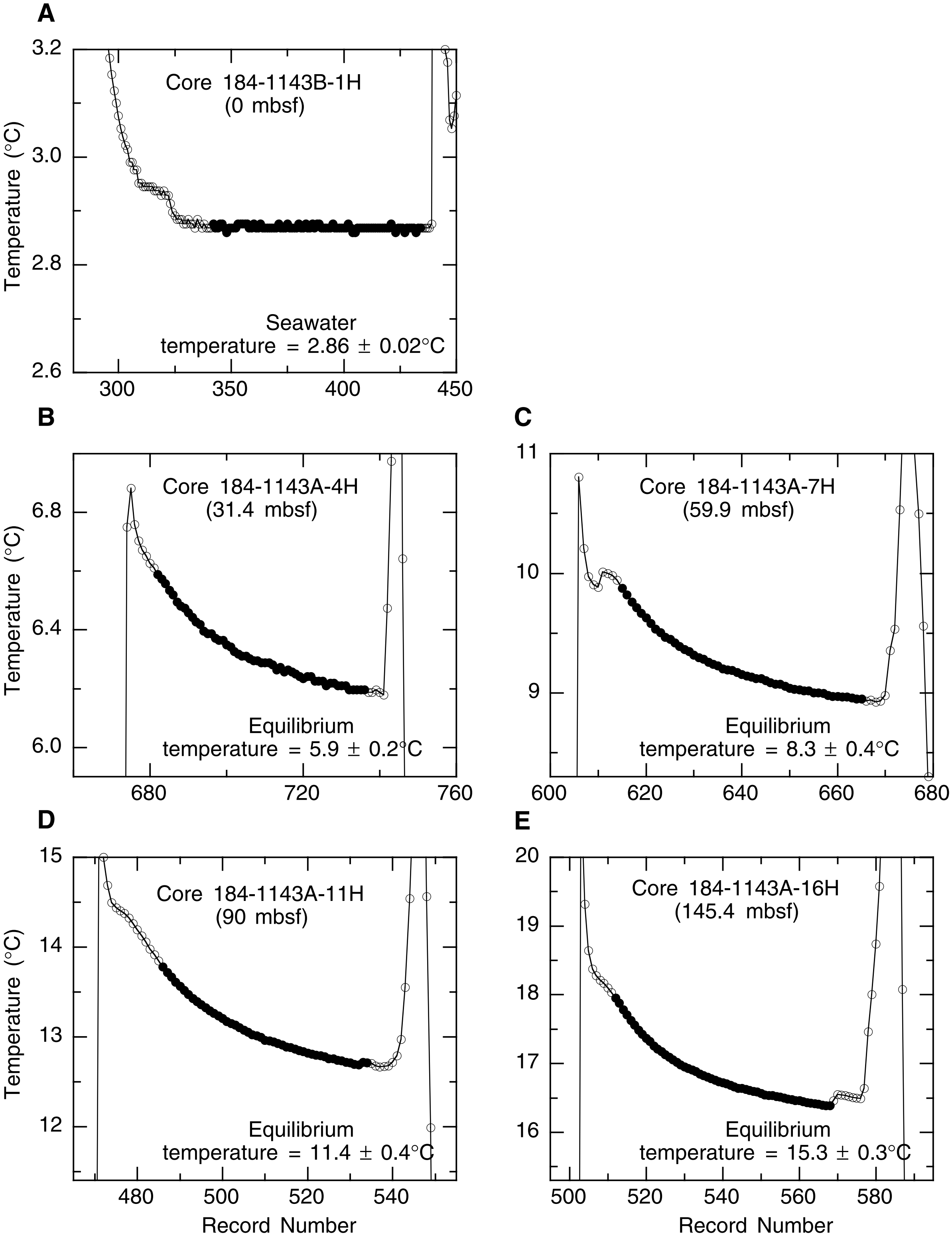

Figure F32. Downhole temperature gradient at Site 1143. T = temperature (°C) at depth (mbsf), R = correlation coefficient.

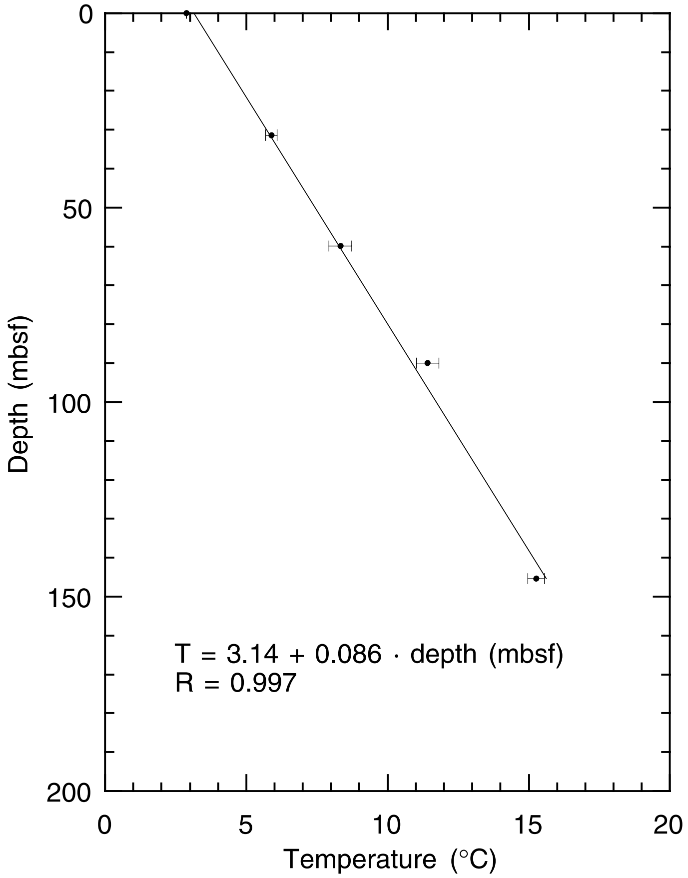

Figure F33. Graphic summary of downhole logging operations for Hole 1143A. The seafloor was identified based on a step in natural gamma activity at the sediment/water boundary. FMS = Formation MicroScanner, LSS = long-spaced sonic.

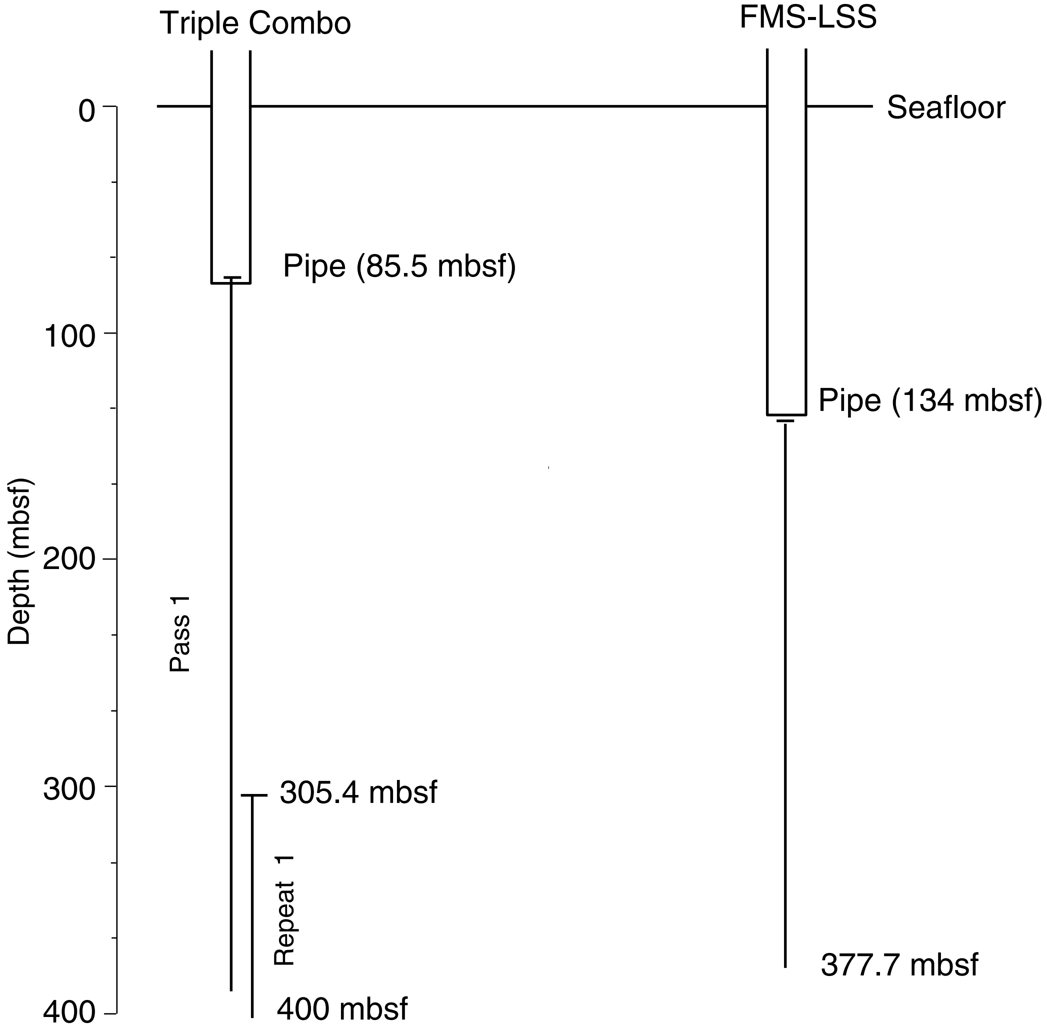

Figure F34. Downhole logs of hole diameter, computed gamma ray (HCGR), bulk density, neutron porosity (neut.), density-derived porosity (dens.), electrical resistivity (spherically focused log [SFL], medium induction phasor-processed resistivity [IMPH], deep induction phasor-processed resistivity [IDPH]), and *P*-wave velocities from Hole 1143A. Comparison of logging data and core-derived lithostratigraphy (see **"Lithostratigraphy,"** p. 8) in Hole 1143A is also shown. Shaded intervals mark distinct features in the logs that correspond to turbidites/slumps. The integrated interpretation of FMS images and standard logs enables identification of the displayed interval boundaries. Dashed lines = general trends of some particular curves. (**Figure shown on next page.**)

Figure F34. (Caption on previous page.)

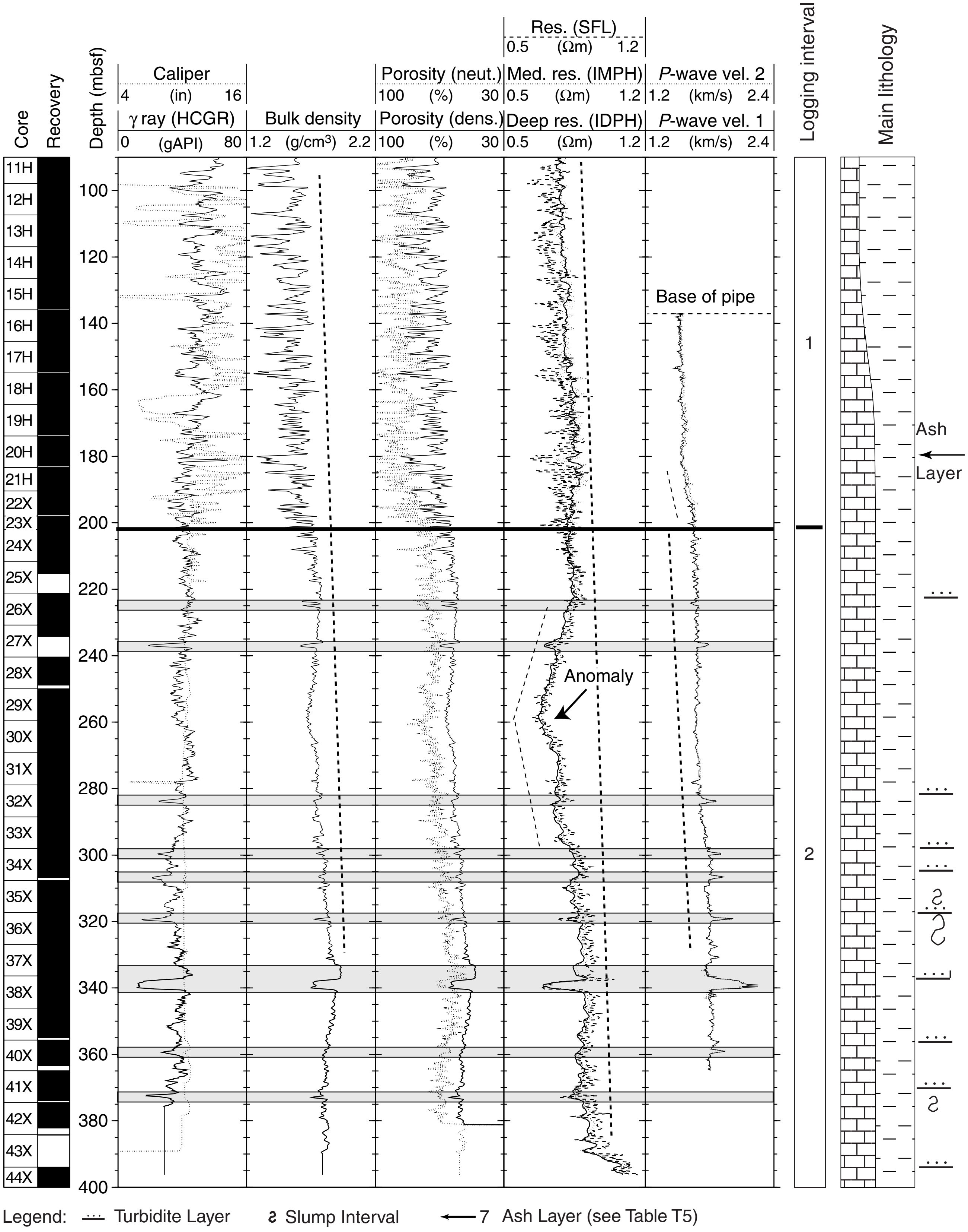

Figure F35. Downhole logs from the hostile environment natural gamma-ray sonde (HNGS) tool on the triple combo tool suite. HCGR = computed gamma ray, HSGR = standard gamma ray, NGT = natural gamma-ray tool. Shaded interval marks distinct drop in all records corresponding to a turbidite (see Fig. **F40,** p. 80, and **"Lithostratigraphy,"** p. 8).

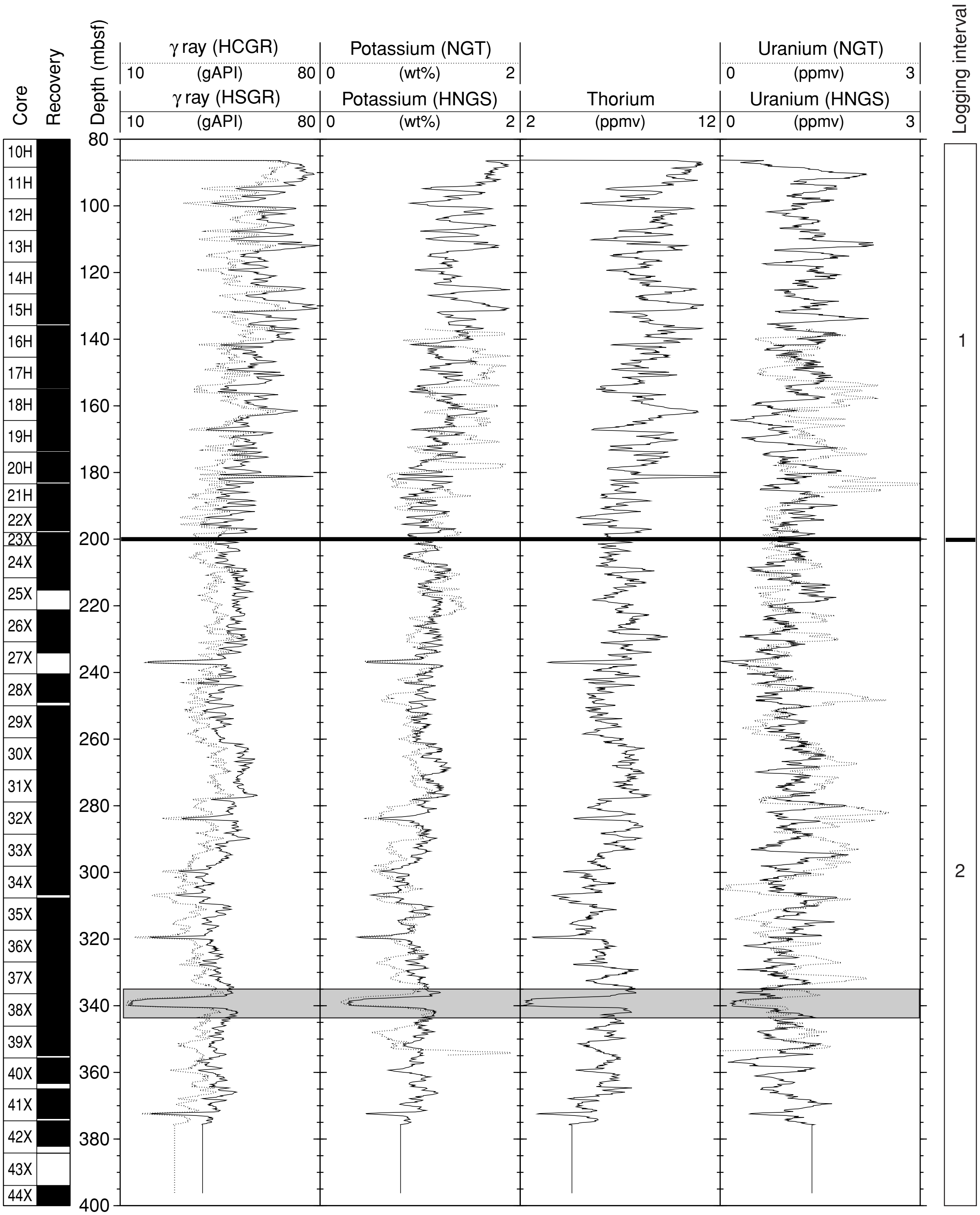

Figure F36. Comparison of *P*-wave velocities from downhole logs with physical properties measurements from core logging (see **"Physical Properties,"** p. 23) and of densities determined from downhole logs and MST gamma-ray attenuation bulk density measurements.

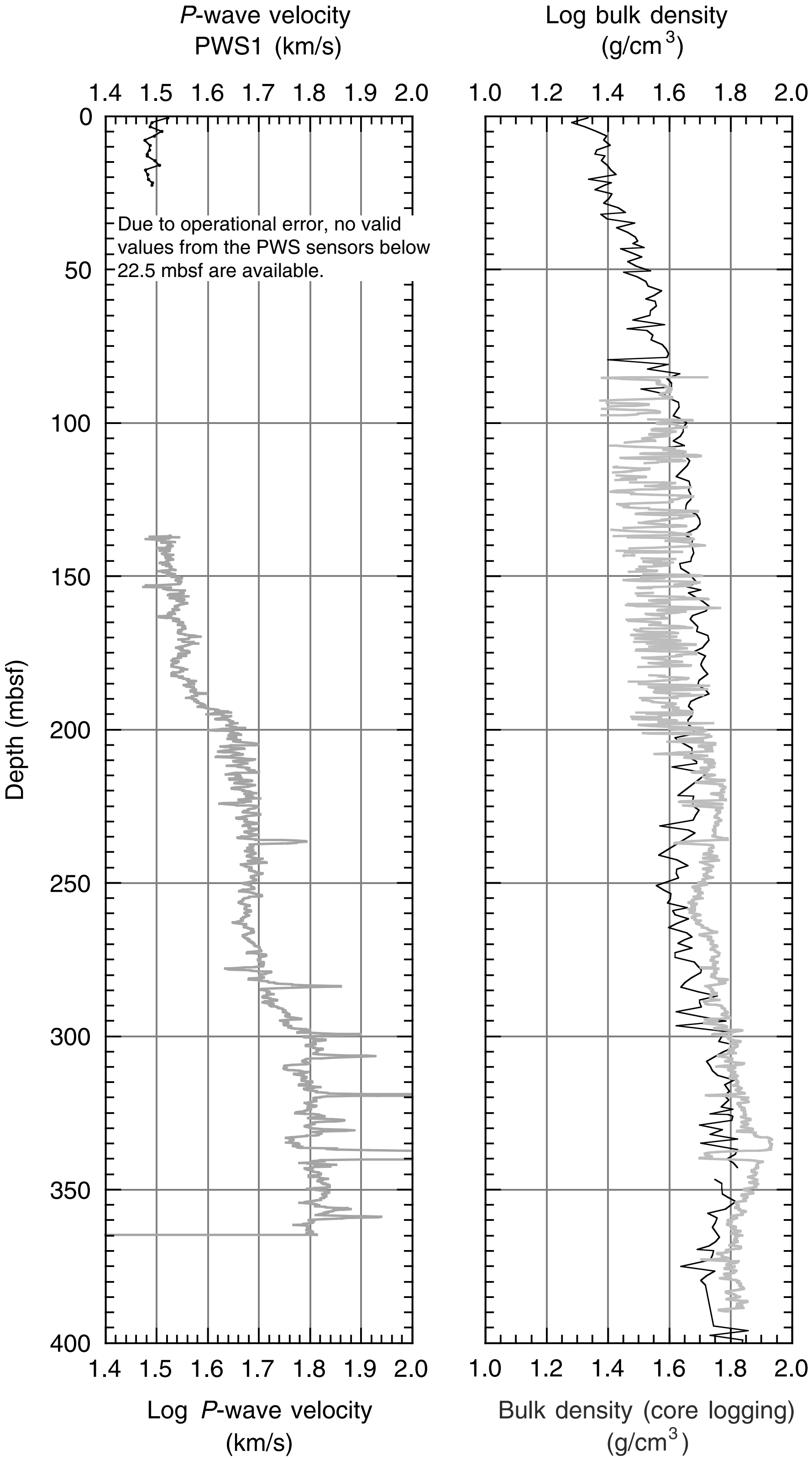

Figure F37. Comparison of spectral gamma ray from downhole logs with multisensor track (MST) natural gamma-ray (NGR) data and of porosities determined from downhole logs and discrete core samples. MAD = moisture and density.

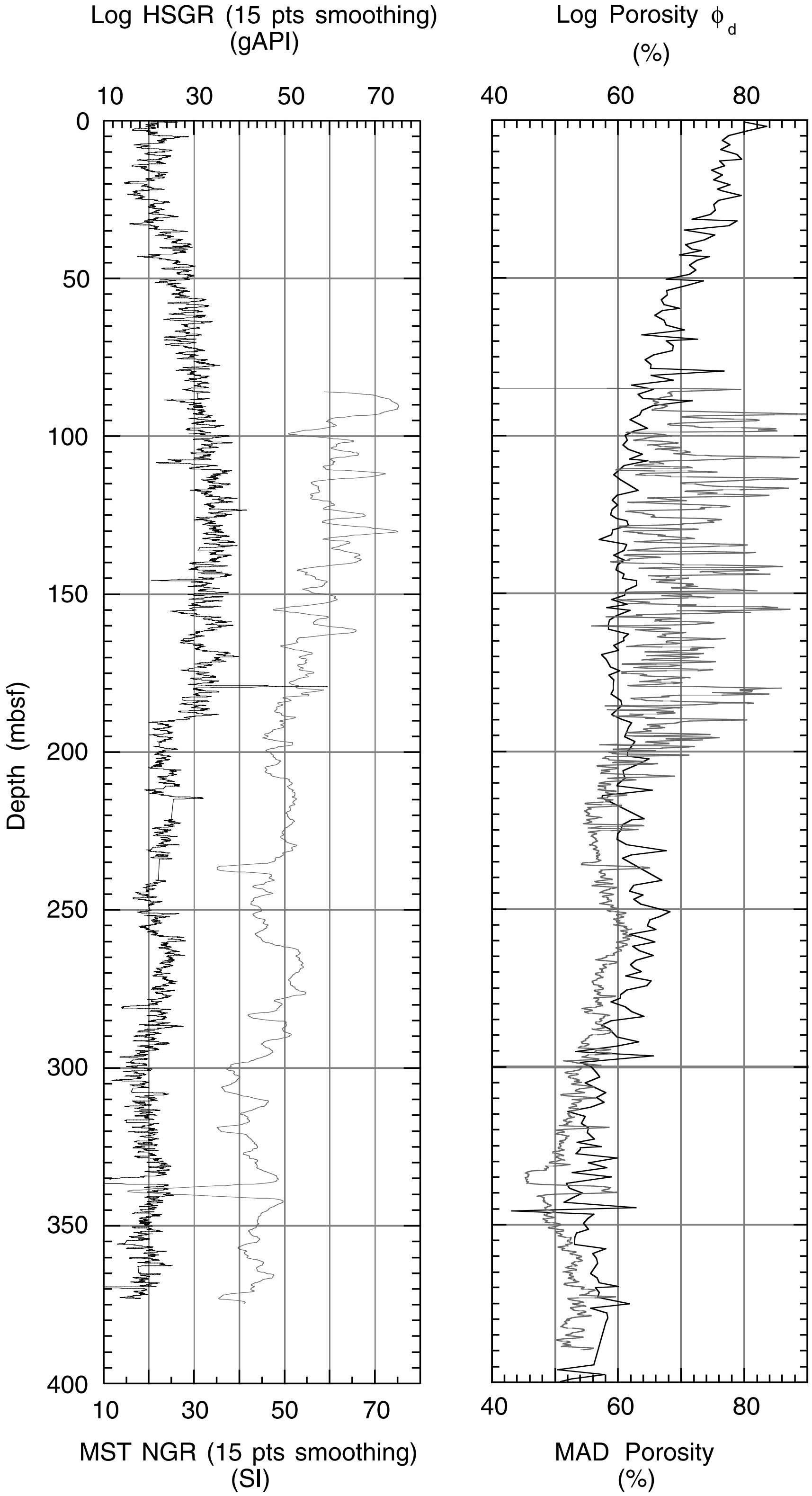

Figure F38. Comparison of the computed gamma ray (HCGR), medium resistivity (IMPH), and photoelectric effect (PEF) logs with carbonate content (see **"Organic Geochemistry,"** p. 18).

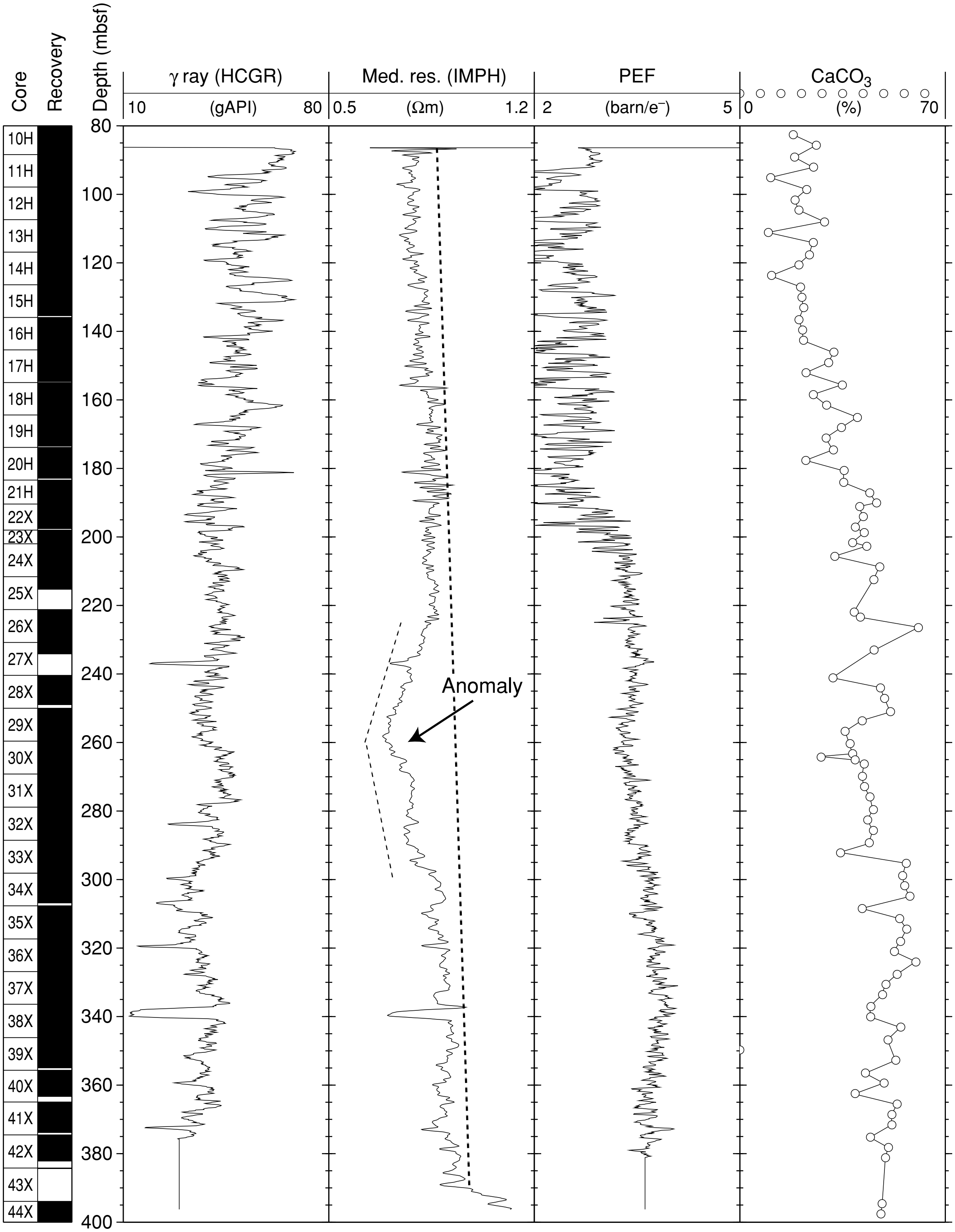

Figure F39. Formation MicroScanner (FMS) image displaying alternation of darker and lighter intervals compared to the lightness curve (see "Physical Properties," p. 23). The sediment reveals bedding structures, which can be related to the slump seen in Core 184-1143A-36X. Horizontal exaggeration is ~8×.

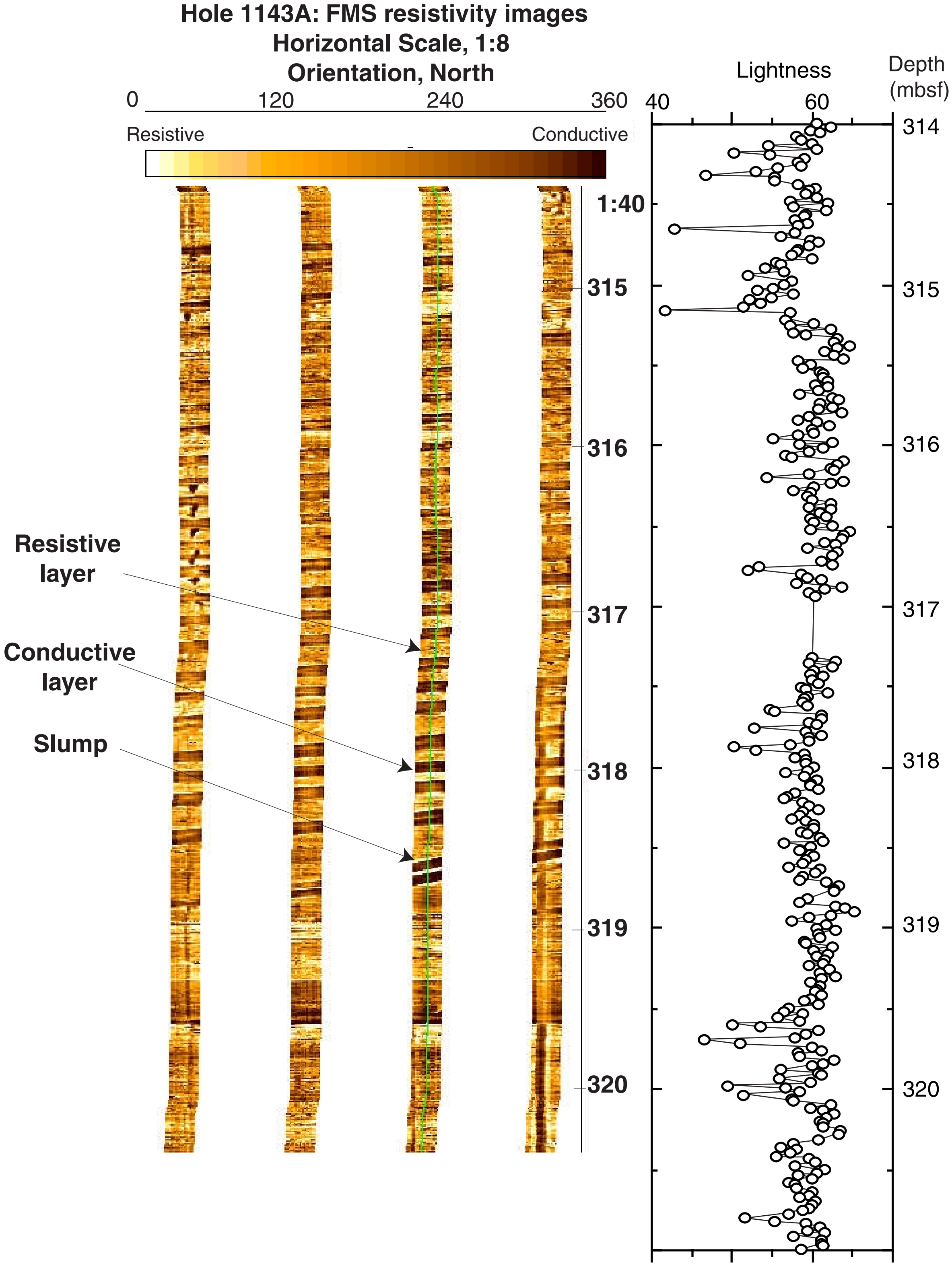

Figure F40. Formation MicroScanner (FMS) image displaying the major turbidite seen in Cores 184-1143A-37X and 38X (see "Lithostratigraphy," p. 8). Horizontal exaggeration is ~8×.

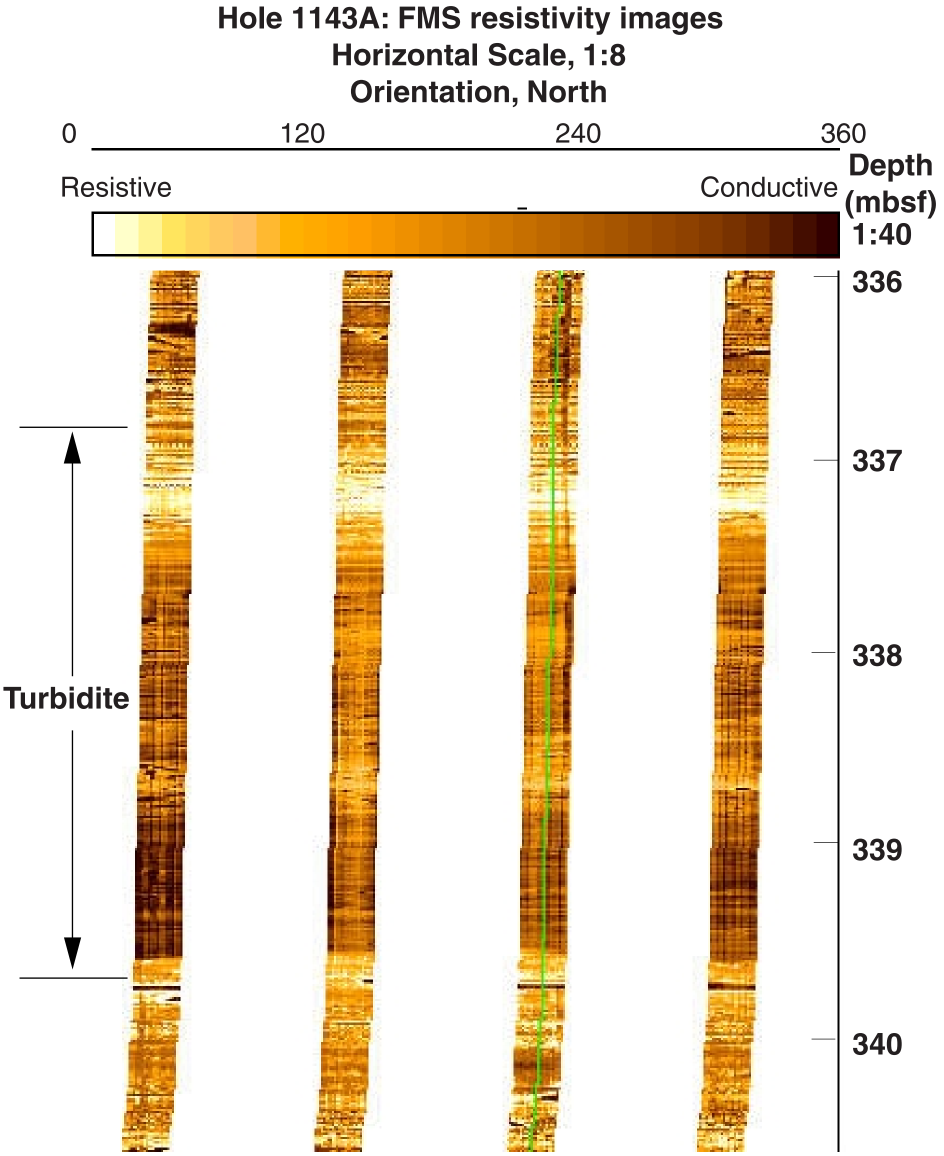

Table T1. Site 1143 coring summary. (See table note. Continued on next page.)

			Depth			Length (cm)		
Core	Date (March 1999)	Time (UTC + 8 hr)	Top (mbsf)	Bottom (mbsf)	Top (mcd)	Cored	Recovered	Recovery (%)
184-1143A-								
1H	4	0350	0.0	2.9	0.02	2.9	2.89	99.7
2H	4	0440	2.9	12.4	3.32	9.5	9.91	104.3
3H	4	0530	12.4	21.9	13.50	9.5	9.92	104.4
4H	4	0700	21.9	31.4	24.04	9.5	10.01	105.4
5H	4	0750	31.4	40.9	33.94	9.5	9.85	103.7
6H	4	0830	40.9	50.4	43.66	9.5	10.08	106.1
7H	4	1005	50.4	59.9	53.82	9.5	9.59	101.0
8H	4	1055	59.9	69.4	63.60	9.5	9.97	105.0
9H	4	1135	69.4	78.9	73.50	9.5	9.81	103.3
10H	4	1215	78.9	88.4	83.54	9.5	9.99	105.2
11H	4	1335	88.4	97.9	93.64	9.5	9.93	104.5
12H	4	1450	97.9	107.4	103.08	9.5	9.95	104.7
13H	4	1540	107.4	116.9	113.04	9.5	9.72	102.3
14H	4	1625	116.9	126.4	122.92	9.5	9.77	102.8
15H	4	1710	126.4	135.9	133.28	9.5	9.12	96.0
16H	4	1830	135.9	145.4	142.46	9.5	10.03	105.6
17H	4	1920	145.4	154.9	152.38	9.5	9.34	98.3
18H	4	2005	154.9	164.4	162.42	9.5	9.52	100.2
19H	4	2100	164.4	173.9	171.57	9.5	9.23	97.2
20H	4	2140	173.9	183.4	181.75	9.5	9.12	95.8
21H	4	2230	183.4	190.4	193.52	7.0	7.08	101.1
22X	5	0010	190.4	198.0	201.10	7.6	7.22	95.0
23X	5	0050	198.0	202.0	208.50	4.0	4.49	112.3
24X	5	0135	202.0	211.6	212.44	9.6	9.72	101.3
25X	5	0225	211.6	221.2	220.32	9.6	3.78	39.4
26X	5	0315	221.2	230.8	231.36	9.6	9.72	101.3
27X	5	0425	230.8	240.4	240.58	9.6	3.44	35.8
28X	5	0555	240.4	250.0	250.72	9.6	8.61	89.7
29X	5	0710	250.0	259.6	259.42	9.6	9.67	100.7
30X	5	0800	259.6	269.2	269.54	9.6	9.66	100.6
31X	5	0920	269.2	278.9	279.32	9.7	9.76	100.6
32X	5	1010	278.9	288.5	289.24	9.6	9.81	102.2
33X	5	1100	288.5	298.1	299.16	9.6	9.63	100.3
34X	5	1230	298.1	307.7	308.76	9.6	8.79	91.6
35X	5	1325	307.7	317.3	317.74	9.6	9.65	100.5
36X	5	1415	317.3	326.9	327.96	9.6	9.62	100.2
37X	5	1520	326.9	336.4	337.82	9.5	9.81	103.3
38X	5	1610	336.4	346.1	347.98	9.7	9.45	97.42
39X	5	1705	346.1	355.7	357.68	9.6	8.97	93.4
40X	5	1800	355.7	364.9	367.02	9.2	7.59	83.6
41X	5	1855	364.9	374.5	376.48	9.6	9.02	94.0
42X	5	1945	374.5	384.2	388.54	9.7	7.79	80.3
43X	5	2055	384.2	393.9	384.20	9.7	0.19	2.0
44X	5	2215	393.9	400.0	406.96	6.1	6.66	109.2
					Totals:	400.0	377.88	94.6
184-1143B-								
1H	7	0145	0.0	5.4	0.00	5.4	5.40	100.0
2H	7	0225	5.4	14.9	7.52	9.5	9.64	101.5
3H	7	0345	14.9	24.4	17.62	9.5	9.96	104.8
4H	7	0435	24.4	33.9	27.92	9.5	9.60	101.0
5H	7	0515	33.9	43.4	38.14	9.5	9.75	102.6
6H	7	0555	43.4	52.9	48.00	9.5	9.70	102.1
7H	7	0635	52.9	62.4	58.46	9.5	9.53	100.3
8H	7	0715	62.4	71.9	68.22	9.5	9.86	103.8
9H	7	0800	71.9	81.4	78.48	9.5	9.88	104.0
10H	7	0840	81.4	90.9	88.28	9.5	9.93	104.5
11H	7	0920	90.9	100.4	98.00	9.5	9.77	102.8
12H	7	1005	100.4	109.9	107.86	9.5	9.89	104.1
13H	7	1045	109.9	119.4	117.70	9.5	8.81	92.7
14H	7	1125	119.4	128.9	127.60	9.5	9.67	101.8
15H	7	1205	128.9	138.4	137.22	9.5	9.46	99.6
16H	7	1250	138.4	147.9	146.94	9.5	9.81	103.3
17H	7	1335	147.9	157.4	156.72	9.5	9.71	102.2
18H	7	1420	157.4	166.9	165.69	9.5	9.89	104.1
19H	7	1510	166.9	175.4	175.97	8.5	8.39	98.7

Table T1 (continued).

Core	Date (March 1999)	Time (UTC + 8 hr)	Depth			Length (cm)		Recovery (%)
			Top (mbsf)	Bottom (mbsf)	Top (mcd)	Cored	Recovered	
20X	7	1610	175.4	181.1	184.27	5.7	6.88	120.7
21X	7	1655	181.1	190.7	191.80	9.6	9.76	101.7
22X	7	1755	190.7	200.3	202.36	9.6	5.69	59.3
23X	7	1850	200.3	209.9	210.84	9.6	7.82	81.5
24X	7	1935	209.9	219.5	220.66	9.6	4.65	48.4
25X	7	2030	219.5	229.2	230.70	9.7	8.14	83.9
26X	7	2125	229.2	238.9	240.68	9.7	6.91	71.2
27X	7	2210	238.9	248.6	250.60	9.7	9.84	101.4
28X	7	2255	248.6	258.2	259.48	9.6	8.03	83.6
					Totals:	258.2	246.37	95.4
184-1143C-								
1H	8	0115	0.0	9.4	3.20	9.4	9.33	99.3
2H	8	0150	9.4	18.9	12.80	9.5	9.97	105.0
3H	8	0240	18.9	28.4	22.86	9.5	10.00	105.3
4H	8	0325	28.4	34.9	30.06	6.5	9.52	146.5
5H	8	0410	34.9	44.4	40.06	9.5	10.05	105.8
6H	8	0445	44.4	53.9	49.86	9.5	10.02	105.5
7H	8	0530	53.9	63.4	60.16	9.5	9.98	105.1
8H	8	0620	63.4	72.9	70.24	9.5	10.10	106.3
9H	8	0700	72.9	82.4	80.28	9.5	9.92	104.4
10H	8	0745	82.4	91.9	89.92	9.5	9.82	103.4
11H	8	0825	91.9	101.4	99.68	9.5	9.76	102.7
12H	8	0915	101.4	110.9	109.34	9.5	9.95	104.7
13H	8	1010	110.9	120.4	119.06	9.5	9.85	103.7
14H	8	1055	120.4	129.9	129.06	9.5	10.03	105.6
15H	8	1135	129.9	139.4	138.24	9.5	9.57	100.7
16H	8	1220	139.4	148.9	148.98	9.5	9.82	103.4
17H	8	1305	148.9	158.4	158.80	9.5	9.36	98.5
18H	8	1345	158.4	167.9	167.79	9.5	9.78	103.0
19H	8	1430	167.9	177.4	178.19	9.5	9.07	95.5
20X	8	1545	177.4	180.1	187.19	2.7	3.69	136.7
21X	8	1630	180.1	189.7	192.50	9.6	9.91	103.2
22X	8	1715	189.7	199.3	202.10	9.6	9.76	101.7
23X	8	1805	199.3	208.9	211.70	9.6	9.79	102.0
24X	8	1845	208.9	218.5	221.30	9.6	9.87	102.8
25X	8	1925	218.5	228.1	230.90	9.6	9.86	102.7
26X	8	2010	228.1	237.7	240.50	9.6	5.43	56.6
27X	8	2105	237.7	247.3	250.10	9.6	9.76	101.7
28X	8	2150	247.3	257.0	259.70	9.7	9.83	101.3
29X	8	2245	257.0	266.7	269.40	9.7	9.80	101.0
30X	9	2330	266.7	276.4	279.10	9.7	9.80	101.0
31X	9	0020	276.4	286.1	288.80	9.7	9.78	100.8
32X	9	0120	286.1	295.7	298.50	9.6	8.49	88.4
33X	9	0210	295.7	305.3	308.10	9.6	7.03	73.2
34X	9	0305	305.3	314.9	317.70	9.6	6.61	68.9
35X	9	0355	314.9	324.5	327.30	9.6	7.52	78.3
36X	9	0450	324.5	334.1	336.90	9.6	9.17	95.5
37X	9	0610	334.1	343.7	346.50	9.6	4.39	45.7
38X	9	0710	343.7	353.3	356.10	9.6	4.76	49.6
39X	9	0820	353.3	362.8	365.70	9.5	9.05	95.3
40X	9	0930	362.8	372.4	375.20	9.6	8.08	84.2
41X	9	1035	372.4	381.7	384.80	9.3	9.05	97.3
42X	9	1135	381.7	391.3	394.10	9.6	9.72	101.3
43X	9	1300	391.3	401.0	403.70	9.7	8.33	85.9
44X	9	1400	401.0	410.7	413.40	9.7	9.27	95.6
45X	9	1520	410.7	420.3	423.10	9.6	9.75	101.6
46X	9	1610	420.3	429.9	432.70	9.6	7.66	79.8
47X	9	1655	429.9	439.5	442.30	9.6	9.86	102.7
48X	9	1750	439.5	449.2	451.90	9.7	8.68	89.5
49X	9	1840	449.2	458.9	461.60	9.7	9.04	93.2
50X	9	1940	458.9	468.5	471.30	9.6	8.76	91.3
51X	9	2045	468.5	478.2	480.90	9.7	7.92	81.7
52X	9	2140	478.2	487.9	490.60	9.7	9.22	95.1
53X	9	2230	487.9	497.6	500.30	9.7	9.09	93.7
54X	9	2315	497.6	500.0	510.00	2.4	2.91	121.3
					Totals:	500.0	477.54	95.5

Note: UTC = Universal Time Coordinated. This table is also available in **ASCII format.**

Table T2. Site 1143 coring summary by section.

Core	Date (March 1999)	Time (UTC + 8 hr)	Core depth (mbsf)		Length (m)		Recovery (%)	Section	Length (m)		Section depth (mbsf)		Top depth (mcd)	Catwalk samples	Comments
			Top	Bottom	Cored	Recovered			Liner	Curated	Top	Bottom			
184-1143A-															
1H	4	0350	0.0	2.9	2.9	2.89	99.7								
								1	1.50	1.50	0.00	1.50	0.02	IW, IWPL	
								2	1.21	1.21	1.50	2.71	1.52	HS	
								CC(w/2)	0.18	0.18	2.71	2.89	2.73	PAL	
								Totals:	2.89	2.89					
2H	4	0440	2.9	12.4	9.5	9.91	104.3								
								1	1.50	1.50	2.90	4.40	3.32		
								2	1.50	1.50	4.40	5.90	4.82		
								3	1.50	1.50	5.90	7.40	6.32	IW, IWPL	
								4	1.50	1.50	7.40	8.90	7.82	HS	
								5	1.50	1.50	8.90	10.40	9.32		
								6	1.50	1.50	10.40	11.90	10.82		
								7	0.70	0.70	11.90	12.60	12.32		
								CC(w/7)	0.21	0.21	12.60	12.81	13.02	PAL	
								Totals:	9.91	9.91					
3H	4	0530	12.4	21.9	9.5	9.92	104.4								
								1	1.50	1.50	12.40	13.90	13.50		
								2	1.50	1.50	13.90	15.40	15.00		
								3	1.50	1.50	15.40	16.90	16.50	IW, IWPL	
								4	1.50	1.50	16.90	18.40	18.00	HS	
								5	1.50	1.50	18.40	19.90	19.50		
								6	1.50	1.50	19.90	21.40	21.00		
								7	0.72	0.72	21.40	22.12	22.50		
								CC(w/7)	0.20	0.20	22.12	22.32	23.22	PAL	
								Totals:	9.92	9.92					
4H	4	0700	21.9	31.4	9.5	10.01	105.4								Oriented; Adara
								1	1.50	1.50	21.90	23.40	24.04		
								2	1.50	1.50	23.40	24.90	25.54		
								3	1.50	1.50	24.90	26.40	27.04	IW, IWPL	
								4	1.50	1.50	26.40	27.90	28.54	HS	
								5	1.50	1.50	27.90	29.40	30.04		
								6	1.50	1.50	29.40	30.90	31.54		
								7	0.70	0.70	30.90	31.60	33.04		
								CC(w/7)	0.31	0.31	31.60	31.91	33.74	PAL	
								Totals:	10.01	10.01					
5H	4	0750	31.4	40.9	9.5	9.85	103.7								Oriented
								1	1.50	1.50	31.40	32.90	33.94		
								2	1.50	1.50	32.90	34.40	35.44		
								3	1.50	1.50	34.40	35.90	36.94	IW, IWPL	
								4	1.50	1.50	35.90	37.40	38.44	HS	
								5	1.50	1.50	37.40	38.90	39.94		

Notes: UTC = Universal Time Coordinated. The notation “CC(w/x)” refers to the D-tube in which the core catcher is stored, where x is the section number (1–7 or CC). NS = no section, IW = interstitial waters, IWPL = interstitial waters plastic Lin, HS = headspace, PAL = paleontology, SOLH = Solheid. Only a portion of this table appears here. The complete table is available in **ASCII format.**

Table T3. Site 1143 composite depths.

Core	Depth (mbsf)	Cumulative offset (m)	Depth (mcd)
184-1143A-			
1H	0.0	0.02	0.02
2H	2.9	0.42	3.32
3H	12.4	1.10	13.50
4H	21.9	2.14	24.04
5H	31.4	2.54	33.94
6H	40.9	2.76	43.66
7H	50.4	3.42	53.82
8H	59.9	3.70	63.60
9H	69.4	4.10	73.50
10H	78.9	4.64	83.54
11H	88.4	5.24	93.64
12H	97.9	5.18	103.08
13H	107.4	5.64	113.04
14H	116.9	6.02	122.92
15H	126.4	6.88	133.28
16H	135.9	6.56	142.46
17H	145.4	6.98	152.38
18H	154.9	7.52	162.42
19H	164.4	7.17	171.57
20H	173.9	7.85	181.75
21H	183.4	10.12	193.52
22X	190.4	10.70	201.10
23X	198.0	10.50	208.50
24X	202.0	10.44	212.44
25X	211.6	8.72	220.32
26X	221.2	10.16	231.36
27X	230.8	9.78	240.58
28X	240.4	10.32	250.72
29X	250.0	9.42	259.42
30X	259.6	9.94	269.54
31X	269.2	10.12	279.32
32X	278.9	10.34	289.24
33X	288.5	10.66	299.16
34X	298.1	10.66	308.76
35X	307.7	10.04	317.74
36X	317.3	10.66	327.96
37X	326.9	10.92	337.82
38X	336.4	11.58	347.98
39X	346.1	11.58	357.68
40X	355.7	11.32	367.02
41X	364.9	11.58	376.48
42X	374.5	14.04	388.54
43X	384.2	14.04	398.24
44X	393.9	13.06	406.96
184-1143B-			
1H	0.0	0.00	0.00
2H	5.4	2.12	7.52
3H	14.9	2.72	17.62
4H	24.4	3.52	27.92
5H	33.9	4.24	38.14
6H	43.4	4.60	48.00
7H	52.9	5.56	58.46
8H	62.4	5.82	68.22
9H	71.9	6.58	78.48
10H	81.4	6.88	88.28
11H	90.9	7.10	98.00
12H	100.4	7.46	107.86
13H	109.9	7.80	117.70
14H	119.4	8.20	127.60
15H	128.9	8.32	137.22
16H	138.4	8.54	146.94
17H	147.9	8.82	156.72
18H	157.4	8.29	165.69
19H	166.9	9.07	175.97
20X	175.4	8.87	184.27
21X	181.1	10.09	191.19
22X	190.7	11.66	202.36
23X	200.3	10.54	210.84
24X	209.9	10.76	220.66
25X	219.5	11.20	230.70
26X	229.2	11.48	240.68
27X	238.9	11.70	250.60
28X	248.6	10.88	259.48
184-1143C-			
1H	0.0	3.20	3.20
2H	9.4	3.40	12.80
3H	18.9	3.96	22.86
4H	28.4	1.66	30.06
5H	34.9	5.16	40.06
6H	44.4	5.46	49.86
7H	53.9	6.26	60.16
8H	63.4	6.84	70.24
9H	72.9	7.38	80.28
10H	82.4	7.52	89.92
11H	91.9	7.78	99.68
12H	101.4	7.94	109.34
13H	110.9	8.16	119.06
14H	120.4	8.66	129.06
15H	129.9	8.34	138.24
16H	139.4	9.58	148.98
17H	148.9	9.90	158.80
18H	158.4	9.39	167.79
19H	167.9	10.29	178.19
20X	177.4	9.79	187.19
21X	180.1	12.40	192.50
22X	189.7	12.40	202.10
23X	199.3	12.40	211.70
24X	208.9	12.40	221.30
25X	218.5	12.40	230.90
26X	228.1	12.40	240.50
27X	237.7	12.40	250.10
28X	247.3	12.40	259.70
29X	257.0	12.40	269.40
30X	266.7	12.40	279.10
31X	276.4	12.40	288.80
32X	286.1	12.40	298.50
33X	295.7	12.40	308.10
34X	305.3	12.40	317.70
35X	314.9	12.40	327.30
36X	324.5	12.40	336.90
37X	334.1	12.40	346.50
38X	343.7	12.40	356.10
39X	353.3	12.40	365.70
40X	362.8	12.40	375.20
41X	372.4	12.40	384.80
42X	381.7	12.40	394.10
43X	391.3	12.40	403.70
44X	401.0	12.40	413.40
45X	410.7	12.40	423.10
46X	420.3	12.40	432.70
47X	429.9	12.40	442.30
48X	439.5	12.40	451.90
49X	449.2	12.40	461.60
50X	458.9	12.40	471.30
51X	468.5	12.40	480.90
52X	478.2	12.40	490.60
53X	487.9	12.40	500.30
54X	497.6	12.40	510.00

Note: This table is also available in **ASCII format.**

Table T4. Site 1143 splice tie points.

Hole, core, section, interval (cm)	Depth			Hole, core, section, interval (cm)	Depth	
	(mbsf)	(mcd)			(mbsf)	(mcd)
184-				184-		
1043B-1H-3, 40	3.40	3.40	Tie to	1043C-1H-1, 20	0.20	3.40
1043C-1H-6, 112	8.62	11.82	Tie to	1043B-2H-3, 130	9.70	11.82
1043B-2H-6, 140	14.30	16.42	Tie to	1043C-2H-3, 61	13.02	16.42
1043C-2H-7, 32	18.72	22.12	Tie to	1043B-3H-3, 150	19.40	22.12
1043B-3H-7, 10	24.00	26.72	Tie to	1043C-3H-3, 85	22.76	26.72
1043C-3H-6, 108	27.48	31.44	Tie to	1043C-4H-1, 137	29.78	31.44
1043C-4H-6, 112	37.02	38.68	Tie to	1043B-5H-1, 54	34.44	38.68
1043B-5H-6, 114	42.54	46.78	Tie to	1043C-5H-5, 72	41.62	46.78
1043C-5H-7, 78	44.68	49.84	Append to	1043C-6H-1, 0	44.40	49.86
1043C-6H-7, 20	53.60	59.06	Tie to	1043B-7H-1, 60	53.50	59.06
1043B-7H-5, 52	59.42	64.98	Tie to	1043C-7H-4, 32	58.72	64.98
1043C-7H-6, 72	62.12	68.38	Tie to	1043B-8H-1, 16	62.56	68.38
1043B-8H-6, 48	70.38	76.20	Tie to	1043C-8H-4, 146	69.36	76.20
1043C-8H-7, 20	72.60	79.44	Tie to	1043B-9H-1, 96	72.86	79.44
1043B-9H-7, 36	81.26	87.84	Tie to	1043C-9H-6, 5	80.46	87.84
1043C-9H-7, 66	82.56	89.94	Append to	1043C-10H-1, 0	82.40	89.92
1043C-10H-6, 80	90.70	98.22	Tie to	1043B-11H-1, 21	91.12	98.22
1043B-11H-5, 100	97.90	105.00	Tie to	1043C-11H-4, 101	97.22	105.00
1043C-11H-7, 48	101.18	108.96	Tie to	1043B-12H-1, 109	101.50	108.96
1043B-12H-5, 28	106.68	114.14	Tie to	1043C-12H-4, 29	106.20	114.14
1043C-12H-7, 36	110.76	118.70	Tie to	1043B-13H-1, 98	110.90	118.70
1043B-13H-6, 116	118.56	126.36	Tie to	1043A-14H-3, 44	120.34	126.36
1043A-14H-5, 66	123.56	129.58	Tie to	1043C-14H-1, 52	120.92	129.58
1043C-14H-7, 8	129.48	138.14	Tie to	1043B-15H-1, 92	129.82	138.14
1043B-15H-5, 28	135.18	143.50	Tie to	1043C-15H-4, 76	135.16	143.50
1043C-15H-6, 70	138.10	146.44	Tie to	1043A-16H-3, 97	139.88	146.44
1043A-16H-5, 80	142.70	149.26	Tie to	1043C-16H-1, 27	139.68	149.26
1043C-16H-6, 92	147.82	157.40	Tie to	1043B-17H-1, 66	148.58	157.40
1043B-17H-6, 20	155.60	164.42	Tie to	1043C-17H-4, 112	154.52	164.42
1043C-17H-6, 76	157.16	167.06	Tie to	1043A-18H-4, 24	159.54	167.06
1043A-18H-7, 24	164.07	171.59	Tie to	1043B-18H-5, 29	163.30	171.59
1043B-18H-7, 12	166.12	174.41	Tie to	1043C-18H-5, 61	165.02	174.41
1043C-18H-6, 132	167.22	176.61	Tie to	1043B-19H-1, 62	167.54	176.61
1043B-19H-5, 92	173.82	182.89	Tie to	1043C-19H-4, 20	172.60	182.89
1043C-19H-5, 128	175.18	185.47	Tie to	1043B-20X-1, 120	176.60	185.47
1043B-20X-5, 58	181.98	190.85				

Note: This table is also available in **ASCII format.**

Table T5. Volcanic ash layers recovered at Site 1143.

Hole 1143A			Hole 1143B			Hole 1143C				
Core, section, interval (cm)	Top (mbsf)	Top (mcd)	Core, section, interval (cm)	Top (mbsf)	Top (mcd)	Core, section, interval (cm)	Top (mbsf)	Top (mcd)	Thickness (cm)	Description
2H-2, 73	5.13	5.55	NO			NO			1-2	Light gray, intensely bioturbated volcanic ash
5H-6, 121-123	40.11	42.65	5H-4, 4-6	38.44	42.68	NO			1-2	Light gray, intensely bioturbated volcanic ash
NO			NO			6H-6, 24-24	52.14	57.60	0-1	Discontinuous ash (filled burrow?)
8H-CC, 2-4	69.67	73.37	8H-4, 17-25	67.07	72.89	8H-2, 121-125	66.11	72.95	2-8	Dark gray, bioturbated volcanic ash
9H-3, 114-118	73.54	77.64	8H-7, 41 to 8H-CC, 3	71.81	77.63	8H-5, 148, to 8H-6, 3	70.88	77.72	4-9	Dark gray ash, sharp basal contact
NO			NO			8H-6, 138-139	72.28	79.12	0-1	Dark gray, thin, discontinuous, intensely bioturbated ash
NO			NO			9H-6, 132	81.72	89.10	0-1	Dark gray, discontinuous ash
10H-2, 104	81.44	86.08	NO			NO			0-1	Foraminifer sand with tephra particles
20H-4, 94-97	179.34	187.19	20X-2, 134-138	178.24	187.11	19H-7, 11-22	176.61	186.90	3-11	Dark gray, graded, sharp basal contact
NO			25X-2, 68-75	221.68	232.88	NO			>1	Dark gray, foraminifer tests, and angular quartz
NO			NO			25X-4, 104-105	224.04	236.44	>1	Dark gray, foraminifer tests, and angular quartz
NO						31X-6, 15	284.05	296.45	0-1	Black discontinuous ash
						45X-7, 30, to 45X-CC, 9	420.00	432.40	14	Dark gray, graded clay with quartz
						47X-5, 33-37	436.23	448.63	4	Breccia
						47X-6, 98-101	438.38	450.78	3	Breccia
						49X-CC, 7-27	457.84	470.24	>20	Dark gray
						53X-3, 10-17	491.00	503.40	7	Black

Note: NO = not observed.

Table T6. Turbidite deposits recovered at Site 1143. (See table notes. Continued on next two pages.)

Core, section, interval (cm)	Depth				Thickness (cm)	Bouma divisions recognized
	Top		Bottom			
	(mbsf)	(mcd)	(mbsf)	(mcd)		
184-1143A-						
5H-3, 94-105	35.34	37.88	35.45	37.99	11	A
6H-2, 62-82	43.02	45.78	43.22	45.98	20	A
10H-2, 103-104	81.43	86.07	81.44	86.08	1	A with volcanic ash
11H-4, 62-78	93.52	98.76	93.68	98.92	16	E
17H-2, 150	148.40	155.38	148.40	155.38	<0.5	?
24X-1, 108-111	203.08	213.52	203.11	213.55	3	A
25X-2, 80-85	213.90	222.62	213.95	222.67	5	A
26X-1, 27-36	221.47	231.63	221.56	231.72	9	A
26X-2, 43-47	223.13	233.29	223.17	233.33	4	A
26X-2, 55-60	223.25	233.41	223.30	233.46	5	A
26X-4, 66-69	226.36	236.52	226.39	236.55	3	A
26X-4, 86-89	226.56	236.72	226.59	236.75	3	A
27X-3, 44-94	233.74	243.52	234.20	244.00	50	E
28X-4, 100-118	245.90	256.22	246.08	256.40	18	AE
29X-3, 101-146	254.01	263.43	254.46	263.88	45	E
32X-1, 0-85	278.90	289.24	281.25	291.59	235	AE
33X-6, 50-85	296.50	307.16	296.85	307.51	35	B
34X-4, 120-150	303.80	314.46	304.10	314.76	30	BC
35X-6, 134	316.54	326.58			55	ABC
35X-CC, 14			317.09	327.13		
36X-1, 0	317.30	327.96			500	Slumping
36X-4, 50			322.30	332.96		
36X-6, 42-69	325.22	335.88	325.49	336.15	27	A in slumping
37X-1, 110-132	328.00	338.92	328.22	339.14	22	A in slumping
37X-2, 89-97	329.29	340.21	329.37	340.29	8	A in slumping
37X-3, 25	330.15	341.07			656	ABCE
37X-CC, 37			336.71	347.63		
38X-1, 0-38	336.40	347.98	336.78	348.36	38	A
40X-1, 17-31	355.87	367.19	356.01	367.33	14	A
40X-1, 31-67	356.01	367.33	356.37	367.69	36	AC
40X-4, 135-137	361.55	372.87	361.57	372.89	2	A
41X-3, 130	369.20	380.78			60	ABCDE
41X-4, 40			369.80	381.38		
42X-1, 54-58	375.04	389.08	375.18	389.22	14	Slumping
44X-2, 109-132	396.49	409.55	396.72	409.78	23	ABE
44X-4, 80-85	399.20	412.26	399.25	412.31	15	ABE
44X-5, 63-70	400.03	413.09	400.10	413.16	7	ABE
184-1143B-						
5H-6, 23-37	41.63	45.87	41.77	46.01	14	A
15H-3, 107	132.97	141.29	132.97	141.29	<1	A
23X-1, 139-141	201.69	212.23	201.71	212.25	2	A
24X-2, 31-33	211.71	222.47	211.73	222.49	2	Fine grained with quartz
26X-2, 137	232.07	243.55			205	AE
26X-4, 42			234.12	245.60		
28X-3, 97-143	252.57	263.45	253.03	263.91	46	E
184-1143C-						
4H-6, 18-26	36.08	37.74	36.16	37.82	8	A
5H-3, 143-150	39.33	44.49	39.40	44.56	7	A
16H-5, 49-50	145.89	155.47	145.90	155.48	1	A
21X-7, 0-2	189.10	201.50	189.12	201.52	2	A
23X-1, 127-130	200.57	212.97	200.60	213.00	3	A
24X-4, 68-70	214.08	226.48	214.10	226.50	2	A
25X-2, 35-41	220.35	232.75	220.41	232.81	6	A
25X-2, 67-73	220.67	233.07	220.73	233.13	6	A
26X-3, 0	231.10	243.50			196	AE
26X-4, 56			233.16	245.56		
27X-2, 112-117	240.32	252.72	240.37	252.77	5	A
27X-5, 17-36	243.87	256.27	244.06	256.46	19	E
28X-3, 128	251.58	263.98			53	AE
28X-4, 31			252.11	264.51		
31X-1, 60	277.00	289.40			109	CE
31X-2, 19			278.09	290.49		
31X-2, 19-116	278.09	290.49	279.06	291.46	97	CE
33X-3, 144	300.14	312.54			20	AE

Table T6 (continued).

Core, section, interval (cm)	Depth				Thickness (cm)	Bouma divisions recognized
	Top		Bottom			
	(mbsf)	(mcd)	(mbsf)	(mcd)		
33X-4, 14			300.34	312.74		
34X-CC, 16-30	311.61	324.01	311.75	324.15	14	E
35X-1, 0-150	314.90	327.30	316.40	328.80	150	Slumping
36X-1, 104-107	325.54	337.94	325.57	337.97	3	A
36X-2, 64-73	326.64	339.04	326.73	339.13	9	A
36X-2, 127-130	327.27	339.67	327.30	339.70	3	A
36X-5, 130	331.80	344.20			187	BE
36X-7, 20			333.70	346.10		
37X-1, 0	334.10	346.50			179	B
37X-2, 29			335.89	348.29		
39X-2, 5-28	354.85	367.25	355.08	367.48	23	AB
39X-5, 125-127	360.55	372.95	360.57	372.97	2	AB
40X-3, 143-148	367.23	379.63	367.28	379.68	5	A
41X-1, 5-45	372.45	384.85	372.85	385.25	40	Slumping
41X-2, 0	373.90	386.30			320	Slumping
41X-4, 20			377.10	389.50		
41X-5, 0-25	378.40	390.80	378.65	391.05	25	Slumping
41X-6, 0-27	379.90	392.30	380.17	392.57	27	Slumping
42X-1, 0-51	381.70	394.10	382.21	394.61	51	BE
43X-4, 130	397.10	409.50			24	AB
43X-5, 4			397.34	409.74		
44X-2, 111-131	403.61	416.01	403.81	416.21	20	AE
44X-4, 100-131	406.50	418.90	406.81	419.21	31	ABE
44X-5, 128-130	408.28	420.68	408.30	420.70	2	B
44X-5, 140-143	408.40	420.80	408.43	420.83	3	B
45X-1, 24-57	410.94	423.34	411.27	423.67	33	AB
45X-1, 86-91	411.56	423.96	411.61	424.01	5	B
45X-3, 43-47	414.13	426.53	414.17	426.57	4	B
45X-3, 57-59	414.27	426.67	414.29	426.69	2	A
45X-4, 25-35	415.45	427.85	415.55	427.95	10	B
45X-5, 45-60	417.15	429.55	417.30	429.70	15	AE
46X-1, 0-70	420.30	432.70	421.00	433.40	70	B
46X-2, 39-46	422.19	434.59	422.26	434.66	7	B
46X-2, 50-55	422.30	434.70	422.35	434.75	5	B
46X-2, 103-105	422.83	435.23	422.85	435.25	2	A
46X-3, 53-55	423.83	436.23	423.85	436.25	2	A
46X-4, 15-18	424.95	437.35	424.98	437.38	3	B
46X-5, 24-27	426.54	438.94	426.57	438.97	3	B
46X-5, 76-90	427.06	439.46	427.20	439.60	14	AB
46X-5, 90-104	427.20	439.60	427.34	439.74	14	Biosiliceous laminated
47X-3, 70-83	433.60	446.00	433.73	446.13	13	Biosiliceous laminated
47X-4, 80-100	435.20	447.60	435.40	447.80	20	Biosiliceous laminated
47X-6, 81-84	438.21	450.61	438.24	450.64	3	Biosiliceous laminated
47X-7, 11-14	439.01	451.41	439.04	451.44	3	Biosiliceous laminated
48X-1, 107-117	440.57	452.97	440.67	453.07	10	B
48X-2, 125-131	442.25	454.65	442.31	454.71	6	B
48X-3, 84-87	443.34	455.74	443.37	455.77	3	B
48X-5, 114-120	446.64	459.04	446.70	459.10	6	A
48X-6, 21-22	447.17	459.57	447.18	459.58	1	Biosiliceous laminated
48X-6, 35-36	447.31	459.71	447.32	459.72	1	A
48X-6, 71-72	447.67	460.07	447.68	460.08	1	Biosiliceous laminated
49X-1, 128-131	450.48	462.88	450.51	462.91	3	B
49X-2, 120	451.90	464.30			70	BCE
49X-3, 40			452.60	465.00		
49X-5, 17-24	455.37	467.77	455.44	467.84	7	BC
49X-5, 135-139	456.55	468.95	456.59	468.99	4	Pyrite silt
50X-1, 39-42	459.29	471.69	459.32	471.72	3	B
50X-1, 115-123	460.05	472.45	460.13	472.53	8	B
50X-2, 53-60	460.93	473.33	461.00	473.40	7	B
50X-2, 74-100	461.14	473.54	461.40	473.80	26	A
50X-6, 30-34	466.70	479.10	466.74	479.14	4	A
51X-1, 123-127	469.73	482.13	469.77	482.17	4	C
51X-4, 73	473.73	486.13			101	AE
51X-5, 24			474.74	487.14		
52X-2, 142	481.12	493.52			33	BC
52X-3, 25			481.45	493.85		
52X-5, 25-113	484.45	496.85	485.33	497.73	88	CE
52X-6, 38-42	486.08	498.48	486.12	498.52	4	A
52X-6, 102-106	486.72	499.12	486.76	499.16	4	BC
53X-2, 84-87	490.24	502.64	490.27	502.67	3	B

Table T6 (continued).

Core, section, interval (cm)	Depth Top (mbsf)	Depth Top (mcd)	Depth Bottom (mbsf)	Depth Bottom (mcd)	Thickness (cm)	Bouma divisions recognized
53X-4, 48-54	492.88	505.28	492.94	505.34	6	B
53X-5, 47-53	494.37	506.77	494.43	506.83	6	B
53X-5, 112-120	495.02	507.42	495.10	507.50	8	B
53X-6, 83-84	496.23	508.63	496.24	508.64	1	C
54X-1, 108-117	498.68	511.08	498.77	511.17	9	AC
54X-2, 40-54	499.50	511.90	499.64	512.04	14	BC

Notes: Bouma divisions: A = massive/graded bedding, B = plane parallel bedding, C = convolute or ripple bedding, D = parallel bedding, E = interturbidite (hemipelagic/pelagic sediments), ? = Bouma division not identified. Bouma divisions D and E were difficult to distinguish. Intervals labeled E may be division D.

Table T7. Summary of biohorizons at Site 1143.

		Depth range of stratigraphic datums								
		Top			Bottom					
Code	Events	Core, section, interval (cm)	Depth (mbsf)	Depth (mcd)	Core, section, interval (cm)	Depth (mbsf)	Depth (mcd)	Age (Ma)	Average depth (mcd)	Average sedimentation rate (m/m.y.)
		184-1143A-			184-1143A-					
CN	FO *E. huxleyi* acme	1H-CC, 11-18	2.86	**2.88**	2H-CC, 14-21	12.78	13.20	0.09	8.04	54
PF	LO pink *G. ruber*	1H-CC, 11-18	2.86	2.88	2H-CC, 14-21	12.78	**13.20**	0.12	8.04	
CN	FO *E. huxleyi*	3H-1, 65-67	13.05	**14.15**	3H-2, 65-67	14.57	15.67	0.26	14.91	
PF	FO pink *G. ruber*	3H-CC, 3-10	22.32	**23.42**	4H-CC, 24-31	31.91	34.33	0.40	28.875	
CN	LO *P. lacunosa*	4H-2, 65-67	24.70	26.84	4H-3, 65-67	25.55	**27.69**	0.46	27.27	
BF	LO *Stilostomella*	5H-CC, 19-26	41.22	43.76	6H-CC, 27-34	50.95	**53.71**	0.75	48.74	
CN	LO small *Gephyrocapsa* acme	6H-6, 65-67	49.07	51.33	6H-7, 65-67	50.55	**53.31**	1.01	52.32	
CN	LO *C. macintyrei*	8H-CC, 20-27	69.84	73.54	9H-1, 65-67	70.05	**74.15**	1.59	73.85	
CN	FO medium *Gephyrocapsa* spp.*	10H-CC, 20-27	88.86	**93.50**	11H-1, 65-67	88.86	94.29	1.69	93.90	
PF	LO *G. fistulosus*	9H-CC, 23-30	79.18	83.28	10H-CC, 20-27	88.86	**93.50**	1.77	88.39	32
CN	LO *D. brouweri*	10H-CC, 20-27	88.86	93.50	11H-1, 65-67	89.05	**94.29**	1.96	93.90	
PF	FO *G. truncatulinoides*	10H-CC, 20-27	88.86	**93.50**	11H-CC, 40-47	98.30	103.54	2.00	98.52	
PF	LO *G. multicamerata*	10H-CC, 20-27	88.86	93.50	11H-CC, 40-47	98.30	**103.54**	2.4	98.52	
CN	LO *D. pentaradiatus*	12H-5, 65-67	104.57	109.75	12H-6, 65-67	106.05	**111.23**	2.52	110.49	
CN	LO *D. surculus*	13H-5, 65-67	114.07	119.71	13H-6, 65-67	115.55	**121.19**	2.53	120.45	
PF	FO *G. tosaensis*	15H-CC, 8-15	135.49	**142.37**	16H-CC, 38-45	145.90	**152.46**	**3.35**	147.42	
PF	FO *S. dehiscens*	14H-CC, 17-24	126.64	**132.66**	15H-CC, 8-15	135.49	142.37	3.25	137.52	
CN	LO *Sphenolithus abies/neoabies*	16H-CC, 38-45	145.90	152.46	17H-1, 60	146.00	**152.98**	3.66	152.52	
CN	LO *R. pseudoumbilicus*	17H-6, 60	153.50	160.48	17H-6, 80	153.70	**160.68**	3.82	160.58	
PF	*Pulleniatina* (S to D coiling change)	16H-CC, 38-45	145.90	152.46	17H-CC, 27-34	154.71	**161.69**	3.95	157.08	
CN	LO *A. tricorniculatus*	20H-4, 32	178.72	186.57	20H-4, 33	178.73	**186.58**	4	186.58	
CN	FCO *D. asymmetricus*	21H-2, 20-60	185.10	**195.22**	21H-2, 100	185.50	195.62	4.2	195.42	
PF	LO *G. nepenthes*	18H-CC, 52-59	164.36	171.88	19H-CC, 0-10	173.58	**180.75**	4.20	176.32	
PF	LO *S. kochi*	19H-CC, 0-10	173.58	180.75	20H-CC, 0-10	182.95	**190.80**	4.53	185.78	
CN	LO *C. acutus**	20H-CC, 0-10	182.95	190.80	21H-CC, 0-8	190.43	**200.55**	4.99	195.68	
CN	FO *C. acutus*	22X-CC, 43-50	197.57	**208.27**	23X-CC, 22-29	202.46	212.96	5.37	210.62	63
CN	LO *D. quinqueramus*	24X-6, 60	210.10	220.54	24X-6, 80	210.30	**220.74**	5.54	220.64	
PF	FO *G. tumida*	26X-CC, 41-48	230.87	**241.03**	27X-CC, 22-29	234.19	243.97	5.82	242.5	
CN	LO *A. amplificus*	26X-CC, 41-48	230.87	241.03	27X-CC, 22-29	234.19	**243.97**	5.99	242.5	
PF	FO *G. conglobatus*	29X-CC, 19-26	259.64	**269.06**	30X-CC, 27-32	269.23	279.17	6.20	274.12	
PF	FO *G. margaritae*	29X-CC, 19-26	259.64	**269.06**	30X-CC, 27-32	269.23	279.17	6.4	274.12	
CN	FO *A. amplificus*	31X-CC, 40-47	278.93	**289.05**	32X-CC, 35-42	288.68	299.02	6.76	294.04	
CN	FO *A. primus**	36X-CC, 40-47	326.89	**337.55**	37X-CC, 30-37	336.68	347.58	7.39	342.57	
		184-1143C-			184-1143C-					
CN	FO *D. berggrenii*	43X-CC, 48-54	400.97	**412.00**	44X-CC, 46-52	410.64	422.64	8.2	417.32	72
PF	FO *G. plesiotumida*	44X-CC, 46-52	410.64	**422.64**	45X-CC, 34-40	420.27	432.82	8.58	427.73	
PF	FO *G. extremus**	44X-CC, 46-52	410.64	**422.64**	45X-CC, 34-40	420.27	432.82	8.58	427.73	
PF	LO *G. mayeri*	49X-CC, 42-47	458.87	470.61	50X-CC, 27-33	468.47	**480.03**	10.49	475.32	
CN	FO *D. neohamatus*	51X-CC, 41-48	478.17	**488.79**	52X-CC, 44-49	487.87	499.79	9.60	494.29	

Notes: Sources of reference age for all biostratigraphic events are listed in Tables T2, p. 42, and T3, p. 43, in the "Explanatory Notes" chapter. CN = calcareous nannofossils, PF = planktonic foraminifers, BF = benthic foraminifers. FO = first occurrence, FCO = first common occurrence, LO = last occurrence. * = events used in calculating average sedimentation rate. Depth for the top and the bottom of biostratigraphic events = the mean of the sample interval. Depth in bold indicates where the marker species was observed highest or lowest in the studied samples; depth range between the top and bottom is the interval where the real bioevent may occur. Bars in average sedimentation rate column indicate the range of samples to which the average sedimentation applies.

Table T8. Calcareous nannofossil checklist for Site 1143. (See table notes. Continued on next page.)

Epoch	Zones		Core, section, interval (cm)	Depth (mcd)	Preservation	Abundance	*Amaurolithus amplificus*	*Amaurolithus delicatus*	*Amaurolithus ninae*	*Amaurolithus primus*	*Amaurolithus tricorniculatus*	*Calcidiscus leptoporus*	*Calcidiscus macintyrei*	*Catinaster coalitus*	*Ceratolithus acutus*	*Ceratolithus armatus*	*Ceratolithus cristatus*	*Ceratolithus rugosus*	*Coccolithus pelagicus*	*Discoaster asymmetricus*	*Discoaster berggrenii*	*Discoaster brouweri*	*Discoaster hamatus*	*Discoaster intercalaris*	*Discoaster loeblichii*	*Discoaster neohamatus*	*Discoaster neorectus*	*Discoaster pansus*	*Discoaster pentaradiatus*	*Discoaster quinqueramus*	*Discoaster surculus*	*Discoaster tamalis*	*Discoaster triradiatus*	*Discoaster variabilis*	*Emiliania huxleyi*	*Florisphaera profunda*	*Gephyrocapsa caribbeanica*	*Gephyrocapsa lumina*	*Gephyrocapsa margarelii*	*Gephyrocapsa oceanica*	*Gephyrocapsa* spp. (small)	*Helicosphaera carteri*	*Helicosphaera hyalina*	*Helicosphaera inversa*	*Helicosphaera sellii*	*Oolithotus antillarum*	*Pseudoemiliania lacunosa*	*Reticulofenestra asanoi*	*Reticulofenestra oamaruensis*	*Reticulofenestra pseudoumbilicus*	*Reticulofenestra umbilicus*	*Sphenolithus abies/neoabies*	*Sphenolithus belemnos*	*Sphenolithus ciperoensis*	*Sphenolithus heteromorphus*	*Thorosphaera flabellata*	*Triquetrorhabdulus rugosus*	*Umbellosphaera irregularis*	*Umbellosphaera tenuis*	*Umbilicosphaera sibogae*
			184-1143A-																																																										
Pleistocene	NN21b	CN15	1H-CC, 13-18	2.88	G	A						F					F																		A	D				A	C	F	R			R												R		R
	NN21a		2H-CC, 16-21	13.20	G	A						F					R																		C	D				C	C	R	R			R												F		F
			3H-CC, 15-20	23.39	G	A						R					R																		R	D	F	F		A	C	R	R	R														R		R
	NN19b	CN14a	4H-CC, 15-20	34.02	G	A						F					R																			D	F		F	A	C	F					F													R
			5H-CC, 21-26	43.76	G	A						F					R																			D	R		C	A	A	F		R			F									R				F
		CN13	6H-CC, 29-34	53.71	G	A						F					F																			D					A	F	R			R	C	R												F
			7H-CC, 12-17	63.38	G	A						C					R																			D	R		F	C	A	F				R	C											R		C
			8H-CC, 22-27	73.59	G	A						F					R																			A		C	R	C	A	F					C													
			9H-CC, 25-30	83.28	G	A						F					R																			A			C	C	D	F					C												R	F
	NN19a		10H-CC, 22-27	93.50	G	A						F	R				R																			A			F		A	R					C												R	R
late Pliocene	NN17/18	CN12c/d	11H-CC, 39-47	103.54	G	A						F	R				R					R							R							A					R	R			R		C													R
			12H-CC, 21-27	113.00	G	A						R	R				R					R							R			R	F			A						R			R		C													R
	NN16	CN12a/b	13H-CC, 18-25	122.73	G	A						R	R				R			R		C							C		R					A						R			R		C													R
			14H-CC, 20-24	132.66	G	A						R	R				R					C							C		R					A						R			R		C													
			15H-CC, 11-15	142.37	G	A						R	R				R					C							C		R		R			A						R			R		C													R
			16H-CC, 39-45	152.46	G	A						R	R				R					C							C		R		R			A						R			R		C													
early Pliocene	NN15	CN11	17H-7, 24-34	161.69	G	A						R	R				R			C		C							A		R		R			A						R			R		F			F										
			18H-7, 43-59	171.91	G	A						R	R				R	R				C							A		R			R		A						R			R		F			F										
			19H-CC, 0-10	180.77	G	A						R	R				R					C							A		R			R		A						R			R		R			R										
			20H-CC, 0-10	190.84	G	A		R			R	R	R				R					C							C		R			R		A						R			R					R										
	NN12-14	CN10	21H-CC, 0-8	200.57	G	A		R				R	R		R	R	R					C							C		R			R		A						R			R					R		A								
			22X-CC, 45-50	208.29	G	A						R	R		R	R						C							C		F			R		A						C										A								F
			23X-CC, 22-29	212.96	G	A		R				R	R		R	R	R					C							C		R			R		A						R			R					R		A								R
late Miocene	NN11	CN9b	24X-CC, 31-40	222.13	M	A						R										C		R					C	R	C			F		A						R								C		A								R
			25X-CC, 26-33	224.07	M	A						C										F		R					C	F	R			R		A						C								F		A								F
			26X-CC, 41-48	241.05	M	A		R				C							R	R	F	F		R					F	C	C			F		A						C								F		A					R			F
			27X-CC, 22-29	243.99	M	A	R	R				C	R									R		R					F	C	F					A						C								F		A					R			R
			28X-CC, 28-35	259.30	M	A	R	R		R		F	F						R		R	F						R	F	C	F			R		A						C								F		A					R			F
			29X-CC, 19-26	269.06	M	A	R	R				F	F						F		R	F		R					C	C	F			C		A						C								F		A					R			C
			30X-CC, 25-32	279.17	M	A		R	R	R		F	F						F		F	F		R				R	R	C	F					A						C								C		A					R			R
			31X-CC, 40-47	289.05	M	A		R	R	R		F	R						F		C	F							F	C	R			R		A						C								F		A					R			F
			32X-CC, 35-42	299.02	M	A		R				C	R						F		C	R		R						C	R			R		A						F								A		A					F			R
			33X-CC, 35-42	308.76	M	A		R		R									F		C	R								C	R					A						C								F		A					R			F
			34X-CC, 38-43	317.52	G	A		R		R		R							R		A	C				R			C	C	R			R		A						R			R							A								
			35X-CC, 33-40	327.36	G	A				R		R	R						R		A	C							C	C	R			R		C						R								R		A					R			
			36X-CC, 41-47	337.55	G	A				R		R	R								A	C				R			C	F	R					C						R								R		A								
			37X-CC, 32-37	347.60	M	A				R		R							R		A	C							F	C	R			R		C						R			R					R		A								
		CN9a	38X-CC, 33-39	357.80	M	A						R									A	F			R				F	C	R			R		C						R								R		A								
			39X-CC, 27-33	366.62	G	A						R							R		A	F			R				F	F	R			R		C						R								R		A								

Table T8 (continued).

Epoch	Zones		Core, section, interval (cm)	Depth (mcd)	Preservation	Abundance	*Amaurolithus amplificus*	*Amaurolithus delicatus*	*Amaurolithus ninae*	*Amaurolithus primus*	*Amaurolithus tricorniculatus*	*Calcidiscus leptoporus*	*Calcidiscus macintyrei*	*Catinaster coalitus*	*Ceratolithus acutus*	*Ceratolithus armatus*	*Ceratolithus cristatus*	*Ceratolithus rugosus*	*Coccolithus pelagicus*	*Discoaster asymmetricus*	*Discoaster berggrenii*	*Discoaster brouweri*	*Discoaster hamatus*	*Discoaster intercalaris*	*Discoaster loeblichii*	*Discoaster neohamatus*	*Discoaster neorectus*	*Discoaster pansus*	*Discoaster pentaradiatus*	*Discoaster quinqueramus*	*Discoaster surculus*	*Discoaster tamalis*	*Discoaster triradiatus*	*Discoaster variabilis*	*Emiliania huxleyi*	*Florisphaera profunda*	*Gephyrocapsa caribbeanica*	*Gephyrocapsa lumina*	*Gephyrocapsa margarelii*	*Gephyrocapsa oceanica*	*Gephyrocapsa* spp. (small)	*Helicosphaera carteri*	*Helicosphaera hyalina*	*Helicosphaera inversa*	*Helicosphaera sellii*	*Oolithotus antillarum*	*Pseudoemiliania lacunosa*	*Reticulofenestra asanoi*	*Reticulofenestra oamaruensis*	*Reticulofenestra pseudoumbilicus*	*Reticulofenestra umbilicus*	*Sphenolithus abies/neoabies*	*Sphenolithus belemnos*	*Sphenolithus ciperoensis*	*Sphenolithus heteromorphus*	*Thorosphaera flabellata*	*Triquetrorhabdulus rugosus*	*Umbellosphaera irregularis*	*Umbellosphaera tenuis*	*Umbilicosphaera sibogae*
late Miocene	NN11	CN 9a	40X-CC, 43-49	374.58	G	A						R							R		A	C				R			F	F	R			F		C						R										A								
			41X-CC, 49-55	385.47	G	A						R							R		C	F				R			F	F	R					C						R										A					R			
			42X-CC, 42-48	396.30	G	A						R							R		C	F							F	F						C						R										A								R
			43X-CC, 17-19	384.36	G	A						R							R		C	F			R				F	F				F		C						R										A								
			44X-CC, 39-46	413.59	M	A						R									C	F			F				F	F				F		C						R										A								
			184-1143C-																																																									
			43X-CC, 48-54	412.00	M	A						R	R								F	F			R	F			R	R				F		F						F								F		A								
	NN10–NN9	CN8–CN7	44X-CC, 46-52	422.64	M	A						R	R						R	R		C			C	F			F					C		C						F								F		C								
			45X-CC, 34-40	432.82	M	A						R							R			F			F	C			F	F				C		C						F								F		C								
			46X-CC, 48-54	440.33	M	A																F			F	F				F				C		C						F								F		C								
			47X-CC, 36-42	452.13	P	A													R			F			F	F			F					C		C						F								C		C								
			48X-CC, 33-39	460.55	P	A						R										F			F	C			F	R				C		C						F								C		C								
			49X-CC, 42-47	470.61	P	F							R	C								R	F		R	F			R	R				C		C						F								C	R	C								
			50X-CC, 27-33	480.03	P	A								C					R			R			F				R					C		C						F								C	R	C								
			51X-CC, 41-48	488.79	P	A							R	C								R			F	R								C		C						F								C		C								
			52X-CC, 44-49	499.79	P	A						R	R						R			R			F	R								C		C						F								C	R	C								
			53X-CC, 48-53	509.36	P	A							C						R			R			F									C		F						R								C	R	C								
			54X-CC, 43-48	512.88	P	A							C						R						F									C		C						F								C	R	C								

Notes: D = dominant, A = abundant, F = few/frequent, C = common, R =rare, P = present, G = good. See **“Biostratigraphy,”** p. 9, in the “Explanatory Notes” chapter.

Table T9. Planktonic foraminifer checklist for Site 1143.

Epoch	Zone	Core, section, interval (cm)	Depth (mcd)	Abundance	Preservation	*Dentoglobigerina altispira*	*Globigerinoides conglobatus*	*Globigerinoides extremus*	*Globigerinoides fistulosus*	*Globigerinoides ruber*	*Globigerinoides ruber* (pink)	*Globigerinoides sacculifer*	*Globorotalia cibaoensis*	*Globorotalia crassaformis*	*Globorotalia margaritae*	*Globorotalia mayeri*	*Globorotalia menardii*	*Globorotalia multicamerata*	*Globorotalia plesiotumida*	*Globorotalia tumida*	*Globorotalia tosaensis*	*Globorotalia truncatulinoides*	*Neogloboquadrina acostaensis*	*Pulleniatina* (dextral)	*Pulleniatina* (sinistral)	*Pulleniatina obliquiloculata*	*Sphaeroidinella dehiscens*	*Sphaeroidinellopsis kochi*	*Sphaeroidinellopsis seminulina*	*Globoturborotalia nepenthes*
		184-1143A-																												
Pleistocene	N22	1H-CC, 13-18	2.88	C	G					F		F		R								P								
		2H-CC, 16-21	13.20	C	G						A			R								R								
		3H-CC, 15-20	23.39	F	M						A			P												A				
		4H-CC, 15-20	34.02	C	G					A				P								P								
		5H-CC, 21-26	43.76	A	G					A												P				F	R			
		6H-CC, 29-34	53.71	A	G					A												P				F				
		7H-CC, 12-17	63.38	A	G																	P				F	F			
		8H-CC, 22-27	73.59	A	G												F					P				R				
		9H-CC, 25-30	83.28	A	G					A							R					P					P			
		10H-CC, 22-27	93.50	A	G				P													P								
late Pliocene	N21	11H-CC, 39-47	103.54	A	G													F									R			
		12H-CC, 21-27	113.00	A	G													F			P									
		13H-CC, 18-25	122.73	A	G													R			P									
		14H-CC, 20-24	132.66	A	G													R									R			
		15H-CC, 11-15	142.37	A	G	F		P										R			P									
	N20	16H-CC, 39-45	152.46	A	G	F		P										R						P					P	
		17H-7, 24-34	161.69	A	G	F		P							P			R											P	
early Pliocene	N19	18H-7, 43-59	171.91	A	G	R		P										R							P				P	
		19H-CC, 0-10	180.77	A	G	F	P								P					P					F				P	P
		20H-CC, 0-10	190.84	A	G	F	P								P										R			P	P	P
		21H-CC, 0-8	200.57	A	G	R	P	R							P					P					R			P	P	P
		22X-CC, 45-50	208.29	A	G		P								P			R		P					R			P		P
late Miocene	N18	23X-CC, 22-29	212.96	A	G		P													P					P			P		P
		24X-CC, 31-40	222.13	A	G	R	P													P								P		P
		25X-CC, 26-33	224.07	A	G	R	P						P							P								P	P	P
		26X-CC, 41-48	241.05	A	G		P													P								P		P
	N17b	27X-CC, 22-29	243.99	A	G		P	F																				P		
		28X-CC, 28-35	259.30	A	M		P	R											P											P
		29X-CC, 19-26	269.06	A	G		P	R							P				P				P					P		P
	N17a	30X-CC, 25-32	279.17	A	G			F											P				R							
		31X-CC, 40-47	289.05	F	M			R					P						P											
		32X-CC, 35-42	299.02	A	M			F					P						P				R							P
		33X-CC, 35-42	308.76	A	G			F					P										R					P		
		34X-CC, 38-43	317.52	A	G			R															R					P		
		35X-CC, 33-40	327.36	A	G	R		R											P				R							
		36X-CC, 41-47	337.55	A	G	F		R										P	P				R							P
		37X-CC, 32-37	347.60	A	G	A		P											P											
		38X-CC, 33-39	357.80	A	G	R		P											P									P		
		39X-CC, 27-33	366.62	A	G	R		P											P				P							
		40X-CC, 43-49	374.58	A	G			P											P				P					P		
		41X-CC, 49-55	385.47	A	G			P											P									P		
		42X-CC, 42-48	396.30	A	G			P											P											P
		43X-CC, 17-19	384.36	A	G			R											P				P					P		
		44X-CC, 39-46	413.59	A	G			F											P											
		184-1143C-																												
late Miocene	N16	44X-CC, 46-52	422.64	A	G	P																								R
		45X-CC, 34-40	432.82	A	G	P																								P
		46X-CC, 48-54	440.33	A	G	R																								R
	N16-N15	47X-CC, 36-42	452.13	A	G	P							P																	F
		48X-CC, 33-39	460.55	A	G	P																								F
		49X-CC, 42-47	470.61	T	P																									
	N14	50X-CC, 27-33	480.03	A	G	R		R								P		F												F
		51X-CC, 41-48	488.79	C	G	P		F								F														R
		52X-CC, 44-49	499.79	A	VG	P		F								P														R
		53X-CC, 48-53	509.36	A	G			A								F							F					R		
		54X-CC, 43-48	512.88	A	G			A								A			P											

Notes: D = dominant, A = abundant, F = few/frequent, C = common, R =rare, P = present, G = good, M = moderate. See **"Biostratigraphy,"** p. 9, in the "Explanatory Notes" chapter.

Table T10. Sedimentation and accumulation rates for selected intervals, based on age-depth model and rates presented in Figure F17, p. 56.

	Bottom of interval					
	Age (Ma)	Depth (mcd)	LSR total (m/m.y.)	LSR carbonate (m/m.y.)	MAR total (g/cm^2/k.y.)	MAR carbonate (g/cm^2/k.y.)
NN21/NN20	0.26	16.6	62	10.3	3.5	0.59
Brunhes/Matuyama	0.78	43.2	49	8.8	3.2	0.58
Pleistocene/Pliocene	1.77	85.9	44	7.8	3.6	0.65
Pliocene/Miocene	5.32	213.3	36	10.1	3.8	1.05
Bottom of hole	9.88	512.9	66	31.3	7.9	3.76

Note: LSR = linear sedimentation rate for total sediment and inorganic carbonate, MAR = mass accumulation rate for total sediment and inorganic carbonate.

Table T11. Corrected sediment thickness at Site 1143.

Depth interval (mcd)	Measured thickness (m)	Recognized turbidites (m)	Corrected thickness (m)
0-43.15	43.15	0.11	43.04
43.15-147.42	104.27	0.37	103.90
147.42-210.62	63.40	0.01	63.40
210.62-342.57	131.95	17.13	114.82
342.57-504.57	162.00	9.11	152.89

Table T12. Inorganic carbon, carbonate, total carbon, total organic carbon, Rock-Eval, total nitrogen, and total sulfur contents at Site 1143. (**See table note.** Continued on next three pages.)

	Depth					TOC			
Core, section, interval (cm)	(mbsf)	(mcd)	IC (wt%)	$CaCO_3$ (wt%)	TC (wt%)	TC – IC (wt%)	R-E (wt%)	TN (wt%)	TS (wt%)
184-1143A-									
1H-1, 67-68	0.67	0.69	3.40	28.30	3.93	0.53		0.17	0.21
1H-2, 67-68	2.17	2.19	0.99	8.25	1.75	0.76		0.17	0.15
2H-1, 67-68	3.57	3.99	1.51	12.54	1.95	0.45		0.14	0.24
2H-3, 67-68	6.57	6.99	2.82	23.51	3.18	0.35		0.11	0.21
2H-5, 67-68	9.57	9.99	0.86	7.12	1.44	0.59	0.34	0.14	0.27
3H-1, 67-68	13.07	14.17	2.39	19.89	2.76	0.37		0.13	0.11
3H-3, 67-68	16.07	17.17	1.53	12.72	1.89	0.36		0.12	0.21
3H-5, 67-68	19.07	20.17	3.32	27.64	3.74	0.42		0.16	0.24
4H-1, 67-68	22.57	24.71	2.87	23.91	3.10	0.23		0.10	
4H-3, 67-68	25.57	27.71	1.44	11.98	1.82	0.38		0.13	
4H-5, 67-68	28.57	30.71	1.51	12.62	1.85	0.34		0.15	0.42
5H-1, 67-68	32.07	34.61	2.22	18.51	2.57	0.35		0.14	0.24
5H-3, 67-68	35.07	37.61	1.70	14.20	2.13	0.43		0.14	0.09
5H-5, 67-68	38.07	40.61	2.81	23.39	3.25	0.44		0.14	0.06
6H-1, 67-68	41.57	44.33	2.09	17.44	2.55	0.45		0.13	0.14
6H-3, 67-68	44.57	47.33	2.25	18.74	2.72	0.47	0.20	0.13	0.11
6H-5, 67-68	47.57	50.33	1.39	11.62	1.71	0.31		0.13	0.10
7H-1, 67-68	51.07	54.49	3.55	29.55	3.82	0.27		0.11	0.30
7H-3, 67-68	54.07	57.49	1.52	12.66	1.76	0.24		0.11	0.14
7H-5, 67-68	57.07	60.49	0.80	6.70	1.01	0.21		0.11	0.06
8H-1, 67-68	60.57	64.27	2.13	17.70	2.41	0.28		0.13	
8H-3, 67-68	63.57	67.27	1.37	11.38	1.90	0.54	0.34	0.12	0.19
8H-5, 67-68	66.62	70.32	3.27	27.28	3.49	0.22		0.13	0.19
9H-1, 67-68	70.07	74.17	1.36	11.35	1.52	0.16		0.11	0.24
9H-3, 67-68	73.07	77.17	2.74	22.81	2.94	0.20		0.11	
9H-5, 67-68	76.07	80.17	1.88	15.64	2.18	0.31		0.12	0.57
10H-1, 67-69	79.57	84.21	2.44	20.30	2.66	0.22		0.12	0.04
10H-3, 67-68	82.57	87.21	2.18	18.17	2.39	0.21		0.11	0.43
10H-5, 67-68	85.57	90.21	3.12	26.02	3.33	0.21		0.11	0.28
11H-1, 67-68	89.07	94.31	2.24	18.69	2.50	0.25		0.10	0.34
11H-3, 67-68	92.07	97.31	3.01	25.11	3.31	0.30		0.13	0.29
11H-5, 67-68	95.07	100.31	1.26	10.48	1.47	0.22		0.11	0.51
12H-1, 67-68	98.57	103.75	2.73	22.78	2.95	0.21		0.11	
12H-3, 67-68	101.57	106.75	2.26	18.86	2.49	0.22		0.11	
12H-5, 67-68	104.57	109.75	2.42	20.14	2.67	0.26		0.11	
13H-1, 67-68	108.07	113.71	3.47	28.89	3.77	0.30		0.14	
13H-3, 67-68	111.07	116.71	1.17	9.75	1.39	0.22		0.13	
13H-5, 67-68	114.07	119.71	3.01	25.06	3.19	0.18		0.12	
14H-1, 67-68	117.57	123.59	2.84	23.70	3.09	0.25		0.13	0.24
14H-3, 67-68	120.57	126.59	2.42	20.15	2.56	0.14		0.11	
14H-5, 67-68	123.57	129.59	1.30	10.82	1.54	0.24		0.14	0.29
15H-1, 67-68	127.07	133.95	2.48	20.68	2.67	0.19		0.11	
15H-3, 67-68	130.07	136.95	2.54	21.13	2.70	0.16		0.11	
15H-5, 67-68	133.07	139.95	2.62	21.81	2.84	0.22		0.10	
16H-1, 67-68	136.57	143.13	2.42	20.12	2.70	0.28		0.12	0.13
16H-3, 67-68	139.57	146.13	2.56	21.36	2.76	0.20		0.11	0.80
16H-5, 67-68	142.57	149.13	2.60	21.70	2.84	0.24		0.14	0.29
17H-1, 67-68	146.07	153.05	3.84	32.01	4.13	0.29		0.11	0.08
17H-3, 67-68	149.07	156.05	3.63	30.26	3.82	0.19		0.12	
17H-5, 67-68	152.07	159.05	2.71	22.57	2.87	0.16		0.12	
18H-1, 67-68	155.57	163.09	4.19	34.89	4.34	0.15		0.11	
18H-3, 67-68	158.47	165.99	3.00	25.02	3.18	0.18		0.11	0.13
18H-5, 67-68	161.48	169.00	3.55	29.56	3.77	0.22		0.11	0.13
19H-1, 67-68	165.07	172.24	4.80	40.02	5.13	0.33		0.08	
19H-3, 67-68	168.07	175.24	4.15	34.60	4.37	0.22		0.09	
19H-5, 67-68	171.07	178.24	3.53	29.41	3.79	0.26		0.10	
20H-1, 67-68	174.57	182.42	3.83	31.88	4.11	0.28		0.12	0.11
20H-3, 67-68	177.57	185.42	2.70	22.45	2.97	0.27		0.12	0.20
20H-5, 67-68	180.57	188.42	4.26	35.51	4.48	0.22		0.11	0.21
21H-1, 67-68	184.07	194.19	4.25	35.42	4.60	0.35		0.10	
21H-3, 67-68	187.07	197.19	5.31	44.25	5.43	0.12		0.12	
21H-5, 67-68	190.07	200.19	5.59	46.57	5.76	0.17		0.10	
22X-1, 67-68	191.07	201.77	4.90	40.82	5.07	0.17		0.08	0.06
22X-3, 67-68	194.07	204.77	5.05	42.09	5.18	0.13		0.11	

Table T12 (continued).

	Depth					TOC			
Core, section, interval (cm)	(mbsf)	(mcd)	IC (wt%)	$CaCO_3$ (wt%)	TC (wt%)	TC – IC (wt%)	R-E (wt%)	TN (wt%)	TS (wt%)
22X-5, 67-68	197.07	207.77	4.73	39.39	5.03	0.30	0.09	0.07	
23X-1, 67-68	198.67	209.17	5.09	42.41	5.16	0.07		0.12	
23X-3, 67-68	201.67	212.17	4.62	38.45	4.55			0.07	0.04
24X-1, 67-68	202.67	213.11	5.19	43.26	5.28	0.09		0.13	
24X-3, 67-68	205.67	216.11	3.89	32.37	4.02	0.13		0.08	
24X-5, 67-68	208.67	219.11	5.72	47.67	5.87	0.15		0.10	
25X-1, 79-80	212.39	221.11	5.48	45.63	5.62	0.14		0.11	
26X-1, 67-68	221.87	232.03	4.68	38.98	4.81	0.13		0.07	0.46
26X-2, 67-68	223.37	233.53	4.93	41.06	5.03	0.10		0.10	
26X-4, 67-68	226.37	236.53	7.30	60.79	7.44	0.14		0.07	0.10
27X-2, 67-68	232.97	242.75	5.49	45.74	5.55	0.06		0.10	
28X-1, 67-68	241.07	251.39	3.81	31.76	4.10	0.29		0.12	
28X-3, 67-68	244.07	254.39	5.75	47.92	5.67			0.07	0.12
28X-5, 67-68	247.07	257.39	5.92	49.29	6.14	0.22		0.11	
29X-1, 92-93	250.92	260.34	6.16	51.35	6.40	0.24		0.10	
29X-3, 57-58	253.57	262.99	5.00	41.65	5.17	0.17		0.08	
29X-5, 67-68	256.67	266.09	4.31	35.88					
30X-1, 67-68	260.27	270.21	4.51	37.55	4.81	0.30		0.13	
30X-3, 67-68	263.27	273.21	4.61	38.43	5.01	0.40		0.09	
30X-4, 15-16	264.25	274.19	3.32	27.65	4.20	0.88	0.67	0.11	0.30
30X-4, 95-96	266.27	276.21	5.09	42.42	5.26	0.17		0.07	
31X-1, 67-68	269.87	279.99	5.01	41.75	5.37	0.36		0.13	
31X-3, 67-68	272.87	282.99	5.10	42.45	5.38	0.28		0.12	
31X-5, 67-68	275.87	285.99	5.32	44.31	5.53	0.21		0.07	
32X-1, 67-68	279.57	289.91	5.46	45.49	5.63	0.17		0.07	0.15
32X-3, 67-68	282.57	292.91	5.23	43.55	5.40	0.17		0.08	0.19
32X-5, 67-68	285.57	295.91	5.46	45.47	5.71	0.25		0.11	0.15
33X-1, 69-70	289.19	299.85	5.30	44.12	5.53	0.23		0.09	0.09
33X-3, 68-69	292.18	302.84	4.12	34.28	4.92	0.80	0.77	0.13	0.55
33X-5, 67-68	295.17	305.83	6.81	56.71	6.90	0.09		0.10	0.03
34X-1, 67-68	298.77	309.43	6.65	55.42	6.81	0.16		0.07	0.05
34X-3, 67-68	301.77	312.43	6.74	56.17	6.83	0.09		0.06	0.06
34X-5, 67-68	304.77	315.43	6.95	57.92	7.18	0.23		0.07	0.06
35X-1, 67-68	308.37	318.41	5.00	41.68	5.19	0.19		0.07	
35X-3, 67-68	311.37	321.41	6.54	54.45	6.78	0.24		0.06	0.05
35X-5, 67-68	314.37	324.41	6.83	56.89	7.06	0.23		0.06	0.08
36X-1, 67-68	317.97	328.63	6.57	54.75	6.68	0.11		0.06	
36X-3, 67-68	320.97	331.63	6.32	52.65	6.65	0.33		0.06	
36X-5, 67-68	323.97	334.63	7.20	59.96					
37X-1, 67-68	327.57	338.49	6.43	53.60	6.65	0.22		0.07	
37X-3, 67-68	330.57	341.49	5.98	49.80					
37X-5, 67-68	333.57	344.49	5.84	48.62					
38X-1, 67-68	337.07	348.65	5.36	44.63					
38X-3, 67-68	340.07	351.65	5.35	44.57	5.64	0.29		0.08	
38X-5, 67-68	343.07	354.65	6.59	54.86					
39X-1, 68-69	346.78	358.36	6.06	50.47					
39X-3, 62-63	349.72	361.30	6.45	53.68					
39X-5, 66-67	352.76	364.34	6.37	53.10	6.59	0.22		0.06	
40X-1, 67-68	356.37	367.69	5.14	42.80					
40X-3, 67-68	359.37	370.69	5.91	49.19					
40X-5, 67-68	362.37	373.69	4.72	39.31	4.92	0.20		0.08	
41X-1, 66-67	365.56	377.14	6.43	53.56					
41X-3, 67-68	368.57	380.15	6.22	51.82					
41X-5, 67-68	371.57	383.15	6.22	51.82	6.53	0.31		0.09	
42X-1, 67-68	375.17	389.21	5.34	44.45					
42X-3, 67-68	378.17	392.21	6.08	50.67					
42X-5, 67-68	381.17	395.21	5.96	49.61	6.20	0.24		0.08	
44X-1, 68-69	394.58	407.64	5.81	48.42					
44X-3, 67-68	397.57	410.63	5.77	48.04	6.12	0.35	0.09	0.10	
44X-5, 65-66	400.05	413.11	10.18	84.76					
184-1143B-									
5H-1, 65-66	34.55	38.79	3.04	25.29					
5H-3, 65-66	37.55	41.79	0.36	2.98					
5H-5, 65-66	40.55	44.79	1.23	10.22					
6H-1, 65-66	44.05	48.65	1.94	16.13					
6H-3, 65-66	47.05	51.65	1.66	13.85					
6H-5, 65-66	50.05	54.65	3.52	29.33					
7H-1, 67-68	53.57	59.13	2.28	19.00					
7H-3, 67-68	56.57	62.13	1.67	13.89					
7H-5, 67-68	59.57	65.13	2.54	21.12					

Table T12 (continued).

	Depth					TOC			
Core, section, interval (cm)	(mbsf)	(mcd)	IC (wt%)	$CaCO_3$ (wt%)	TC (wt%)	TC – IC (wt%)	R-E (wt%)	TN (wt%)	TS (wt%)
8H-1, 67-68	63.07	68.89	1.87	15.54					
8H-3, 67-68	66.07	71.89	3.04	25.31					
8H-5, 67-68	69.07	74.89	1.89	15.78					
9H-1, 67-68	72.57	79.15	2.19	18.21					
9H-3, 67-68	75.57	82.15	1.54	12.80					
9H-5, 67-68	78.57	85.15	2.55	21.28					
10H-1, 67-68	82.07	88.95	2.67	22.24					
10H-3, 67-68	85.07	91.95	2.01	16.73					
10H-5, 67-68	88.07	94.95	1.80	14.97					
11H-1, 67-68	91.57	98.67	1.68	14.03					
11H-3, 67-68	94.57	101.67	1.08	8.99					
11H-5, 67-68	97.57	104.67	2.78	23.18					
12H-1, 67-68	101.07	108.53	1.80	14.98					
12H-3, 67-68	104.07	111.53	2.73	22.77					
12H-5, 67-68	107.07	114.53	2.68	22.29					
13H-1, 67-68	110.57	118.37	2.66	22.15					
13H-3, 67-68	113.57	121.37	1.81	15.09					
13H-5, 67-68	116.57	124.37	2.12	17.63					
14H-1, 67-68	120.07	128.27	1.99	16.55					
14H-3, 67-68	123.07	131.27	2.30	19.20					
14H-5, 67-68	126.07	134.27	2.79	23.21					
15H-1, 67-68	129.57	137.89	2.51	20.89					
15H-3, 67-68	132.57	140.89	2.56	21.32					
15H-5, 67-68	135.57	143.89	2.71	22.54					
16H-1, 67-68	139.07	147.61	2.13	17.78					
16H-3, 67-68	141.97	150.51	2.21	18.38					
16H-5, 67-68	144.97	153.51	4.02	33.45					
17H-1, 67-68	148.57	157.39	3.91	32.57					
17H-3, 67-68	151.57	160.39	4.58	38.13					
17H-5, 67-68	154.57	163.39	3.64	30.29					
18H-2, 67-68	159.17	167.46	3.42	28.47					
18H-3, 67-68	160.67	168.96	4.91	40.92					
18H-5, 67-68	163.67	171.96	4.34	36.14					
19H-1, 67-68	167.57	176.64	3.27	27.22					
19H-3, 67-68	170.57	179.64	4.06	33.82					
19H-5, 67-68	173.57	182.64	4.18	34.78					
20X-1, 67-68	176.07	184.94	3.86	32.19					
20X-3, 67-68	179.07	187.94	4.69	39.09					
20X-5, 55-56	181.95	190.82	4.81	40.09					
21X-1, 37-39	181.47	191.56	4.90	40.84					
21X-3, 67-68	183.88	193.97	4.48	37.34					
21X-5, 67-68	186.88	196.97	5.44	45.30					
22X-1, 67-68	191.37	203.03	5.10	42.51					
22X-3, 67-68	194.37	206.03	4.92	40.94					
23X-1, 67-68	200.97	211.51	5.12	42.63					
23X-3, 67-68	203.97	214.51	4.92	40.97					
23X-5, 67-68	206.97	217.51	4.65	38.73					
24X-1, 63-64	210.53	221.29	4.97	41.42					
24X-3, 67-68	213.57	224.33	5.32	44.30					
25X-1, 66-67	220.16	231.36	4.74	39.45					
25X-3, 66-67	223.16	234.36	5.03	41.86					
25X-5, 66-67	226.16	237.36	4.42	36.83					
26X-1, 84-85	230.04	241.52	4.99	41.54					
26X-3, 74-75	232.94	244.42	5.75	47.92					
26X-5, 33-34	235.53	247.01	5.53	46.10					
27X-1, 67-68	239.57	251.27	5.20	43.32					
27X-3, 66-68	242.56	254.26	6.21	51.69					
27X-5, 57-58	245.47	257.17	6.37	53.06					
28X-1, 88-89	249.48	260.36	6.59	54.91					
28X-3, 98-99	252.58	263.46	5.28	43.99					
28X-5, 77-78	255.37	266.25	4.39	36.58					
184-1143C-									
6H-2, 56-57	46.46	51.92	1.11	9.23					
6H-7, 34-35	53.74	59.2	1.50	12.53					
42X-1, 67-68	382.37	394.77	5.70	47.51					
42X-3, 67-68	385.37	397.77	5.07	42.26	5.31	0.23		0.08	0.62
42X-5, 67-68	388.37	400.77	6.28	52.30					
43X-1, 67-68	391.97	404.37	5.98	49.79					
43X-3, 67-68	394.97	407.37	6.74	56.16	6.87	0.13		0.07	
43X-5, 67-68	397.97	410.37	5.95	49.54					

Table T12 (continued).

Core, section, interval (cm)	Depth		IC (wt%)	$CaCO_3$ (wt%)	TC (wt%)	TOC		TN (wt%)	TS (wt%)
	(mbsf)	(mcd)				TC – IC (wt%)	R-E (wt%)		
44X-1, 67-68	401.67	414.07	5.95	49.55					
44X-3, 69-71	404.69	417.09	5.96	49.67	6.11	0.15		0.07	
44X-5, 67-68	407.67	420.07	6.00	50.00					
45X-1, 67-68	411.37	423.77	4.60	38.34					
45X-3, 66-67	414.36	426.76	4.99	41.56	5.17	0.18		0.07	0.09
45X-5, 67-68	417.37	429.77	5.67	47.20					
46X-1, 63-64	420.93	433.33	9.89	82.37					
46X-3, 84-85	424.14	436.54	5.26	43.82	5.46	0.20		0.08	
46X-5, 67-68	426.97	439.37	5.46	45.46					
47X-1, 65-66	430.55	442.95	5.43	45.24					
47X-3, 64-65	433.54	445.94	6.03	50.24	6.26	0.23		0.07	
47X-5, 63-64	436.53	448.93	5.24	43.64					
48X-1, 67-68	440.17	452.57	4.78	39.86					
48X-3, 67-68	443.17	455.57	5.66	47.11	5.86	0.21		0.06	
48X-5, 67-68	446.17	458.57	5.55	46.26					
49X-1, 67-68	449.87	462.27	4.77	39.75					
49X-3, 67-68	452.87	465.27	5.55	46.25	5.67	0.12		0.07	
49X-5, 67-68	455.87	468.27	6.06	50.46					
50X-1, 67-68	459.57	471.97	5.20	43.35					
50X-3, 68-69	462.58	474.98	5.19	43.27					
50X-5, 67-68	465.57	477.97	5.73	47.70					
51X-1, 67-68	469.17	481.57	5.49	45.73					
51X-3, 67-68	472.17	484.57	4.94	41.17	5.15	0.21		0.08	
51X-5, 67-68	475.17	487.57	6.99	58.21					
52X-1, 67-68	478.87	491.27	6.48	54.00					
52X-3, 67-68	481.87	494.27	5.90	49.14	6.04	0.14		0.06	
52X-5, 65-66	484.85	497.25	7.53	62.72					
53X-1, 65-66	488.55	500.95	4.87	40.58					
53X-3, 66-67	491.56	503.96	4.50	37.47	4.68	0.18		0.08	
53X-5, 67-68	494.57	506.97	5.39	44.94					
54X-1, 67-68	498.27	510.67	5.68	47.31	5.86	0.18		0.06	

Note: IC = inorganic carbon, $CaCO_3$ = carbonate, TC = total carbon, TOC = total organic carbon, R-E = Rock-Eval, TN = total nitrogen, TS = total sulfur.

Table T13. Composition of interstitial waters from Holes 1143A and 1143C.

Core, section, interval (cm)	Depth																	
	(mbsf)	(mcd)	pH	Alkalinity (mM)	Salinity	Cl^- (mM)	Na^+ (mM)	K^+ (mM)	Mg^{2+} (mM)	Mg^{2+}* (mM)	Ca^{2+} (mM)	Ca^{2+}* (mM)	SO_4^{2-} (mM)	HPO_4^{2-} (µM)	NH_4+ (mM)	H_4SiO_4 (µM)	Li^+ (µM)	Sr^{2+} (µM)
184-1143A-																		
1H-1, 145-150	1.48	1.50	7.78	4.26	35.0	549	472	12.4	51.5	50.5	10.3	10.5	27.6	15.6	0.2	476	29	93
2H-3, 145-150	7.38	7.80	7.74	5.35	35.0	555	476	11.9	51.2		9.9		25.5	33.7	0.4	651	27	100
3H-3, 145-150	16.88	17.98	7.74	6.82	34.0	558	484	12.2	49.3		8.8		24.0	16.6	0.5	693	33	107
4H-3, 145-150	26.38	28.52	7.83	7.79	34.0	558	484	12.2	48.5	48.7	8.5	8.9	22.9	12.0	0.6	689	38	118
5H-3, 145-150	35.88	38.42	7.86	8.05	35.0	561	482	11.4	47.3		8.0		17.9	6.9	0.6	579	46	128
6H-3, 145-150	45.38	48.14	7.84	8.00	34.0	559	487	11.1	46.1		7.2		19.2	3.6	0.7	501	52	139
9H-3, 145-150	73.88	77.98	7.86	7.93	33.5	559	486	9.9	44.1	45.2	6.0	6.3	15.1	1.6	0.9	355	63	186
12H-3, 145-150	102.38	107.56	7.83	7.29	34.0	561	487	9.5	41.6		5.5		12.3	1.0	1.3	220	88	261
15H-3, 140-150	130.85	137.73	7.81	7.36	33.0	561	486	10.1	39.9	40.4	5.5	5.4	10.2	1.2	1.2	251	172	379
18H-3, 140-150	159.25	166.77	7.23	7.98	33.0	561	487	10.6	37.0		6.6		9.2	0.8	1.3	279	347	506
21H-3, 140-150	187.85	197.97	7.81	10.07	32.5	559	483	10.4	35.4		8.4		7.8	1.6	1.3	433	920	653
24X-3, 140-150	206.45	216.89	7.83	11.02	33.0	559	483	9.8	34.6		9.5		7.3	1.2	1.4	652	1200	744
27X-1, 140-150	232.25	242.03	7.82	12.28	33.0	560	486	11.3	33.0	33.4	11.1	12.4	9.2	1.6	1.7	983	1515	874
30X-3, 140-150	264.05	273.99	6.91	11.21	33.0	559	484	12.1	31.1		12.2		9.0	1.5	1.8	1057	1900	1023
33X-3, 140-150	292.95	303.61	7.81	13.41	33.0	561	489	12.3	29.0		13.4		8.8	2.6	1.8	1312	2260	1101
36X-3, 140-150	321.75	332.41	7.86	11.51	33.0	561	490	13.3	27.3		13.6		9.8	1.8	1.8	1148	2685	1185
39X-3, 140-150	350.55	362.13	7.84	13.09	33.0	560	485	12.9	26.1	25.6	16.4	18.9	8.5	2.1	1.8	1419	3010	1269
42X-3, 140-150	378.95	392.99	6.62	14.23	33.5	559	486	12.2	24.5		18.5		9.2	2.1	1.7	1495	3420	1332
44X-3, 140-150	398.35	411.41	6.59	13.89	34.0	561	485	11.7	23.7		19.6		8.5	2.1	1.8	1467	3940	1367
184-1143C-																		
44X-3, 143-150	405.47	417.87	7.81	14.26	34.0	563	486	12.9	23.6		17.9		6.4	1.5	1.9	1239	3960	1346
47X-3, 140-150	434.35	446.75	7.77	13.96	33.5	558	481	11.6	22.6		19.4		6.7	1.2	1.8	1504	4200	1522
50X-3, 140-150	463.35	475.75	6.77	13.41	33.5	560	483	11.0	21.6		19.8		6.5	1.7	1.8	1482	4300	1594
53X-5, 135-150	495.33	507.73	7.77	8.87	34.0	559	481	10.4	21.2		18.8		6.3	1.9	1.7	1049	4300	1582

Note: * = data from titrations.

Table T14. Thermal conductivity measurements at Site 1143. (**See table note.** Continued on next page.)

Leg	Site	Hole	Core	Type	Section	Interval (cm) Top	Interval (cm) Bottom	Depth (mbsf)	Depth (mcd)	Thermal conductivity (W/[m·K])
184	1143	A	1	H	2	74	74	2.24	2.26	0.811
184	1143	A	2	H	2	76	76	5.16	5.58	0.859
184	1143	A	2	H	5	75	75	9.65	10.07	0.865
184	1143	A	3	H	2	75	75	14.65	15.75	0.863
184	1143	A	3	H	5	75	75	19.15	20.25	0.88
184	1143	A	4	H	2	75	75	24.15	26.29	0.872
184	1143	A	4	H	5	75	75	28.65	30.79	0.919
184	1143	A	5	H	2	75	75	33.65	36.19	0.911
184	1143	A	5	H	5	75	75	38.15	40.69	0.949
184	1143	A	6	H	2	75	75	43.15	45.91	0.931
184	1143	A	6	H	5	75	75	47.65	50.41	0.957
184	1143	A	7	H	2	75	75	52.65	56.07	0.914
184	1143	A	7	H	5	75	75	57.15	60.57	0.997
184	1143	A	8	H	2	75	75	62.20	65.90	0.983
184	1143	A	8	H	5	75	75	66.70	70.40	1.002
184	1143	A	9	H	2	75	75	71.65	75.75	0.959
184	1143	A	9	H	5	75	75	76.15	80.25	1.054
184	1143	A	10	H	2	75	75	81.15	85.79	1.046
184	1143	A	10	H	5	75	75	85.65	90.29	1.065
184	1143	A	11	H	2	75	75	90.65	95.89	1.017
184	1143	A	11	H	5	75	75	95.15	100.39	1.059
184	1143	A	12	H	2	75	75	100.15	105.33	1.068
184	1143	A	12	H	5	73	73	104.63	109.81	1.029
184	1143	A	13	H	2	75	75	109.65	115.29	1.034
184	1143	A	13	H	5	75	75	114.15	119.79	1.055
184	1143	A	14	H	2	75	75	119.15	125.17	1.065
184	1143	A	14	H	5	80	80	123.70	129.72	1.033
184	1143	A	15	H	2	75	75	128.65	135.53	1.072
184	1143	A	15	H	5	75	75	133.15	140.03	1.025
184	1143	A	16	H	2	75	75	138.15	144.71	0.908
184	1143	A	16	H	5	75	75	142.65	149.21	1.135
184	1143	A	17	H	2	75	75	147.65	154.63	0.946
184	1143	A	17	H	5	75	75	152.15	159.13	1.141
184	1143	A	18	H	2	75	75	157.15	164.67	1.027
184	1143	A	18	H	5	76	76	161.57	169.09	1.142
184	1143	A	19	H	2	75	75	166.65	173.82	1.115
184	1143	A	19	H	5	75	75	171.15	178.32	1.163
184	1143	A	20	H	2	75	75	176.15	184.00	1.041
184	1143	A	20	H	5	75	75	180.65	188.50	1.170
184	1143	A	21	H	2	75	75	185.65	195.77	1.115
184	1143	A	21	H	5	51	51	189.91	200.03	1.154
184	1143	A	22	X	2	75	75	192.65	203.35	0.829
184	1143	A	22	X	5	36	36	196.76	207.46	0.750
184	1143	A	23	X	2	75	75	200.25	210.75	1.010
184	1143	A	24	X	2	75	75	204.25	214.69	1.012
184	1143	A	24	X	5	75	75	208.75	219.19	0.982
184	1143	A	26	X	2	75	75	223.45	233.61	0.973
184	1143	A	26	X	5	75	75	227.95	238.11	0.813
184	1143	A	27	X	2	50	50	232.8	242.58	1.013
184	1143	A	28	X	2	75	75	242.65	252.97	0.916
184	1143	A	28	X	5	75	75	247.15	257.47	1.005
184	1143	A	29	X	2	75	75	252.25	261.67	0.947
184	1143	A	29	X	5	85	85	256.85	266.27	0.944
184	1143	A	30	X	2	75	75	261.85	271.79	1.025
184	1143	A	30	X	5	75	75	266.35	276.29	0.937
184	1143	A	31	X	2	75	75	271.45	281.57	1.084
184	1143	A	31	X	5	75	75	275.95	286.07	1.136
184	1143	A	32	X	2	75	75	281.15	291.49	1.159
184	1143	A	32	X	5	75	75	285.65	295.99	0.966
184	1143	A	33	X	2	75	75	290.75	301.41	1.048
184	1143	A	33	X	5	75	75	295.25	305.91	1.089
184	1143	A	34	X	2	75	75	300.35	311.01	1.119
184	1143	A	34	X	5	75	75	304.85	315.51	1.064
184	1143	A	35	X	2	75	75	309.95	319.99	1.018
184	1143	A	35	X	5	75	75	314.45	324.49	1.104
184	1143	A	36	X	2	75	75	319.55	330.21	0.998
184	1143	A	36	X	5	75	75	324.05	334.71	0.963

Table T14 (continued).

						Interval (cm)		Depth		Thermal
Leg	Site	Hole	Core	Type	Section	Top	Bottom	(mbsf)	(mcd)	conductivity (W/[m·K])
184	1143	B	5	H	5	75	75	40.65	44.89	0.963
184	1143	B	5	H	6	75	75	42.15	46.39	0.934
184	1143	B	5	H	7	25	25	43.15	47.39	0.860
184	1143	B	6	H	1	75	75	44.15	48.75	0.811
184	1143	B	6	H	2	75	75	45.65	50.25	0.868
184	1143	B	6	H	3	75	75	47.15	51.75	0.933
184	1143	B	6	H	4	75	75	48.65	53.25	0.901
184	1143	B	11	H	2	76	76	93.16	100.26	0.908
184	1143	B	11	H	3	70	70	94.60	101.70	0.880
184	1143	B	11	H	4	75	75	96.15	103.25	0.853
184	1143	B	11	H	5	86	86	97.76	104.86	1.051
184	1143	B	11	H	6	82	82	99.22	106.32	1.059
184	1143	B	11	H	7	24	24	100.14	107.24	0.974
184	1143	B	12	H	1	75	75	101.15	108.61	0.962
184	1143	B	12	H	2	75	75	102.65	110.11	1.046
184	1143	B	16	H	2	75	75	140.55	149.09	0.946
184	1143	B	16	H	3	75	75	142.05	150.59	0.887
184	1143	B	16	H	4	75	75	143.55	152.09	0.984
184	1143	B	16	H	5	75	75	145.05	153.59	1.084
184	1143	B	16	H	6	75	75	146.55	155.09	1.105
184	1143	B	16	H	7	27	27	147.57	156.11	0.931
184	1143	B	17	H	1	75	75	148.65	157.47	0.998
184	1143	B	17	H	2	75	75	150.15	158.97	1.072

Note: This table is also available in **ASCII format.**

Table T15. Summary of logging operations at Site 1143.

Date (March 1999)	Time (local)	
6	0015	Hole preparation complete, rig up wireline.
6	0045	Rig into hole with HNGS-APS-HLDS-DIT-TAP.
6	0400	Uplog at 275 m/hr from 400 to 305 mbsf. Rig into hole to total depth.
6	0420	Uplog at 275 m/hr from 400 mbsf to seafloor. Pull out of hole.
6	0800	Pipe trip.
6	1030	Rig up NGT-FMS-DSI.
6	1115	DSI failure, troubleshoot, DSI replaced by LSS.
6	1300	Rig into hole with NGT-FMS-LSS.
		Bridge near end of pipe (EOP) prevents going down. Pull out of hole.
6	1700	Reposition EOP at 134 mbsf.
6	1745	Rig into hole with NGT-FMS-LSS.
6	2020	Uplog at 275 m/hr from 378 mbsf to EOP.
6	2315	End of logging operations.

Note: HNGS = hostile environment natural gamma-ray sonde, APS = accelerator porosity sonde, HLDS = hostile environment lithodensity sonde, DIT = dual-induction tool, TAP = Lamont-Doherty Earth Observatory (LDEO) temperature/acceleration/pressure tool, NGT = natural gamma-ray tool, FMS = Formation MicroScanner, DSI = dipole sonic imager, LSS = long-spaced sonic logging tool.